The Pennsylvania State University

The Graduate School

Department of Materials Science and Engineering

HIGH-PERFORMANCE POLYMER/LAYERED SILICATE

NANOCOMPOSITES

A Thesis in

Materials Science and Engineering

by

Matthew J. Heidecker

Submitted in Partial Fulfillment
of the Requirements
for the Degree of

Doctor of Philosophy

August 2007

The thesis of Matthew J. Heidecker was reviewed and approved* by the following:

Evangelos Manias
Associate Professor of Materials Science and Engineering
Thesis Advisor
Chair of Committee

Kwadwo Osseo-Asare
Distinguished Professor of Metallurgy and Energy and Geo-environmental
Engineering

Charles Bakis
Professor of Engineering Science and Mechanics

Ronald Hedden
Asst. Professor of Materials Science and Engineering

James Runt
Professor of Polymer Science
Chair, Intercollege Graduate Degree Program in Materials Science and
Engineering

*Signatures are on file in the Graduate School

ABSTRACT

High-performance layered-silicate nanocomposites of Polycarbonate (PC), poly(ethylene terephthalate) (PET), and their blends were produced via conventional melt-blending techniques. The focus of this thesis was on the fundamentals of dispersion, control of thermal stability, maintenance of melt-blending processing conditions, and on optimization of the composites' mechanical properties via the design of controlled and thermodynamically favorable nano-filler dispersions within the polymer matrices.

PET and PC require high temperatures for melt-processing, rendering impractical the use of conventional/commercial organically-modified layered-silicates, since the thermal degradation temperatures of their ammonium surfactants lies below the typical processing temperatures. Thus, different surfactant chemistries must be employed in order to develop melt-processable nanocomposites, also accounting for polymer matrix degradation due to water (PET) or amine compounds (PC). Novel high thermal-stability surfactants were developed and employed in montmorillonite nanocomposites of PET, PC, and PC/PET blends, and were compared to the respective nanocomposites based on conventional quaternary-ammonium modified montmorillonites. Favorable dispersion was achieved in all cases, however, the overall material behavior –*i.e.*, the combination of crystallization, mechanical properties, and thermal degradation– was better for the nanocomposites based on the thermally-stable surfactant fillers.

Studies were also done to trace, and ultimately limit, the matrix degradation of Polycarbonate/montmorillonite nanocomposites, through varying the montmorillonite surfactant chemistry, processing conditions, and processing additives. Molecular weight

degradation was, maybe surprisingly, better controlled in the conventional quaternary ammonium based nanocomposites –even though the thermal stability of the organically modified montmorillonites was in most cases the lowest. Dependence of the resultant nanocomposites' mechanical properties on the preferential alignment of the montmorillonite nano-platelet was also evaluated. Highly aligned filler platelets did not result in an additional enhancement in mechanical properties.

PC/PET blends and their respective PC/PET/montmorillonite nanocomposites were synthesized and compared. The dispersion of the organically modified nano-fillers in the PC/PET blends was controlled via thermodynamic considerations, realized through proper surfactant choice: Nanocomposites in which the layered silicate was preferentially sequestered in the PET phase were designed and synthesized. This preferential dispersion of the nano-filler in the PET phase of the PC/PET blend was insensitive to processing conditions, including approaches employing a master-batch (filler concentrate); regardless of the master-batch matrix, both PC and PET were employed, thermodynamics drove the layered silicate to preferentially migrate to the PET phase of the PC/PET blend.

In a second approach, the development of a nanocomposite with controlled PC/PET compatibilization near the montmorillonite platelets, in absence of appreciable transesterification reactions, led to the formation of very high performance nanocomposites. These latter systems, point to an exciting new avenue of future considerations for nanocomposite blends with selective nano-filler dispersions, where performance can be tailored via the controlled preferential dispersion of nano-fillers in one phase, or by filler-induced polymer compatibilization.

TABLE OF CONTENTS

LIST OF FIGURES

LIST OF TABLES

ACKNOWLEDGEMENTS

Chapter 1

Aim and Scope of this Thesis

The ability to disperse high aspect ratio nano-scale fillers, such as a layered-silicates, in polymer matrices has led to a host of non-trivial concurrent improvements in material properties of the resultant nanocomposites.[1][2][3][4] Nano-scale fillers often reduce the penalties for the incorporation of a filler by limiting the disruption of the polymer matrix, although they require sensitive tailoring of the thermodynamics for dispersion (mixing free energy).

For example, consider the classic case of polymer composite brittleness. Stiffness improvements in a conventional composite are typically associated with a high degree of embrittlement (up to 95 % reduction in elongation at break) at their normal loading levels (30-60 wt. %).[5] However, to obtain similar enhancements in stiffness, typically less than 10 wt. % nano-scale montmorillonite loading is required. Furthermore, as long as a percolated filler network is absent, the ductility of the nanocomposite is not impacted as severely as conventional composites.[6]

A significant portion of the nanocomposite literature focuses on 'soft-matrix' polymers, reporting excellent relative improvements; unfortunately, most have limited applicability to industrial applications. Similar nanocomposite approaches have substantially less success for high performance polymer matrices, as the improvements can be limited by poorly performing interfacial regions (polymer in/around the layered silicate). The development of new nanocomposite materials based on high-performance

polymers and exhibiting enhanced properties is particularly useful for improving current products, as well as introducing novel industrial applications. Thus, the focus of this thesis is on the creation of functional nanocomposite materials with superior properties such as the mechanical, crystallization, and degradation behaviors, where the polymer matrix is already a high-performance polymer.

The exploration and development of high-performance nanocomposites within this thesis focuses on two specific polymer matrices: a) poly(ethylene terephthalate) (PET) and b) polycarbonate (PC), as new applications for such materials have been targeted by industry. Since both PET and PC require high melt-blending temperatures, it is imperative to be mindful of the relative weak thermal stability of typical surfactants employed as nanofiller organic modifications (compared to the host matrices), to aid the dispersion of nanofillers [7] and the subsequent poor chemical resistance of PET and PC to such conventional surfactant degradation products.

Specifically, the goals of this work were:

1. pinpoint the general and specific mechanisms responsible for enhancement of material properties due to the dispersion of nanofillers;

2. elucidate the dispersive, mechanical, degradation, and crystallization behaviors of polymer/clay nanocomposites based on thermally stable alkyl-imidazole surfactants, as applied to high performance polymer matrices;

3. develop surfactant treatments that minimize the extent of matrix degradation during melt-blending and subsequently optimize the mechanical properties of such systems;

4.   produce and explicate the material behaviors of high-performance, dispersion tailored, polymer nanocomposite blends (focus on PET/PC immiscible blends);

Along these lines, the research depicted in this thesis is organized in the following manner:

Chapter 2   An overview of polymer/layered-silicate nanocomposites is given, including some of the fundamentals with respect to the general origin of property enhancements in polymer nanocomposites. Specifically, the roots of enhancements in the mechanical, crystallization, and fire performance properties of polymer/montmorillonite nanocomposites are outlined.

Chapter 3   Focusing on a high-temperature PET matrix, the performance of alternative high-thermal stability surfactant chemistry (alkyl-imidazole) was contrasted with a conventional (quaternary ammonium) surfactant. The morphology of the nanocomposite, the resultant crystallization behavior, and the mechanical performance are detailed. Differential scanning calorimetry (DSC) and polarized light optical microscopy (PLOM) were used to provide insights into the influence of the layered silicates on the crystallization of PET. The dispersion was also examined, and the mechanical properties were evaluated by tensile measurements and dynamic mechanical analysis (DMA).

Chapter 4   Focusing on the second high-temperature/high-performance polymer, PC, as the matrix for nanocomposites, the goal here was to develop a nanocomposite with controlled/limited matrix degradation. This was attempted by selecting appropriate surfactant chemistries, and was monitored by examining molecular

weight changes via gel permeation chromatography (GPC). The surfactant that provided the best combination of reduced matrix degradation and improved mechanical performance was then used to maximize the mechanical properties of the nanocomposite through montmorillonite platelet alignment via high shear forces, i.e. such as those developed during melt-blending.

Chapter 5   The phase behavior, crystallization, and mechanical properties of PET/PC blends were examined. The effects of the amorphous PC phases on the PET crystallization were examined in detail using PLOM and DSC. The mechanical properties were examined via tensile studies and DMA. Transesterification (copolymer) reactions were investigated via DSC, and ATR-FTIR.

Chapter 6   Novel PET/PC/montmorillonite nanocomposites were developed via melt-blending and were fully characterized in order to provide comprehensive insights into the material properties of these systems. Exhaustive studies were completed on the dispersive behavior of various organically modified layered silicates and the resulting phase morphologies of the nanocomposite blends. Quantification of the dispersion was completed via x-ray diffraction (XRD) with complementary transmission electron microscopy (TEM) analysis. Likewise, transesterification was monitored via modulated DSC, ATR-FTIR, and Raman Spectroscopy and the mechanical properties were examined by tensile studies.

Chapter 7   The crystallization behaviors of the novel PET/PC/montmorillonite nanocomposite blends were examined in order to highlight the influence of phase behavior on crystallinity and to explain the non-trivial improvements in mechanical performance. The effect of the amorphous PC, the incorporation of the layered silicate

particulates, and the modified phase morphology in general, were examined via DSC and PLOM analysis.

Chapter 8 An overall summary of this thesis with conclusive remarks to this body of work and guidance towards potential avenues for furthering this research are given.

References

1.   Alexandre, M. and Dubois, P., *Materials Science and Engineering* 2000; R28:1-63.

2.   Ray, S.S. and Okamoto, M., *Progress in Polymer Science* 2003; 28:1539–1641.

3.   Giannelis, E.P., Krishnamoorti, R., and Manias, E., *Advances in Polymer Science.* 1998; 138:107–148.

4.   Manias, E., Polizos, G., Nakajima, H., and Heidecker, M.J., **<u>Flammability of Polymer Nanocomposites.</u>** Editors: Wilkie and Morgan, Wiley & Sons, NJ, 2007.

5.   Karian, H.G., **<u>Handbook of Polypropylene and Polypropylene Composites.</u>** Marcel Dekker, New York, NY 1999.

6.   Manias, E., Touny, A., Wu, L., Strawhecker, K., Lu, B., and Chung, T.C., *Chemistry of Materials* 2001**;** 13:3516–3523.

7.   Xie, W., Gao, Z., Pan, W-P., Hunter, D., Singh, A., and Vaia, R., *Chemistry of Materials* 2001**;** 13:2979–2990.

Fundamentals and Flammability of Polymer/Clay Nanocomposites

2.1 Introduction

The marked improvement in mechanical and barrier properties, thermal stability, and flammability performance at low loading levels (< 5 wt. % inorganic content) in polymer/layered silicate nanocomposite materials has been well documented. Toyota was the first to report remarkable property enhancements in Nylon-6/montmorillonite (mmt) nanocomposites.[1][2][3] Differing from conventional composites, the improvements observed in polymer nanocomposites are most often observed without the characteristic accompanying sacrifices in other material properties (e.g. modulus/ductility trade-off in conventional composites), which in turn has helped foster the high expectations of polymer/nanofiller reinforced hybrid materials.

The potential applicability of such hybrid materials to industrial applications has pushed research into, perhaps, all commercially available polymer matrices.[4][5][6] Prior to discussion related to specific polymer systems, revelation of the fundamental origins of the improvement in mechanical, crystallization, and flammability characteristics of polymer nanocomposites shall be undertaken. This chapter shall be devoted to mainly theoretical arguments that define the origin of the properties of a polymer/layered silicate nanocomposite. A more comprehensive overview, which also

incorporated aspects of 1D fillers such as carbon nanotubes, has been published by this research group.[7]

2.2   Montmorillonite Filler

Preceding any fundamental discussion involving the properties of polymer/clay nanocomposites, we must first introduce the nano-filler itself. The studies presented within this thesis shall focus solely upon high-aspect ratio layered silicates (specifically montmorillonites) of the smectite group. In its pristine form, mmt is a hydrophilic 2:1 type phyllosilicate with a crystal lattice structure consisting of two silica tetrahedral sheets sandwiching a central alumina octahedral sheet (see **Figure 2.1**).[8]

Figure **2.1**
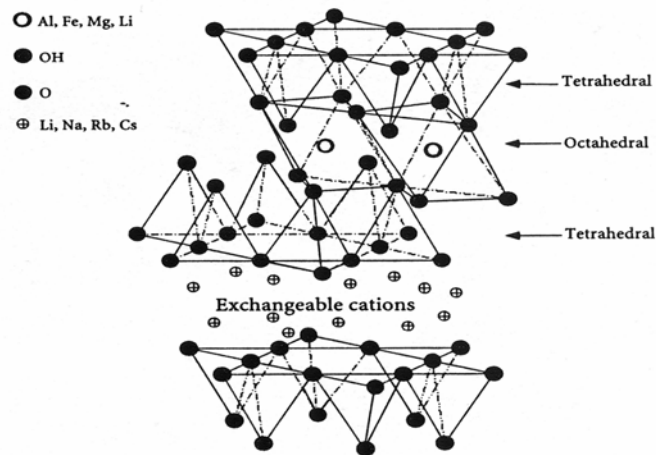
Figure **2.1**: Crystal structure of montmorillonite having an ideal chemical formula of $Al_4Si_8O_{20}(OH_4)·nH_2O$.[8] The silicon atoms in the centers of the tetrahedra are omitted for clarity.

The gallery of mmt, more commonly known as the interlayer spacing, is occupied by exchangeable cations (typically Na^+) and adsorbed water that undergoes dehydration up to temperatures of typically 150 °C.[9][10] Comprehensive thermal analysis indicates OH lattice water is liberated at much higher temperatures.[8] The basis of interest in mmt as a filler hinges upon several factors. The high negative surface charge and the existence of readily exchangeable cations within the interlayer spacing, allows for simple organic substitution (exchange), which can in turn provide thermodynamic compatibility between the host polymer matrix and the exchanged mmt filler. The cation exchange capacity (CEC), the number of readily exchangeable cations within the gallery, for a typical montmorillonite varies from approximately 70 to 150 meq/100 g. Also of central interest from a composite standpoint is the vast surface area of mmt (700 to 800 m^2/g) and its aspect ratio (which ranges from 10 to 1000, given the thickness of an individual layer is 0.97 nm).[11] When considered as a reinforcing agent for a polymer matrix, excitement is generated from the above characteristics and the ability to generate favorable energetics of mixing, which allow a filler whose tensile modulus has been estimated to be 180 to 265 GPa, to be dispersed within the much 'softer' polymer matrix.[12]

The typical improvement in tensile modulus (E) of polymer/mmt nanocomposites at loadings of less than 5 wt. % mmt is comparable in magnitude to a polymer matrix filled with 30 to 60 wt. % of conventional microscale fillers (talc, mica, chopped glass fibers, etc.).[13] Improvement of modulus for these same conventional composite systems can be accompanied by up to a 95 % reduction in elongation at break (i.e., develop a high degree of brittleness), whereas corresponding nanocomposite hybrids typically have less severe reductions and in some cases (such as polyolefin

nanocomposites) can even retain their ductility or even improve fracture toughness.[14][15] Furthermore, synergistic enhancements in other material behaviors such as fire retardancy and thermal stability (amongst other performance improvements) can also be achieved concurrently, depending on the polymer matrix and the composite structure.[4] These behaviors are generally dependent upon the development of an energetically-favored stable filler dispersion, such that the nano-scale filler may maximize its effectiveness. Without nanoscale dispersion of the layered silicate, the composite material developed will behave much like a conventional composite, with only modest enhancements in properties, if any, given the very low loadings employed.

2.3 'Thermodynamics of Dispersion'

The 'thermodynamics of mixing', the balance of entropic and enthalpic changes upon filler dispersion, dictate the dispersive characteristics of a given nanocomposite. A rather simple, yet highly effective, approach focusing on the entropic and enthalpic contributions to the free energy of mixing was published by Vaia and Giannelis.[16][17] The entropic contributions (penalty for confinement of the polymer chain within the gallery and the conformational entropy gain of the surfactant upon gallery expansion) are considered to be small, and as a first order approximation, are ignored here. Thus, favorable per-monomer enthalpic interactions are necessary in order to promote miscibility between a polymer and filler. Further simplification allows the enthalpic polymer/polymer, polymer/surfactant, and surfactant/surfactant interactions to be ignored as these are of comparable magnitude for most common polymers and surfactants. Based

on these considerations, and in the most simple of terms, the enthalpic driving force is considered to be rooted in the competitive adsorption of polymer and surfactant on the filler surface. Thus, when the polymer/filler interactions are more favorable than the surfactant/filler interactions, an excess interfacial tension is present, driving miscibility.

This can be quantified by the relation developed by Vaia and Giannelis (see **Equation 2.1)** based on the surface tension (γ) difference between a polymer (*p*) adsorbed on a layered silicate (*s*) and a surfactant (*a*) on the same layered silicate (*s*).

Equation **2.1**

$$\gamma_{excess}^{total} = \gamma_{ps} - \gamma_{as} \qquad \text{(Equation 2.1)}$$

This equation can be further expanded via the interfacial tension formalization of van Oss-Chaudhury-Good [**18**] as modified by Vaia for its application to polymer/organically modified montmorillonite (o-mmt) nanocomposites (see **Equation 2.2**). When assuming that the apolar (Lifschitz-van der Waals, γ^{LW}) and polar (γ^{AB}, e.g. electron donor/acceptor, also known as Lewis acid/base, γ^+/γ^-) contributions are additive, and by using standard geometric combination rules, we can rewrite the expressions of **Equation 2.1** using surface tension components readily found from literature (most often experimentally determined by contact angle measurements) in order to determine whether dispersion will occur by evaluating **Equation 2.2**.

Equation **2.2**

$$\gamma_{ij} = \gamma_{ij}^{LW} + \gamma_{ij}^{AB} \quad \text{with} \quad \left| \begin{array}{l} \gamma_{ij}^{LW} = \left(\sqrt{\gamma_i^{LW}} - \sqrt{\gamma_j^{LW}}\right)^2 \\ \gamma_{ij}^{AB} = 2\left(\sqrt{\gamma_i^+} - \sqrt{\gamma_j^+}\right)\left(\sqrt{\gamma_i^-} - \sqrt{\gamma_j^-}\right) \end{array} \right. \qquad \text{(Equation 2.2)}$$

A 'favorable excess' enthalpy is present when a negative interfacial tension difference occurs; this condition is satisfied for most common polymers with a simple alkyl-surfactant (see **Table 2.1** for common surface tension components from the literature). When favorable thermodynamics are lacking (such as in a polyolefin/alkyl-mmt system, where the excess enthalpy is exactly zero), thermodynamic 'tricks' need be employed in order to develop stable dispersions. For example, addition of favorable thermodynamics through either: (1) the modification of the polymer such that small quantities of polar/polarizable groups are added to the polymer chains (< 5 %), or (2) the modification of the mmt by the introduction of a low γ surfactant such as a fluoro-alkyl, have been shown to be effective in developing stable dispersions.[**15**]

Table **2.1**

Table **2.1**: Surface tension components (in mJ/m^2) commonly used to predict dispersion in various polymer nanocomposite systems.[**7**]

material	γ^{LW}	γ^+	γ^-
montmorillonite	66	0.7	36
alkane (C$_{12}$-C$_{18}$)	26	0	0
carbon nanotube	18.4	12	12
polypropylene	26	0	0
polyethylene	33	0	0
polystyrene	42	0	1.1
PMMA	40.6	0	12
PET	43.5	0.01	6.8
nylon 6,6	36.4	0.02	21.6

2.4   Nanocomposite Morphology

Novel material behaviors developed in polymer nanocomposites often arise from the change in the polymer behavior in and around the dispersed filler clusters (tactoids).

The degree and nature of this change is strongly dependent upon the overall dispersion of the filler and its effective surface area (surface area of a single mmt layer or of the dispersed tactoid). Thus, as a general rule of thumb, as the dispersion of the filler improves the subsequent degree of property enhancement follows suit.[7] Therefore, the immediate focus upon nanocomposite formation is determination of whether nano-scale dispersion did indeed occur. The most simple, quick, and widely used technique to probe dispersion at the nano-scale for polymer/layered-filler nanocomposites is wide-angle x-ray diffraction (XRD). However, XRD must be coupled with complementary bright-field transmission electron microscopy imaging (TEM) if definitive conclusions are to be drawn regarding the morphology of any nanocomposite. TEM provides morphological information not available from XRD, such as potential agglomeration of tactoids, tactoid size, and can verify the presence of exfoliated/delaminated fillers.

Three distinct morphologies are possible (see **Figure 2.2**) for a polymer nanocomposite. The first case is an intercalated morphology (**Figure 2.2a**) in which the clay gallery is penetrated and swelled by a few chains of the host polymer yet retains long range order of the parallel registry (also known as the 'deck of cards' structure). An intercalated morphology is indicated during XRD analysis when a shift in the Bragg peak position takes place (peak shifts to lower values of 2θ) when comparing the pure organo-mmt to the subsequent nanocomposite. Bragg's law of diffraction (see **Equation 2.3**) is used to determine the interlayer spacing of an intercalated nanocomposite, where n is an integer (order of *hkl* diffraction), λ is the wavelength of the x-ray source (typically Cu K_{α}, where $\lambda = 1.541$ Å), d is the spacing between the *hkl* crystalline planes, and θ is the angle between the incident ray and the corresponding *hkl* scattering planes.[19]

Figure **2.2**

a) intercalated   b) exfoliated/delaminated

c) microcomposite
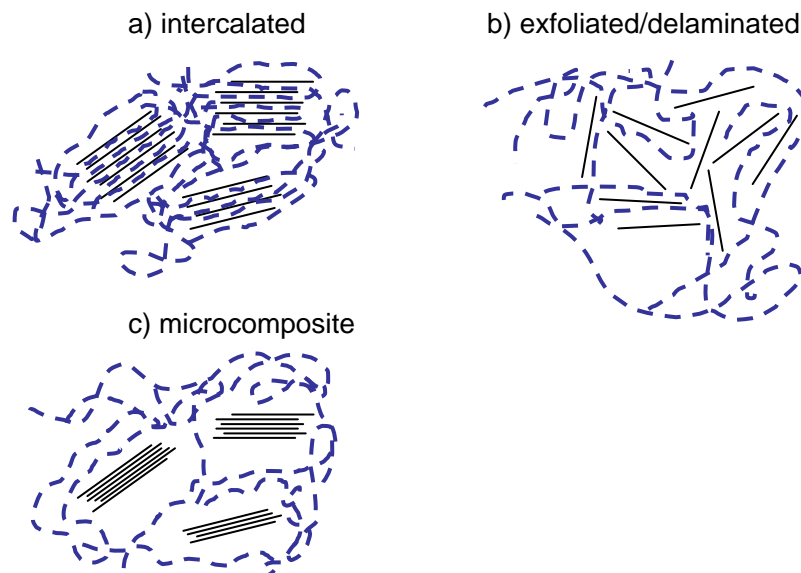
Figure **2.2**: Potential dispersive behaviors developed upon nanocomposite formation.

Equation **2.3**

$$n\lambda = 2d \times \sin\theta \qquad \text{(Equation 2.3)}$$

The second idealized structure is an exfoliated nanocomposite in which the host polymer matrix penetrates the clay gallery and is able to separate the tactoids (stacks) into individual layers, which have no long-range order or parallel stacking (**Figure 2.2b**), and this structure is manifested by a d_{001}-silent XRD trace, which *must* be confirmed by TEM.

The final morphology is termed a microcomposite, and represents the case where no polymer has penetrated the clay gallery, resulting in a dispersion much like that of a conventional composite (**Figure 2.2c**). A microcomposite is indicated by XRD where the interlayer spacing remains constant or is reduced after mixing with polymer (the d_{001} Bragg peak position remains the same or shifts to higher values of 2θ).

2.5   Theoretical Limitation of Mechanical Property Improvement

Theoretical models for predicting the mechanical properties that are applicable to conventional composites systems, such as the Halpin-Tsai [20] and Mori-Tanaka [21] models, fail when directly applied to nanocomposite systems. This is related in part to the inability of the models to account for the dispersion of the layered silicate, the buckling of the filler platelets, and the non biaxial in-plane filler orientation.[7] Attempts have been made to modify the Halpin-Tsai [22] model to account for such instances, and despite these efforts, the model is still lacking in its predictive power over a broad range of polymer matrices. Other models have been proposed and are similar poor predictors or require further modification for each individual matrix when applied across multiple polymers.[23][24]

The commonalities amongst the more successful of these theoretical approaches are the general factors impacting the mechanical behaviors of polymer/nano-scale filler composites. Specifically: (1) the effective filler aspect ratio and the effective filler volume fraction when incomplete dispersion (e.g. intercalated rather than complete exfoliation) occurs, which in turn reduces the efficiency of the mmt filler; (2) filler-specific mechanisms of deformation and fracture can have considerable contributions to the mechanical properties of the respective nanocomposite; and (3) the correct enumeration of the interfacial strength between the polymer and filler is crucial for the correct estimation of the mechanical properties of the composite; this last value, which is substantially smaller compared to the modulus of the filler, can dramatically limit the reinforcing effectiveness of the nano-scale filler.[7]

Upon examining experimental data of polymer/mmt nanocomposites systems with favorable dispersion, we often find remarkable relative enhancements in the tensile modulus of the nanocomposite (compared to the respective unfilled/bulk polymer). A good example is the 300% improvement in modulus observed in a crosslinked poly-dimethylsiloxane (PDMS)/alkyl-ammonium mmt nanocomposite when just 0.04 vol. % of organo-mmt is dispersed within the polymer matrix (see **Figure 2.3**).[**25**]

Figure **2.3**
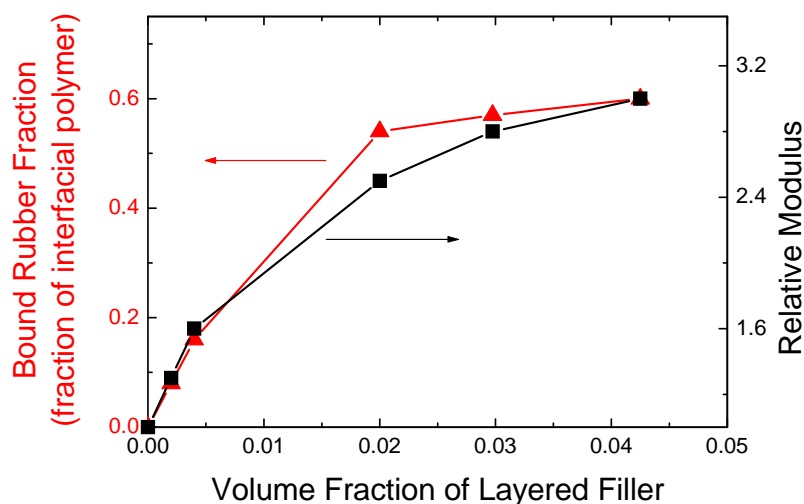
Figure **2.3**: A PDMS/alkyl-ammonium nanocomposite develops a substantial increase in the relative tensile modulus at low loadings, and the corresponding fraction of interfacial polymer increases in a similar manner.[**25**]

Other examples exist in which polymer matrix nanocomposites exhibit relative modulus improvements of similar magnitudes.[**26**][**27**] However, the promise of such great improvements is not realized for all polymer matrices. If we examine polyolefin nanocomposites, for example, we find particularly interesting results. When a thermodynamically stable polyethylene (PE) nanocomposite is produced via melt-

blending, the relative modulus improves by 78 % at 3 % organo-mmt loading (see
Table 2.2). When compared to polypropylene, a nearly identical polymer matrix from a
thermodynamics of dispersion (enthalpic) standpoint, with a comparable dispersion of the
organo-mmt, we find that the relative improvement in tensile modulus is suppressed
(only 18 % compared to the 78 % of the PE nanocomposite at the same mmt loading).

Table **2.2**

Table **2.2**: Comparison of the mechanical properties of maleic anhydride functionalized
PE/organo-mmt and PP/organo-mmt nanocomposites prepared by twin-screw extrusion
and subsequent injection molding.[**30**]

Polyethylene (PE)	Tensile Modulus (MPa)	Increase in Modulus (%)	Tensile Strength (MPa)	Elongation at Break (%)
Unfilled	330 (± 5)	-	24 (± 1)	291 (± 5)
3% organo-mmt	590 (± 9)	78	23 (± 1)	325 (± 11)
9% organo-mmt	1120 (± 25)	240	23 (± 1)	285 (± 23)
Polypropylene (PP)				
Unfilled	1630 (± 50)	-	39 (± 1)	368 (± 21)
3% organo-mmt	1920 (± 16)	18	38 (± 1)	224 (± 17)
6% organo-mmt	2190 (± 42)	34	39 (± 1)	203 (± 21)

One distinct difference between the two matrices is the matrix modulus; unfilled
PE has an as-molded modulus on the order of 0.3 GPa whereas unfilled PP has an as-
molded modulus on the order of 1.6 GPa. The strong correlation between the interfacial
polymer fraction and modulus of the PDMS nanocomposites, coupled with the variance
of the modulus of the two unfilled polyolefins, leads to the conclusion that the limitation
in improvement in mechanical properties of these nanocomposites is not stiffness of the
filler itself, but is the interfacial strength of the polymer/filler interface.[**7**]

Examples do exist in stiff polymer matrix nanocomposites, such as Nylon, in
which despite a starting modulus of over 2 GPa, relative improvements approaching

200 % at low loading levels are possible.[28] It is believed that Nylon-6/mmt nanocomposites owe their vast improvement in modulus to the improved stress transfer from the polymer matrix to the filler, mediated by the strong hydrogen bonding that takes place between the polymer and the filler.[7] Nylon has the potential to hydrogen bond to the silicate surface, which creates the impetus for the significant improvement in the interfacial strength of the nanocomposite, leading to the rise in relative modulus. Molecular weight has no effect on the relative modulus improvement, as the relative modulus is dependent upon the polymer/filler interfacial strength, and not on the modulus of the polymer or of the filler (see **Figure 2.4**).[28]

Figure **2.4**
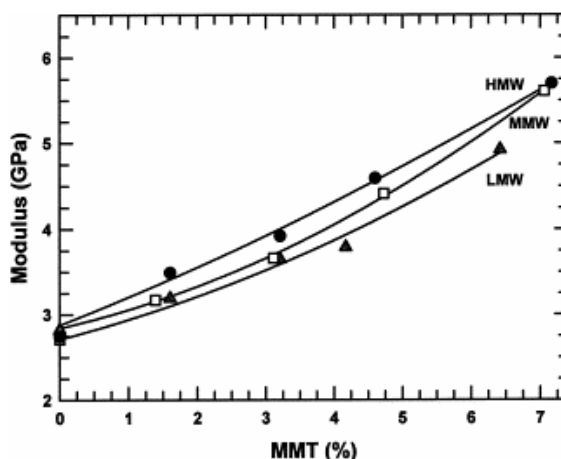
Figure **2.4**: Molecular weight effects on modulus of Nylon-6/mmt nanocomposites.[28]

Strengthening of a polymer/filler interface may also take place by: (1) covalently bonding the polymer to the filler, and/or by (2) the addition of polar groups across the polymer.[29] Epoxies are a prime example of a stiff matrix polymer that may benefit from the development of a reactive mmt filler, through covalent bonding between polymer and filler. The addition of 6 wt. % of a commercially available alkyl-ammonium

mmt led to a 20% improvement in the stiffness of an epoxy matrix, yet when a reactive mmt filler is used the relative improvement rises to 53 %.[**30**]

2.6   Filler-Induced Polymer Crystallization Behaviors

The introduction of the high-aspect ratio inorganic mmt filler in polymer/mmt nanocomposites can lead to improved mechanical properties. At the same time, the crystallization behavior of the polymer matrix is also impacted by the incorporation of nano-scale fillers. Filler-induced effects on polymer crystallinity may be broken down in two general categories: (1) behaviors specific to a polymer, or class of polymers, and (2) general behaviors observed across most crystallizable polymer systems.[**7**]

2.6.1   Polymer Specific Crystallization Behaviors

New crystal structures have been observed in certain polymer nanocomposites such as Nylon-6/mmt [**31**][**32**][**33**] and poly(vinyl alcohol)/mmt [**34**][**35**]. Specifically, when strong specific interactions between the filler and the polymer exist, often a crystal form not normally associated with the bulk polymer crystal structure (under normal crystallization conditions) will occur in the vicinity of the filler. For example, the γ-crystal phase of Nylon-6 is promoted next to the mmt filler, as a result of the strong hydrogen bonding of the amide groups with the silicate surfaces.[**31**] When the inorganic fillers promote the growth of non-bulk crystal phases, the thermal and mechanical properties can be improved when the surface-nucleated crystal phase has better

mechanical and thermal characteristics than the bulk crystal phase.[7] Again, the prime example of such a case, in which the large surface area of the filler promotes enhancements of the materials properties through a filler-promoted novel crystal morphology, would be Nylon-6/mmt nanocomposites.

The polymer can also, in a less prevalent case, become amorphized by the presence of mmt filler. Specifically, in the case of poly(ethylene oxide) (PEO)/Na$^+$ mmt nanocomposites, near the filler surface the strong coordination of the PEO to the Na$^+$ cations of the mmt promotes non-crystalline ether crown PEO conformations, resulting in a highly amorphous polymer structures near the filler surface.[36]

2.6.2   General Crystallization Behaviors

The general effects on polymer crystallinity associated with the incorporation of the nano-scale fillers are rooted in the nucleation and crystallization kinetics and are applicable to most crystallizable polymer matrices. Heterogeneous nucleation is the most common behavior associated with the layered silicates. Second, the number of filler tactoids is proportional to the nucleation density – as the number of tactoids increases, so follows the number of nuclei. Third, the linear growth rate is retarded and most often characterized by a two to four fold reduction in the rate, independent of the nucleation mechanism.

A decrease in the spherulite size is also independent of polymer system/class and is found to correlate with the discontinuity in space created by the inorganic filler (*cf.* the increased nucleation density). The spherulite must have a size comparable to the filler-

filler separation, independent of the bulk polymer spherulite size, which leads to reduced crystal sizes for typical filler loadings and good dispersions.[7]

2.7   Improved Flammability Characteristics of Polymer/Clay Nanocomposites

Recent concerns over the toxicity of the most common flame retardant additives, halogenated compounds – more specifically brominated additives – has hastened the search for non-toxic alternatives to improve the flammability characteristics of polymer materials.[37][38] The addition of a dispersed inorganic layered silicate leads in most cases to an enhancement in the Fire Resistance (FR) character of a nanocomposite hybrid.[39] However, when compared directly to a system in which the layered silicate acts as a replacement for a brominated FR additive, nanocomposite formation alone is insufficient in developing the degree of FR resistance required by commercial applications, e.g. cannot pass stringent tests such as the Underwriters Laboratory (UL) vertical burn test (UL-94).[39]

2.7.1   Halogenated FR Mechanism

Halogenated compounds owe their effectiveness as FR additives to a flame poisoning mechanism, with brominated compounds being the most successful due to their overall stability and favorable radical liberation temperature during combustion/thermal-degradation.[40][41] The flame poisoning mechanism is due to a halogen radical joining free hydrogen to form a hydrogen halide, which in turn reacts with the high energy

hydroxyl radicals (the 'fuel' for the combustion process) to produce water and bromine radicals. The reaction cycle of the halogen is understood to be cyclic, leading to eventual starvation of the combustion reaction from the lack of high-energy hydroxyl radicals, producing a self-extinguishing behavior.[41]

2.7.2   Nanocomposite FR Mechanism

Previous discussion indicated the addition of an inorganic layered silicate alone is not recognized as imparting the same degree of enhancement in the fire suppression characteristic of a material as halogenated compounds. The difference in FR characteristics can find its origin centered on the differences in the FR mechanism. Improved FR behavior for polymer nanocomposites, as first proposed by Gilman [42], has been traced to the formation of a multilayer carbonaceous char layer during combustion. This char layer has dual functionality as an insulator and a mass transport barrier – preventing exposure of the underlying virgin polymer layer to the combustion process and inhibiting the high energy radicals ('fuel') from reaching the surface. Vaia reiterates the mechanism and the char layer functionality while providing a comprehensive characterization of a model char layer through scanning electron microscopy (SEM) of a Nylon-6/mmt nanocomposite exposed to solid-rocket motor exhaust (see **Figure 2.5)**.[43] The char layer is characterized as porous with solid regions; the toughness, thickness, and homogeneity of the char layer typically increase with increasing silicate content (at low loading levels) as dispersion of the nano-scale filler becomes more uniform.

Figure **2.5**
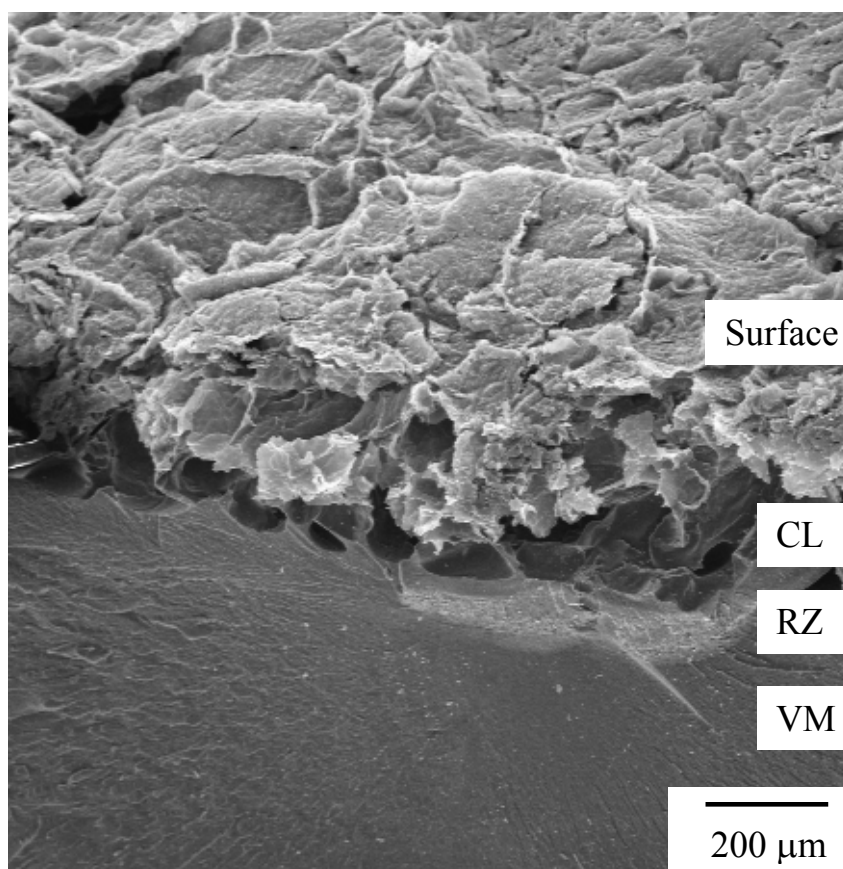
Figure **2.5**: SEM image of a Nylon-6/mmt nanocomposite exposed to solid-rocket motor exhaust. The cross section contains the (a) surface region, (b) carbonaceous char layer (CL), (c) the reaction zone (RZ), and (d) the virgin material (VM).[**43**]

The FR behavior of a nanocomposite is influenced by the dispersion of the layered silicate within the hybrid. Without nano-scale dispersion coupled with a uniform distribution of the clay tactoids, char layer formation will become hindered, reducing the effectiveness of the inorganic filler as an FR alternative.[**43**][**44**] Likewise, the development of a novel degradation mechanism or a change in the existing degradation pathway for the polymer matrix during combustion may also influence the FR characteristics of the nanocomposite.[**45**][**46**]

2.7.3   Enhancements in Nanocomposite FR

The most common technique available to measure the combustion characteristics of a polymer material is the Cone Calorimeter (CC). In a CC test, a thermal insult is applied to a standard test specimen upon which the ignition time (T_{ign}), heat release rate (HRR), peak heat release rate (PHRR), and certain evolved gasses can be monitored.[47]

Figure **2.6**
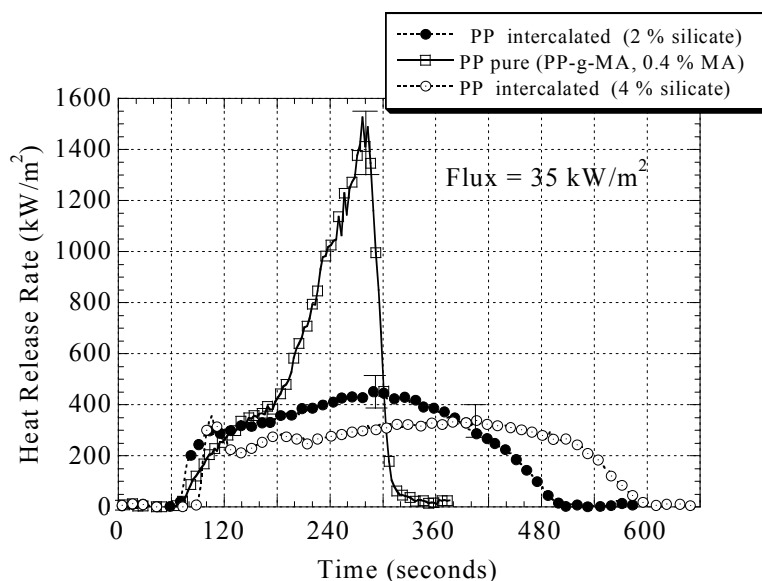
Figure **2.6**: Cone Calorimeter study of intercalated PP-g-MA/mmt nanocomposites.[48]

The metric for comparison between the bulk material and the corresponding nanocomposite is most often the PHRR (also known as the explosiveness of combustion). For example, when favorable dispersion is developed in an intercalated PP-graft-maleic anhydride nanocomposite, the PHRR is reduced by 75 % from about 1600 kW/m^2 to approximately 400 kW/m^2 (see **Figure 2.6**).[48]

Depending on the polymer matrix of interest, improvements on the order of 20 % to 80 % are rather common when favorable dispersion is achieved (see **Table 2.3**). Also, as the filler loading level continues to increase, the PHRR is further reduced. Again, nanocomposite formation alone will not produce a self-extinguishing behavior – except in Nylon-6/mmt nanocomposites, in which the highest UL rating for vertical burn (UL-94, V-0) was achieved.

Table **2.3**

Table **2.3**: Cone calorimeter PHRR data for common polymer/mmt nanocomposites (applied cone flux of 50 kW).[**39**]

Polymer Matrix	Filler Loading (%)	Morphology	PHRR (kW/m^2)	Reduction from Bulk (%)
Nylon-6	2	Intercalated	1212	41
Nylon-6	5	Intercalated	679	67
Nylon-6	10	Intercalated	446	78
PS	5	Exfoliated	537	72
PP-g-MA	5	Intercalated/Exfoliated	724	74
EVA	5	Intercalated/Exfoliated	597	66
EVA	5	Immiscible	1138	36
Epoxy (anhydride)	5	Intercalated	984	20

2.8   Appendix

Several publications detailing the FR behaviors polymer/nano-scale filler reinforced nanocomposites were prepared in conjunction with this thesis. The full abstracts of each publication are listed in this appendix.

2.8.1 The Thermal Degradation of Poly(methyl methacrylate) Nanocomposites with Montmorillonite, Layered Double Hydroxides, and Carbon Nanotubes

The thermal degradation of poly(methyl methacrylate) and its nanocomposite has been studied to determine if the presence of clays (anionic and cationic) or carbon nanotubes has an effect on the degradation pathway. Nanocomposite formation has been established by X-ray diffraction and transmission electron microscopy, thermal degradation has been investigated by cone calorimetry and thermogravimetric analysis (TGA), and the products of degradation have been studied with TGA/FT-IR and gas chromatography/mass spectrometry (GC/MS). There are no marked differences in the degradation products of the polymer and its nanocomposites, but the degradation of the nanocomposite occurs at higher temperatures. The most likely explanation is that poly(methyl methacrylate) degrades by only a single route, so the clay cannot promote one pathway at the expense of another. This observation bears important implications for the barrier mechanism, which is currently used to explain the reduction in the peak heat release rate of nanocomposites.[49]

2.8.2 Preparation and Characterization of Poly(ethylene terephthalate)/Clay Nanocomposites by Melt Blending using Thermally Stable Surfactants

Poly(ethylene terephthalate) (PET)/clay nanocomposites were prepared by melt blending and their morphologies and properties were investigated through X-ray diffraction, bright field transmission electron microscopy, thermogravimetric analysis and cone calorimetry. Three clays were comparatively studied—montmorillonite, hectorite and magadiite — all organically modified with thermally stable surfactants developed in

this laboratory. Two such organic modifications were investigated, alkyl-quinolinium surfactants and vinylbenzyl-ammonium containing copolymers; both organic modifications combine high enough degradation temperature to allow for melt processing with PET, and also favorable thermodynamics for nanocomposite formation with PET. All nanocomposites showed about the same value for the peak heat release rate (PHRR). The amount of char increases after nanocomposite formation and this could account for the PHRRs.[**50**]

2.8.3 Benzimidazolium Surfactants for Styrenic Polymers

Nanocomposites of polystyrene (PS), acrylonitrile-butadiene-styrene copolymer (ABS) and high impact polystyrene (HIPS) were prepared with two new homologous benzimidazolium surfactants. The morphology of the polymer/clay hybrids was evaluated by X-ray diffraction (XRD) and transmission electron microscopy (TEM), showing good overall dispersion of the clay. The thermal stability of the polymer/clay nanocomposites was enhanced as evaluated by thermogravimetric analysis. From cone calorimetric measurements, the peak heat release rate of the nanocomposites was decreased by about the same amount as seen for other organically-modified clays.

2.8.4   The Influence of Carbon Nanotubes, Organically Modified Montmorillonites and Layered Double Hydroxides on the Thermal Degradation of Polyethylene, Ethylene-Vinyl Acetate Copolymer and Polystyrene

Nanocomposites of polyethylene, ethylene-vinyl acetate copolymer and polystyrene with single and multi-wall carbon nanotubes, organically modified montmorillonites and layered double hydroxides were prepared by melt-blending. Their morphologies were assessed by X-ray diffraction and transmission electron microscopy, while the flammability properties were evaluated by thermogravimetric analysis and cone calorimetry. The relative amounts and the identity of the degradation products are changed when both well-dispersed cationic and anionic clays are used, but there are no differences in the degradation products when carbon nanotubes were utilized. When the nano-dimensional material is not well-dispersed, the degradation products are not changed. Unlike their smectite counterparts, polymer/LDH nanocomposites give reasonably good reductions in peak heat release even when good nano-dispersion has not been obtained. These data suggest that the enhancement in the fire behavior must be, at least in part, due to different mechanisms for montmorillonite, layered double hydroxides and carbon nanotube-based nanocomposites.

References

1.   Usuki, A., Kojima, Y., Kawasumi, M., Okada, A., Fukushima, Y., Kurauchi, T., and Kamigaito, O., *Journal of Materials Research* 1993; 8:1179–1184.

2.   Kojima, Y., Usuki, A., Kawasumi, M., Okada, A., Fukushima, Y., Kurauchi, T., and Kamigaito, O., *Journal of Materials Research* 1993; 8:1185–1189.

3.   Kojima, Y., Usuki, A., Kawasumi, M., Okada, A., Kurauchi, T., and Kamigaito, O., *Journal of Journal of Polymer Science Part A: Polymer Chemistry* 1993; 31:983–986.

4.   Alexandre, M. and Dubois, P., *Materials Science and Engineering* 2000; R28:1–63.

5.   Ray, S.S. and Okamoto, M., *Progress in Polymer Science* 2003; 28:1539–1641.

6.   Giannelis, E.P., Krishnamoorti, R., and Manias, E., *Advances in Polymer Science.* 1998; 138:107–148.

7.   Manias, E., Polizos, G., Nakajima, H., and Heidecker, M.J., **Flammability of Polymer Nanocomposites.** Editors: Wilkie and Morgan, Wiley & Sons, NJ, 2007.

8.   Grim, E., **Clay Mineralogy.** McGraw-Hill, New York, NY 1953 pp. 55–64.

9.   Mackenzie, R.C., **The Differential Thermal Investigation of Clays.** Alden Press, London, England 1966 p. 143.

10.   Balek, V., Malek, Z., Yariv, S., Matuschek, G., *Journal of Thermal Analysis and Calorimetry* 1999; 56:67–76.

11.   Theng, B.K., **Formation and Properties of clay-polymer complexes.** Elsevier Scientific Publications, New York, NY 1979.

12.   Chen, B. and Evans, J.R.G., *Scripta Materialia* 2006; 54:1581–1585.

13.   Karian, H.G., **Handbook of Polypropylene and Polypropylene Composites.** Marcel Dekker, New York, NY 1999.

14.   Zerda, A.S. and Lesser, A.J., *Journal of Polymer Science: Part B: Polymer Physics* 2001; 39:1137–1146.

15.   Manias, E., Touny, A., Wu, L., Strawhecker, K., Lu, B., and Chung, T.C., *Chemistry of Materials* 2001**;** 13:3516–3523.

16.   Vaia, R.A. and Giannelis, E.P., *Macromolecules* 1997; 30:7990–7999.

17.   Vaia, R.A. and Giannelis, E.P., *Macromolecules* 1997; 30:8000–8009.

18.   Van Oss, C.J., Chaudhury, M.K., and Good, R.J., *Chemical Reviews* 1988; 88:927–941.

19.   Cullity, B.D. and Stock, S.R., **Elements of X-Ray Diffraction,** Prentice Hall, Upper Saddle River, NJ, 2001.

20.   Halpin, J.C. and Finlayson, K.M., **Primer on composite materials analysis**, Technomic Publication Company, Lancaster, PA, 1992.

21.   Mori, T. and Tanaka, K., *Acta Metallurgica* 1973; 21:571–574.

22.   Brune, D.A. and Bicerano J., *Polymer* 2002; 43:369–387.

23.   Wang, J. and Pyrz, R., *Composites Science and Technology* 2004; 64:925–934.

24.   Wang, J. and Pyrz, R., *Composites Science and Technology* 2004; 64:935–944.

25.   Burnside, S. and Giannelis, E.P., *Chemistry of Materials* 1995; **7**:1597–1600.

26.   Xu, R., Manias, E., Snyder, A.J., and Runt, J., *Macromolecules*, 2001; 34:337–339.

27.   Xu, R., Manias, E., Snyder, A.J., and Runt, J., *Journal of Biomedical Materials Research* 2003; 64A:114–119.

28.   Fornes, T.D., Yoon, P.J., Keskkula, H., and Paul, D.R., *Polymer* 2001; 42:9929–9940.

29.   Wang, Z.M., Nakajima, H., Manias, E., and Chung, T.C., *Macromolecules* 2003; 36:8919–8922.

30.   Unpublished data from the Manias Research group

31.   Lincoln, D.M., Vaia, R.A., Wang, Z-G., Hsiao, B.S., and Krishnamoorti, R., *Polymer* 2001; 42:9975–9985.

32.   Lincoln, D.M., Vaia, R.A., Wang, Z-G., and Hsiao, B.S., *Polymer* 2001; 42:1621–1631.

33.   Lincoln, D.M. and Vaia, R.A., *Macromolecules* 2004; 37:4554–4561.

34.   Strawhecker, K. and Manias, E., *Chemistry of Materials* 2000; 12:2943–2949.

35.   Strawhecker, K. and Manias, E., *Macromolecules* 2001; 34:8475–8482.

36.   Strawhecker, K. and Manias, E., *Chemistry of Materials* 2003; 15:844–849.

37.   Meerts, I.A.T.M., van Zanden, J.J., Luijks, E.A.C., van Leeuwen-Bol, I., Marsh, G., Jakobsson, E., Bergman, A., and Brouwer, A., *Toxicoligical Sciences* 2000; 56:95–104.

38.   Eriksson, P. and Fredriksson, A., *Environmental Toxicology and Pharmacology* 1998; 5:17–27.

39.   Gilman, J.W., Kashiwagi, T., Morgan, A.B., Harris, R.H., Brassell, L., VanLandingham, M., and Jackson, C.L., *NISTIR 6531* 1–55.

40.   Bhaskar, T., Matsui, T., Uddin, M.A., Kaneko, J., Muto, A., and Sakata, Y., *Applied Catalysis B: Environmental* 2003; 43:229–241.

41.   Kaspersma, J., Doumen, C., Munro, S., and Prins, A-M., *Polymer Degradation and Stability* 2002; 77:325–331.

42.   Gilman, J.W., *Applied Clay Science* 1999; 15:31–49.

43.   Vaia, R.A., Price, G., Ruth, P.N., Nguyen, H.T., and Lichtenhan, J., *Applied Clay Science* 1999; 15:67–92.

44.   Qin, H., Su., Q., Zhang, S., Zhao, B., and Yang, M., *Polymer* 2003; 44:7533–7538.

45.   Jang, B.N. and Wilkie, C.A., *Polymer* 2005; 46:2933–2942.

46.   Jang, B.N. and Wilkie, C.A., *Polymer* 2005; 46:3264–3274.

47.   Mai, Y-M., and Yu, Z-Z., **Polymer nanocomposites,** CRC Press, New York, NY 2006.

48.   Gilman, J.W., Jackson, C.L., Morgan, A.B., Harris, R., Manias, E., Gianellis, E.P., Wuthenow, M., Hilton, D., and Phillips, S.H., *Chemistry of Materials* 2000; 12:1866–1873.

49.   Costache, M.C., Wang, D., Heidecker, M.J., Manias, E., and Wilkie, C.A., *Polymers for Advanced Technologies* 2006; 17:272–280.

50.   Costache, M.C., Heidecker, M.J., Manias, E., and Wilkie, C.A., *Polymers for Advanced Technologies* 2006; 17: 764–771.

Chapter 3

Structure and Properties of Melt-Blended Poly(ethylene terephthalate)/Montmorillonite Nanocomposites

3.1   Summary

The crystallization, mechanical, and thermal degradation behavior of melt-blended homopolymer poly(ethylene terephthalate) (PET)/layered silicate nanocomposites were investigated. We compared homopolymer PET nanocomposites with a thermally stable alkyl-imidazole surfactant to those having a conventional alkyl-ammonium surfactant. We also evaluated the respective behaviors of crystallizable PET (homopolymer) nanocomposites with copolymer PET nanocomposites, when similar thermally stable surfactants were used for nanofiller modification. Crystal growth in the PET nanocomposites was evaluated, and we found similar behaviors in the homopolymer and copolymer nanocomposites. The high aspect-ratio mmt filler served as a strong nucleating agent, facilitating heterogeneous nucleation, and led to an increase in the nuclei density and the overall crystallization temperature. However, the spherulite size and linear crystal growth rate of the PET were reduced upon mmt addition.

3.2   Introduction

The potential of improved materials properties in polymer/layered silicate nanocomposites was briefly discussed within **Chapter 2** of this thesis. The

literature [1][2][3] also provides many instances that make a compelling case for efforts to produce well-dispersed polymer nanocomposites. This is especially the case for high performance polymers, such as PET, in which improvements in barrier/transport properties, stiffness, and flammability could potentially push the envelope of performance for organic/polymeric materials, and allow for new products and markets from an industrial standpoint. PET is known as a slow-crystallizing polymer, typically used in textiles or food and beverage storage applications.[4] Thus, the crystallization of PET must be well-controlled, especially when blow molding or thermoforming are the final processing steps. Homopolymer PET (crystallizable PET), the basis of this work, is generated by the esterification reaction between terephthalic acid and ethylene glycol or the transesterification reaction between ethylene glycol and dimethyl terephthalate. The crystallization behavior of the homopolymer PET, can be readily altered by the formation of a copolymer PET (co-PET), in which the addition of a crystallization-inhibiting co-monomer (such as cyclohexane dimethanol) can be utilized to control the polymer crystallization.

Layered silicates, in this case a montmorillonite (mmt), intended for nanofillers in organic matrices, are modified with organic cationic surfactants; most commercial examples employ quaternary ammonium surfactants as the surface treatment, since these surfactants can promote compatibility with a wide range of polymers, they were previously made in industrial/commercial scales as viscosity modifiers for the paint industry, and they can be very economically attractive when naturally occurring alkyl-ammoniums are used. However, in the case of engineering polymers with high melt-processing temperatures (e.g. PET, polycarbonate, syndiotactic polystyrene, etc., all

processed above 250°C) conventional alkyl-ammonium surfactants are not ideal, since they readily undergo thermal degradation during melt-processing of the polymer nanocomposite [5]. This is detrimental to the host polymer in two aspects: (a) the elimination of the surfactant leads to loss of compatibility (dispersion) between polymer and layered silicate, typically manifested through a gallery collapse and limited nano-scale filler dispersion, and (b) depending on the polymer matrix, the potential for significant molecular weight degradation [6][7], when exposed to the surfactant degradation products. Attempts to overcome the limited thermal stability of ammonium surfactants have been made, by replacing the ammonium group with phosphonium, pyridinium, or imidazolium. For example, alkyl-imidazolium based surfactants as modifications for mmt, have been successfully utilized in Nylon-6, syndiotactic polystyrene (s-PS), and PET nanocomposites.[8][9]

Alternatively, other efforts for the preparation and characterization of PET/mmt nanocomposites, have focused on PET/alkyl-ammonium-mmt nanocomposites prepared by in-situ-polymerization and/or solution blending of polymer and organo-filler to avoid the thermal degradation of the surfactant.[10][11][12][13] The resultant morphological and crystallization behaviors reported, show that the addition of layered silicates nanofillers increased heterogeneous nucleation during crystallization, reduced spherulite sizes when comparing to the bulk, and occasionally promoted irregularly-shaped rod-like immature spherulites, which were attributed to the high aspect ratio of the layered silicates.[12][13] As previously discussed, little has been completed with respect to the resultant mechanical behaviors upon nanocomposite formation.

This study focuses on the preparation of a high-thermal stability alkyl-imidazole surfactant for the mmt, to enable melt-blended (twin screw extrusion + injection molding) homopolymer-PET/organically-modified-montmorillonite nanocomposites. In addition, a commercially available mmt nanofiller, exchanged with a conventional quaternary ammonium surfactant will be compared side-by-side. Thus, our objectives are to (a) elucidate the effect of mmt on the crystallization behavior of homopolymer PET, (b) comment on the effect of mmt addition on the mechanical properties and thermal degradation behaviors of PET, and (c) link behaviors observed in co-PET/thermally stable mmt nanocomposites (prepared in an independent study) to those of the homopolymer PET/mmt (from this study).

3.3   Experimental

3.3.1   Materials

A high molecular weight, high intrinsic viscosity (M_n = 35 kg mol^{-1}, IV = 0.95 dL/g) homopolymer PET was obtained from Voridian (grade 12822). Na$^+$ montmorillonite (PGW) with a cation exchange capacity (CEC) of 1.4 meq/g was obtained from Nanocor. Synthesis of the thermally stable alkyl-imidazole surfactant was completed in this lab: Tetrahydrofuran, 1-Iodooctadecane, Hexane, and Imidazole were purchased and used as received from Sigma Aldrich. A 250 mL flask with a constant nitrogen purge was fit with a reflux condenser and a temperature controlled oil bath. Imidazole (5.87 x 10^{-2} moles, 4.0 g) was placed in the flask and dissolved in 200 mL of

Tetrahydrofuran (THF). 1-Iodooctadecane (5.87×10^{-2} moles, 22.3 g) was then added to the flask while stirring at 55 °C. The reaction was allowed to take place for 12 hours under stirring and constant nitrogen purge with the temperature held between 55 °C to 60 °C. The resultant solution was dried in air (THF removed). The yellow solid was then dried under vacuum at room temperature for 4 hours to remove residual THF. The solid was then washed and filtered three times with 100 mL of hexane. The average yield per batch of surfactant was 59.5 %.

The alkyl-imidazole mmt (imm-mmt) was exchanged by the cation exchange reaction of the PGW with an excess of the surfactant. 40 g of PGW was dispersed in distilled water (50 mL/gram) at 50 °C with mechanical stirring for one hour in a 4L beaker. A 50 % excess of the surfactant (38.9 g – 84 meq of surfactant) was dissolved in ethanol at 50 °C and was fully protonated by the addition of 8.2 g of hydrochloric acid while under mechanical stirring for one hour. The surfactant solution was then quickly added to the PGW solution while vigorous stirring was maintained, and was allowed to react for 12 hours at 50 °C. The imm-mmt was collected by filtration. The unbound excess surfactant was removed by washing the imm-mmt in hot ethanol (2000 mL, 50 °C) for two hours a total of eight times, to ensure complete removal of the unbound surfactant. After the final filtration, the imm-mmt was dried in vacuum at 80 °C for 12 hours prior to thermogravimetric analysis.

A commercially available organo-mmt, Cloisite 25A (C25A), with a CEC of 0.95 meq/g modified with dimethyl, hydrogenated-tallow, 2-ethylhexyl quaternary ammonium surfactant was used as received from Southern Clay Products. The structures of the surfactants and the polymer can be found in **Appendix 3.6.1**.

3.3.2 Melt-Blending of PET/mmt Nanocomposites

Twin-screw extrusion of the nanocomposites took place at BAYER MaterialScience on a Prism TSE 16TC extruder with an L/D ratio of 16, run at 280 °C with a screw speed of 280 to 330 RPM. The PET and mmt were dried at 100 °C overnight under vacuum prior to pre-extrusion mixing which consisted of mechanized tumbling of the PET pellets and powder for 20 minutes. Prior to injection molding, the pelletized extrudate was dried again under vacuum overnight at 100 °C. Injection molding of micro-tensile and flexural bars took place on a BOY 22D hydraulic injection molding press operated with a barrel temperature of 295 °C with the mold at ambient conditions (see **Appendix 3.6.2** for the full melt-processing data sheet). Unless otherwise noted, all nanocomposites contain 3 wt. % mmt. All samples utilized a stabilizing agent in this study.

3.3.3 Dispersion Analysis

The dispersion of the mmt within the PET matrix was first analyzed via XRD of the micro-flexural bars on a Rigaku powder diffractometer, with a Cu K_α source ($\lambda = 1.5418$ Å), and a generator tension of 50 kV at 20 mA. The scanning occurred from 1.5° to 10° on the 2θ scale at a continuous scan rate of 0.6 degrees/minute. The d-spacing of the mmt layers was determined by Bragg's law.

Complementary TEM imaging of the injection molded bars was carried out, in order to allow for definitive conclusions on the dispersive characteristics of the nanocomposites. Thin sections (70 to 100nm) of the PET/mmt nanocomposites were

obtained with an ultramicrotome equipped with a diamond knife (Leica Ultracut UCT) and were transferred to carbon-coated copper grids (200-mesh). Bright field images were obtained with a JEOL 1200 EXII microscope equipped with a Tietz F224 digital camera. The images were obtained at an accelerating voltage of 80 kV and no heavy metal staining was required, as the contrast between the polymer and mmt was sufficient in providing proper contrast for successful imaging.

3.3.4   Mechanical Properties

The tensile properties of the bulk PET and its nanocomposites were measured by tensile testing on the injection molded micro-tensile bars. The tensile bars (dogbones) are ASTM D638 standard type IV specimen with a molded thickness of approximately 3.18 mm. The tensile tester, an Instron 5866 tensile tester, was operated with a crosshead speed of 50.8 mm/min. The Young's modulus (E), yield strength, and elongation-at-break will be reported as per the calculations from stress-strain curves done with the Instron software. The elongation at break is reported from the crosshead travel, as a strain extensometer with sufficient travel was unavailable. It is also important to note the tensile behaviors were measured on the as-molded tensile bars with no post-molding annealing.

Dynamic mechanical analysis (DMA) was utilized to examine the thermomechanical behaviors. A TA Instruments Q800 Dynamic Mechanical Analyzer with a 35 mm dual cantilever setup was utilized. Such tests probe the storage modulus (G'), a measure of the energy that is stored during deformation, the loss modulus (G"), a measure of the energy lost during deformation, and tan δ=G"/G', an indicator of the

material's ability to dissipate energy. The tan δ peak is also a good indicator of the (apparent) glass transition temperature (T_g). The program for testing was a standard constant frequency (1 Hz), constant strain (0.01 %) setup, coupled with a temperature sweep from 25 °C to 170 °C at a ramping rate of 4 °C/minute.

3.3.5 Crystallization Behaviors

The non-isothermal crystallization behaviors were examined using a TA Instruments Q100 DSC calibrated with sapphire and indium standards run under helium purge with a secondary nitrogen purge. The PET crystallinity was calculated by **Equation 3.1** where ΔH_m is the enthalpy of fusion and ΔH_m° is the enthalpy of fusion of the perfect crystalline PET (125.5 J/g).[**14**] For all scans shown here, the crystalline fractions reported have been normalized by the mass of the PET, rather than the mass of the specimen as usual. The non-isothermal crystallization behaviors were measured on as-molded and annealed, injection molded specimens. The annealed specimens were held for 1.5 hours at 140 °C to drive the crystallization process to near completion.

Equation **3.1**

$$\chi_c = \frac{\Delta H_m}{\Delta H_m^o} \times 100 \qquad\qquad (\text{Equation } \mathbf{3.1})$$

Optical microscopy under cross polarizers (PLOM) was employed to examine the spherulite shape and size of bulk PET and its nanocomposites on an Olympus BX-41 microscope (Hitech Instruments) equipped with a SPOT Insight QE camera. The microscope was also fit with a Linkam LTS 350 hot stage, controlled using LinkSys

software and cooled via liquid nitrogen, such that isothermal crystallization at elevated temperatures could be monitored. The samples were held isothermally above the melt temperature, at 280 °C for three minutes, to allow for complete melting of the crystalline material to occur. Subsequent crystallization took place isothermally at 237 °C, upon cooling fast (25 °C/minute) from the quiescent melt. Isothermal crystallization was allowed to proceed for 30 minutes during which a series of sequential images were taken, with one minute in between each image, to monitor the crystallization process. It is also important to note that no glass cover slips were used in this work as it has been found to alter polymer crystal growth behaviors.[15]

3.3.6   Thermal Analysis

The thermal degradation behaviors were measured via thermogravimetric analysis (TGA) on a TA instruments SDT Q600. All samples were run in an oxidizing (air) atmosphere with a flow rate of 100 mL/min run from ambient conditions to 1000 °C at a ramp rate of 10 °C/min. The temperature commonly referred to as the onset of degradation, the 5 % wt. loss ($T_{0.05}$) temperature, and the temperature at maximum mass loss rate ($T_{max\ MLR}$), are reported.

3.4   Results and Discussion

3.4.1   Montmorillonite Dispersion

The initial examination upon melt-blending should always be an assessment of the nanocomposite morphology to determine if the thermodynamics of dispersion are indeed satisfied. The XRD trace (see **Figure 3.1**) provides clear evidence that an intercalated morphology is developed for the PET/C25A mmt nanocomposite. The characteristic d_{001} shift to lower 2θ values from the d_{001} of pure organo-mmt signifies the gallery intercalation of the host polymer matrix during melt-blending, such that the d-spacing increases from 1.8 to 3.1 nm as determined by Bragg's law (as determined from the 2θ of the peak of the diffracted intensity).

Figure **3.1**
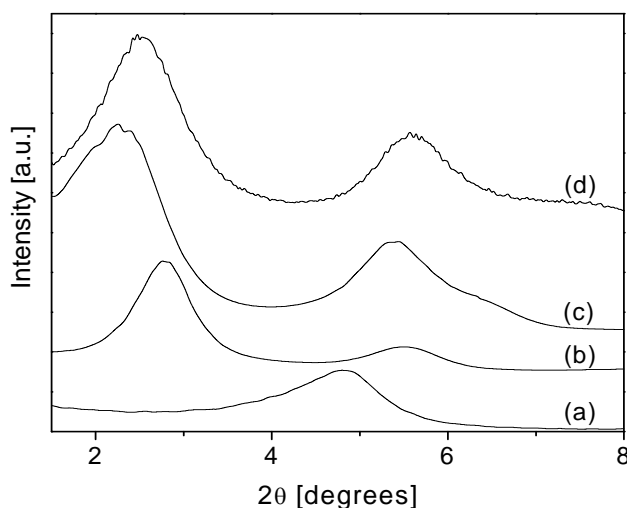
Figure **3.1**: XRD patterns of the organically modified mmt and the corresponding melt-blended PET/mmt nanocomposites: (a) C25A mmt, (b) PET/C25A nanocomposite, (c) imm-mmt and (d) PET/imm-mmt nanocomposite.

The pure imm-mmt gallery is more expanded than the alkyl-ammonium modified C25A mmt, an effect attributed to conformational differences of the different surfactant chemistry.[16] Melt-blending of the PET with the imm-mmt led to a slight reduction from around 3.7 to 3.5 nm in the d_{001}-spacing, which in general is appropriate for an intercalated PET/organo-mmt morphology, but due to the high initial d_{001}-spacing of the organo-mmt TEM is necessary to confirm what is expected to be an intercalated morphology.

Dispersion analysis via TEM (see **Figure 3.2 and 3.3**) confirms the presence of an intercalated morphology for both surfactant chemistries. Analysis of the low magnification images shows the overall dispersion to be –in both instances– rather good, with small, well-dispersed tactoids present throughout the polymer, and with absence of large tactoids/agglomerations. The high magnification images further illustrate the polymer intercalated structure, as we are capable of observing individual layers of the tactoid which maintained their excellent parallel registry as they are expanded from the polymer penetration. These images in general could be considered to be characteristic examples of a well-dispersed intercalated morphology.

Figure **3.2**
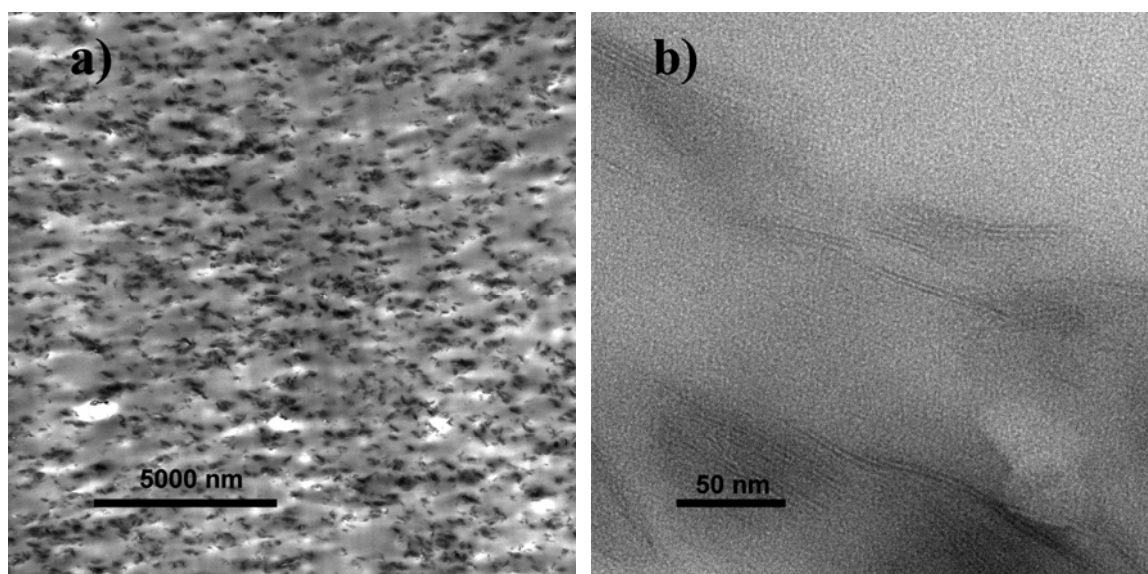
Figure **3.2**: Low (a) and high (b) magnification TEM images of PET/3% mmt C25A nanocomposites indicating a well-dispersed intercalated morphology.

Figure **3.3**
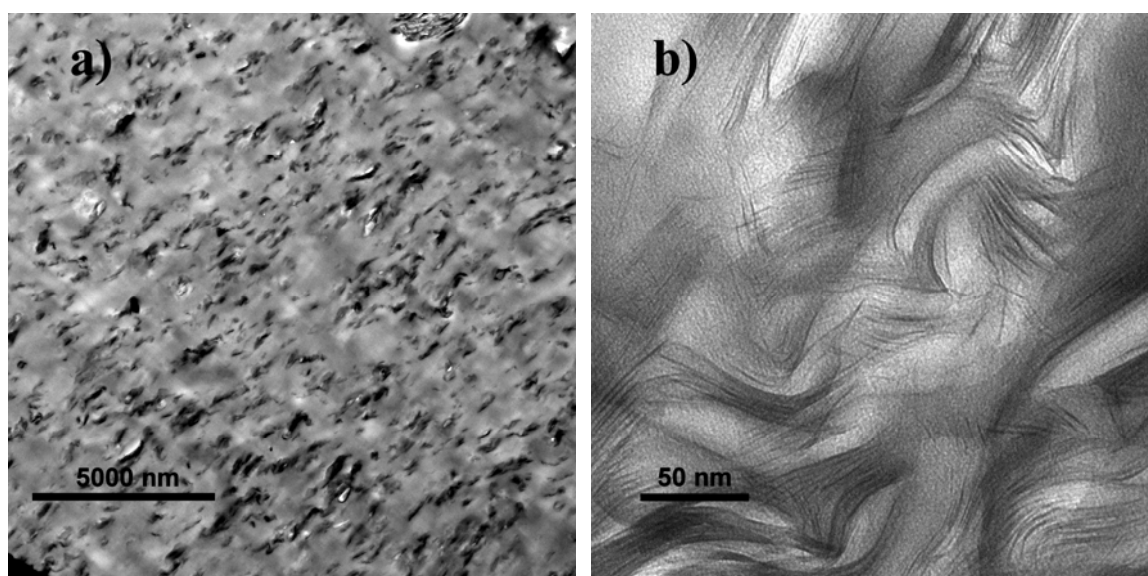
Figure **3.3**: Low (a) and high (b) magnification TEM images of PET/3% mmt imm-mmt nanocomposites indicating a well-dispersed intercalated morphology.

3.4.2 Crystallization Behaviors

The crystallization behavior of PET and its nanocomposites were first examined via non-isothermal DSC analysis (**Figure 3.4**). The as-molded specimens, the samples examined after melt-blending without further annealing, indicated that only relatively low degrees of crystallization were developed during the melt-blending process, as we observe a strong cold crystallization peak (T_{cc}) (**Figure 3.4a**). This is not surprising when considering the low mold temperature (25 °C) during injection molding. Thus, we are essentially quenching from the melt.

Previous discussion has centered on the strong nucleating effect of layered silicates in crystallizable polymer matrices. We first observe this nucleating effect in the as-molded nanocomposites, where the degree of crystallinity rises from 9 % in the unfilled PET to above 14 % in the corresponding nanocomposites molded under identical melt-blending conditions (**Figure 3.4c**). The overall crystallization rate in the nanocomposites increases compared to the bulk, as is common in some crystallizable polymer/layered silicate nanocomposites.[17][18]

Post-processing annealing of the specimens at 140 °C for 1.5 hours was sufficient in driving the crystallization process to near completion and, as DSC analysis indicates, the cold crystallization peak disappears after the annealing process (**Figure 3.4b**).

Figure **3.4**
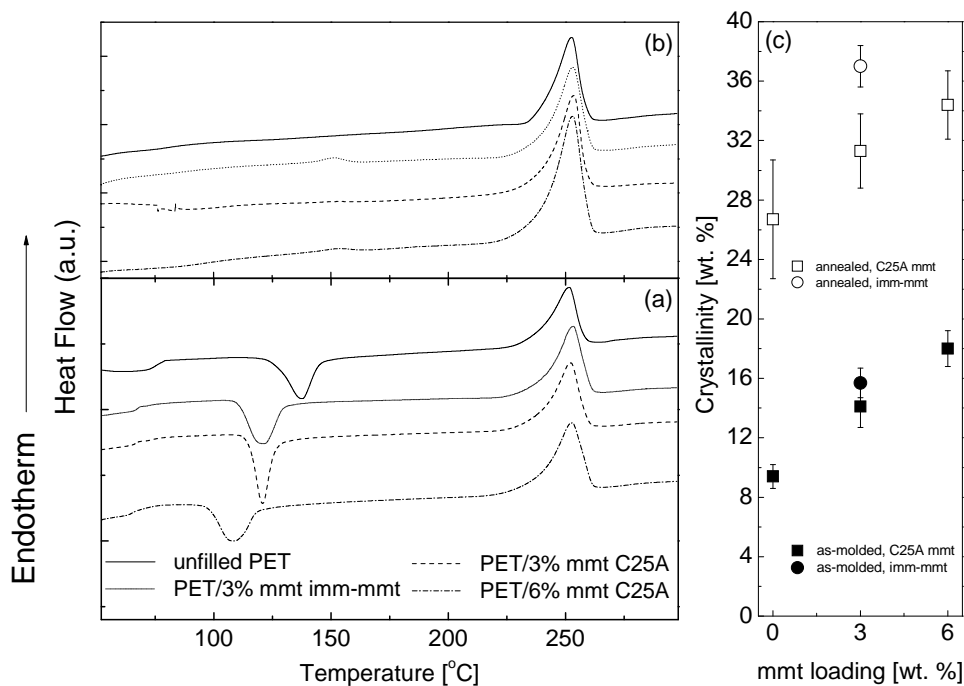
Figure **3.4**: DSC scans of PET and its nanocomposites: (a) as-prepared, (b) annealed at 140 °C for 1.5 hours, and (c) the as-molded and annealed crystallinity PET: as-prepared samples (filled symbols), annealed samples (open symbols); imm-mmt filled (circles), C25A mmt filled (squares).

The increase in the degree of crystallinity is attributed to the rise in the nucleation density upon nanocomposite formation [**18**]; such enhancements in the overall degree of crystallinity have been observed previously in PET/mmt nanocomposites.[**12**] At the same time, previous comprehensive studies in this laboratory have found copolymer PET to undergo a strong heterogeneous nucleation crystallization with no marked changes in the crystalline fraction, albeit a reduction in the linear crystal growth rate upon incorporation of montmorillonite filler. The modeling of such crystallization kinetics prior to spherulite impingement is well described by **Equation 3.2** where V_f^c is the total

crystallinity, ρ_n is the nuclei density, G_R is the linear crystal growth rate, and t is the crystallization time. When $V_f^{\,c}$ is 50 %, the crystallization time t is defined as the half time of crystallization ($t_{1/2}$), and corresponds to the time necessary to reach 50 % of the total enthalpy of crystallization under isothermal crystallization conditions.

Equation **3.2**

$$V_f^c = \frac{4}{3}\pi \; \rho_n \; G_R^3 \; t^3 \qquad\qquad \text{(Equation **3.2**)}$$

The nucleation density increases in the PET nanocomposites since the layered silicates act as efficient nucleating agents, as confirmed when examining the spherulitic structure of PET and its nanocomposites via PLOM. An induction time of one minute during isothermal crystallization at 237 °C was observed for bulk PET (see **Figure 3.5**). During spherulitic growth, initial impingement occurs after about four minutes of isothermal crystallization, with complete impingement taking place shortly thereafter; the final PLOM image was taken after 30 minutes of isothermal crystallization with fully impinged crystals being present. The spherulite size of the PET was determined to be 24 ± 2 micrometers.

The quaternary ammonium modified C25A mmt based PET nanocomposites (see **Figure 3.6**) appear to display rod-like crystal growth at the outset (similar to some PET nanocomposites reported in literature).[**13**] Ultimately, spherulitic growth does appear to occur with slight deviations from the more classic spherulites of the bulk, with the size being 16 ± 2 micrometers just prior to impingement. The induction time in the PET/C25A nanocomposite increased over what was observed in the bulk PET upon the addition of mmt (first nuclei observed after about 5 minutes of isothermal crystallization).

Figure **3.5**
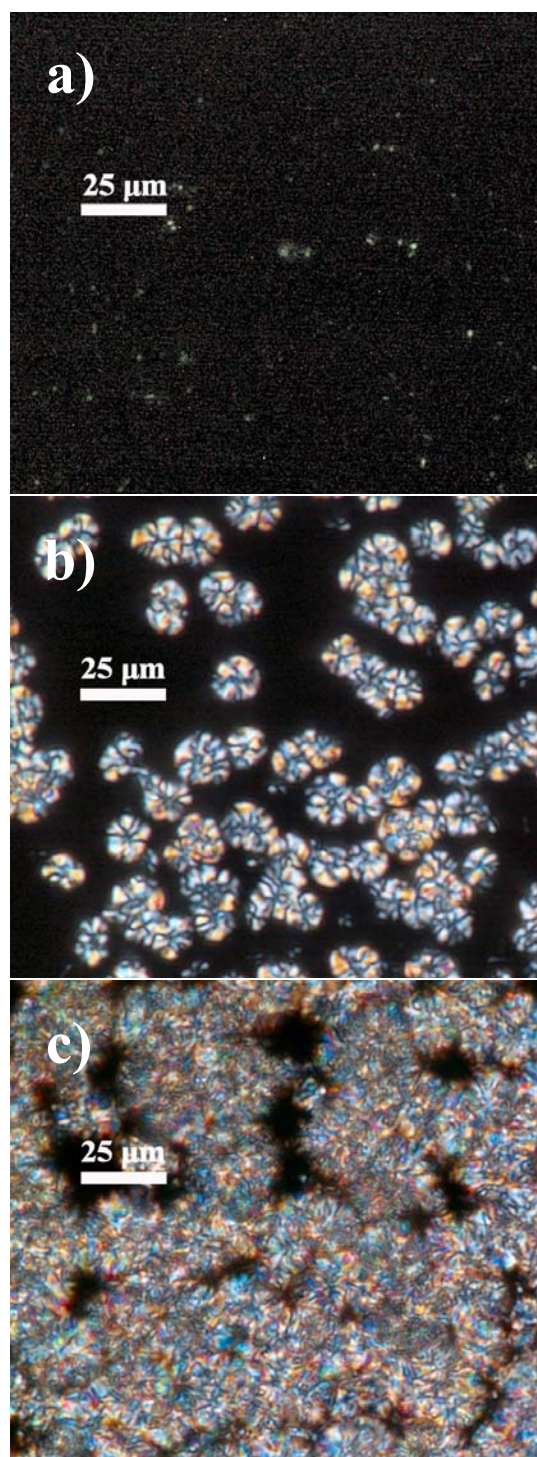
Figure **3.5**: PLOM of isothermal PET crystallization at 237 °C: a) initial nuclei form at 1 minute, b) rapid spherulite growth at 3 minutes, c) full impingement at 30 minutes.

Figure **3.6**
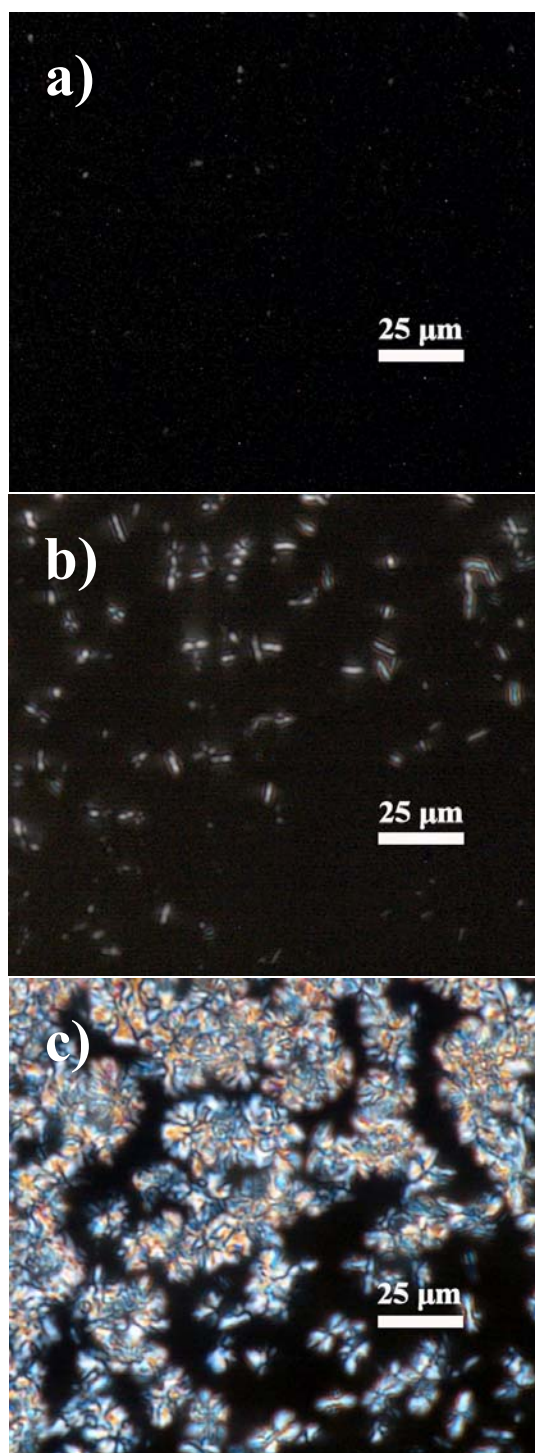
Figure **3.6**: PLOM of isothermal PET/3% mmt C25A crystallization at 237 °C: a) nucleation at 5 minutes, b) irregular growth at 8 minutes, and c) impinged at 30 minutes.

Figure **3.7**
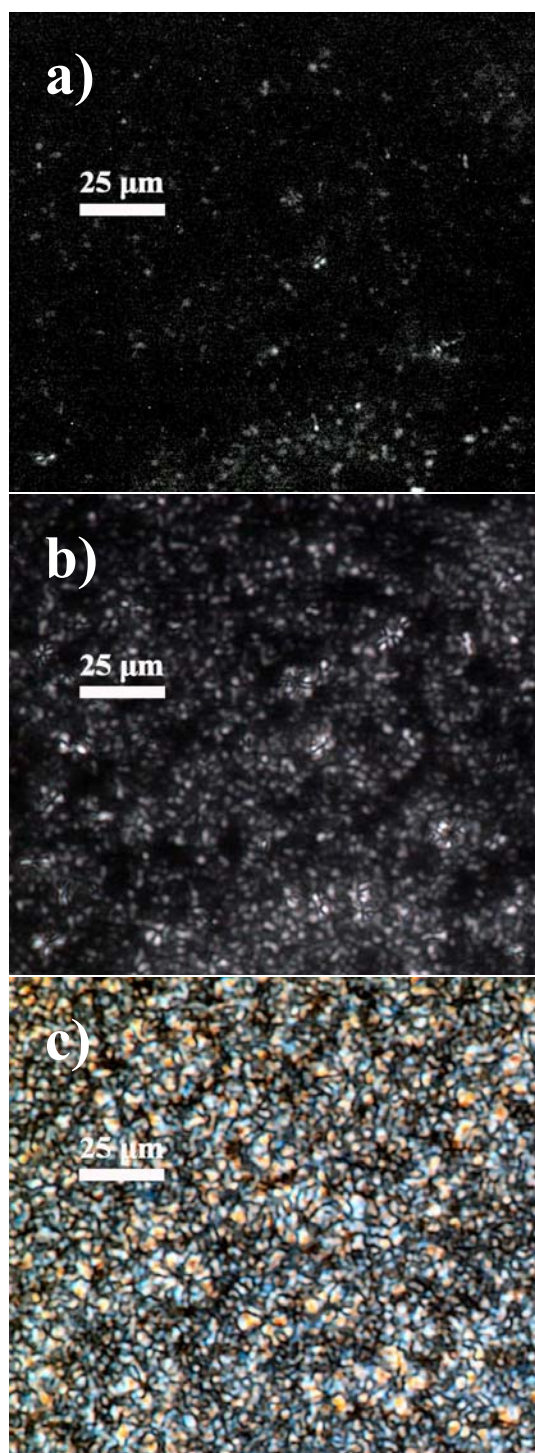
Figure **3.7**: PLOM of isothermal PET/3% mmt imm-mmt crystallization at 237 °C: a) nucleation at 3 minutes, b) growth at 6 minutes, and c) fully impinged at 30 minutes.

The imm-mmt based PET nanocomposite developed dramatically smaller spherulites than the C25A mmt nanocomposites (see **Figure 3.7**). The induction time was slightly less than the C25A mmt nanocomposites with initial nuclei forming at around 3 minutes and initial impingement occurred shortly thereafter. The quaternary ammonium modified C25A mmt has spherulites that were greater in size than those formed in the co-PET/imm-mmt nanocomposites; however, the PET/imm-mmt spherulites were in the sub-micrometer scale, and were markedly smaller than those of the co-PET/imm-mmt nanocomposites. Again, this further confirms the nucleation density rise upon mmt addition, which is expectedly more pronounced for better dispersed nanofillers; *cf.* the quantitative differences between the imm-mmt and C25A-mmt.

Thus, from a crystallization standpoint, we may definitively conclude that the mmt platelets act as effective nucleating agents to spur heterogeneous nucleation with a substantial rise in the nucleation density. Likewise, we observe a corresponding decline in spherulite size that corresponds with the nucleation density rise.

3.4.3 Mechanical Properties

Stiff matrix polymers, such as PET, are not expected to realize enhancements in the tensile modulus on the order of those observed in such 'soft-matrix' polymers like polyethylene or polydimethylsiloxane, where relative enhancements in excess of 300 % are typically observed even at low filler loading levels.[**18**] The moduli of the

homopolymer PET/mmt nanocomposites has a 20 % relative improvement at 3 % mmt

(see **Table 3.1**) and a 34 % improvement in the PET/6 % mmt C25A system.

Table **3.1**

Table **3.1**: Tensile properties of PET/mmt nanocomposites as measured by Instron.

mmt content [wt. %]	Tensile Modulus [MPa]	Relative Modulus Improvement [%]	Yield Strength [MPa]	Elongation at break [%]
C25A mmt				
Neat	1550 (± 50)	-	55 (± 2)	230 (± 15)
3	1860 (± 25)	20	60 (± 1)	115 (± 15)
6	2080 (± 75)	34	55 (± 2)	3 (± 0)
imm-mmt				
Neat	1550 (± 50)	-	55 (± 2)	230 (± 15)
3	1830 (± 25)	19	59 (± 1)	202 (± 35)

The ductility (elongation-at-break) characteristics of the PET/imm-mmt

nanocomposite are rather remarkable, when compared to the bulk and especially to the

C25-mmt nanocomposite. We find only a slight reduction in elongation at break from 230

% to 200 % at 3 wt. % mmt imm-mmt. The C25A mmt based nanocomposites display the

typical embrittlement observed in most polymer (nano)composites, especially when the

loading level is above the percolation threshold (the point at which a continuous network

is created from the filler-filler contacts) at about 6 % mmt, also indicated by the

elongation-at-break drop from 230 % in the unfilled PET to just 3 % in the filler-

percolated nanocomposite.

Spherulite size has been correlated to the ductile/brittle behaviors with respect to

the impact resistance of polymer matrices.[**19**] Conflicting opinions are present in the

literature with respect to the role of spherulite size on the ductility observed in

mechanical testing, specifically the elongation at break for tensile experiments. Reports indicating a strong correlation between spherulite size and tensile elongation at break [19][20], are weakened by the fact that comparisons were made while not all variables are held constant. At the same time, more convincing arguments have been made –albeit with respect to fracture toughness and fatigue crack propagation rather than tensile response– that show spherulite size not to be correlated to ductile/brittle failure.[21] In addition, the presence of tie-chains –inter-crystalline macromolecular links between/within polymer spherulites– have been shown to alter the mechanical behaviors of a polymer.[22][23] Since the incorporation of a nucleating agent increases the number of crystallization sites, it can also potentially increase the number of tie-chains.[23] The nanocomposites in this study were observed to undergo an increase in the nucleation density upon nanocomposite formation, with the PET/imm-mmt nanocomposites developing smaller spherulites and a greater increase in the nucleation density than the PET/C25A mmt nanocomposites. Thus, we believe the nucleation density rise and the suspected likelihood of a greater number of tie-chains between the smaller spherulites led to the more ductile tensile behaviors observed. However, the specific mechanism remains ambiguous.

The thermo-mechanical properties of PET and its nanocomposites were also measured via DMA (see **Figure 3.8**). We observe similar enhancements in the storage modulus at room temperature as were observed in the tensile modulus. The relative G' of the PET/C25A nanocomposite ($G'_{Nanocomposite}/G'_{Neat}$) is 1.29 and the relative G' of the imm-mmt based PET nanocomposite is 1.25, indicating the modulus may not be rate dependent and it persists for higher-than-ambient temperatures.

Figure **3.8**
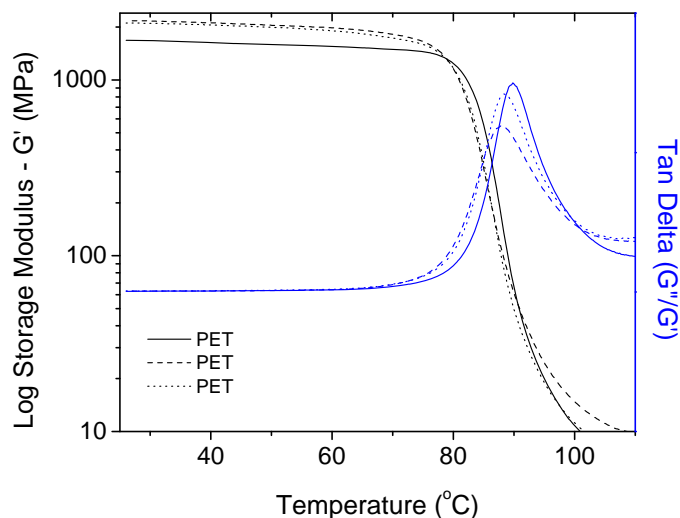
Figure **3.8**: DMA tests measuring the thermomechanical properties of PET and its nanocomposites.

3.4.4 Thermal Stability

The TGA results of PET and its nanocomposites in an oxidizing environment are shown in **Table 3.2**. The results under the inert atmosphere (nitrogen) indicated no distinct differences between the bulk and corresponding nanocomposites. We find the introduction of the layered silicate improves the onset of decomposition, probably due to the well-known barrier effect of the high-aspect ratio mmt filler [**23**], given the results from the inert atmosphere. The results shown here are similar to the co-PET/mmt nanocomposites, when examined under an oxidizing atmosphere.

Table **3.2**

Table **3.2**: Thermal stability (TGA) of PET and its nanocomposites in an oxidizing environment.

Sample	in Air	
	$T_{0.05}$	$T_{max\ MLR}$
	^{o}C	^{o}C
Neat PET	356	438
PET/C25A mmt	379	438
PET/imm-mmt	385	441

3.5 Conclusions

The crystallization behaviors, mechanical properties, and thermal stability of well-dispersed intercalated PET/mmt nanocomposites were investigated, and two organic modifications for the mmt nanofillers were contrasted. The addition of the inorganic layered silicate led to an increase in the nucleation density and a corresponding decrease in the spherulite size as was confirmed by PLOM.

The tensile moduli of the PET/mmt nanocomposites were improved compared to the unfilled PET, with a 20 % improvement in the relative modulus at 3 wt. % inorganic mmt. The thermally stable alkyl-imidazolium surfactant chemistry led to a more ductile nanocomposite; the elongation at break is nearly double the value observed in the conventional alkyl-ammonium modified mmt. This is believed to be a function of the increased nucleation density and suspected corresponding increase in inter-crystalline linkages (*cf.* tie chains). Once the percolation threshold is exceeded for the nanofillers, as is the case in the 6 wt. % mmt PET/C25A nanocomposite, the embrittlement of the

nanocomposite becomes very strong. The "barrier effect" of the layered silicate was pronounced in thermal degradation of the PET/mmt nanocomposites, as measured by TGA, with a substantial increase in the onset of degradation under air (*ca.* 30 °C increase in the 5 % weight loss temperature, $T_{0.05}$) for the imm-mmt based nanocomposite.

In general, when comparing the homopolymer PET/mmt nanocomposites to the copolymer PET/mmt nanocomposites, the qualitative behaviors are similar. The overall influence of mmt on the crystallization and the improvements in mechanical properties are highly similar. The non-crystallizable co-monomer influences the crystallization behaviors on its own, and the mmt induced effects seem independent of the PET structure or surfactant chemistry.

3.1 Appendix

This appendix includes the pertinent structures of the polymers and surfactants utilized, as well as the injection molding parameters used for the work in this chapter.

3.1.1 Pertinent Chemical Structures

Figure **3.9**
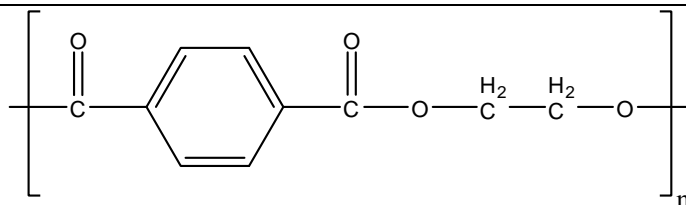
Figure **3.9**: Poly(ethylene terephthalate) repeat unit structure.

Figure **3.10**
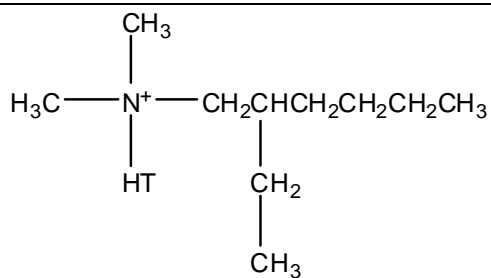
Figure **3.10**: Cloisite 25A surfactant structure with HT referring to hydrogenated tallow which is 65% $C_{18}H_{37}$, 30% $C_{16}H_{33}$, and 5% $C_{14}H_{29}$.

Figure **3.11**
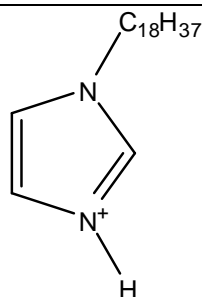
Figure **3.11**: Lab synthesized alkyl-imidazole surfactant for the imm-mmt.

3.1.2 Injection Molding Parameters

Figure **3.12**

Figure **3.12**: Injection molding processing data sheet for PET/mmt nanocomposites.

References

1. Alexandre, M. and Dubois, P., *Materials Science and Engineering* 2000; R28:1–63.

2. Ray, S.S. and Okamoto, M., *Progress in Polymer Science* 2003; 28:1539–1641.

3. Giannelis, E.P., Krishnamoorti, R., and Manias, E., *Advances in Polymer Science.* 1998; 138:107–148.

4. Fakirov, S., **Handbook of Thermoplastic Polyesters**, John Wiley & Sons, UK 2002.

5. Xie, W., Gao, Z., Pan, W-P., Hunter, D., Singh, A., and Vaia, R., *Chemistry of Materials* 2001**;** 13:2979–2990.

6. Yoon, P.J., Hunter, D.L., and Paul, D.R., *Polymer* 2003; 44:5341–5354.

7. Davis, C.H., Mathias, L.J., Gilman, J.W., Schiraldi, D.A., Shields, J.R., Trulove, P., Sutto, T.E., and DeLong, H.C., *Journal of Polymer Science: Part B: Polymer Physics* 2002; 40:2661–2666.

8. Gilman, J.W., Awad, W.H., Davis, R.D., Shields, J., Harris, R.H., Davis, C., Morgan, A.B., Sutto, T.E., Callahan, J., Trulove, P.C., and DeLong, H.C., *Chemistry of Materials* 2002; 14:3776–3785.

9. Wang, Z.M., Chung, T.C., Gilman, J.W., and Manias, E., *Journal of Polymer Science: Part B: Polymer Physics* 2003; 41:3173–3187.

10. Ke, Y., Long, C., and Qi, Z., *Journal of Applied Polymer Science* 1999; 71:1139–1146.

11. Ke, Y-C., Yang, Z-B., Zhu, C-F., *Journal of Applied Polymer Science* 2002; 85:2677–2691.

12. Ou, C.F., Ho, M.T., and Lin, J.R., *Journal of Polymer Research* 2003; 10:127–132.

13. Wan, T., Chen, L., Chua, Y.C., and Lu, X., *Journal of Applied Polymer Science* 2004; 94:1381–1388.

14. Wunderlich, B., **Macromolecular Physics, Vol. 1, Crystal Structure, Morphology, Defects**, Academic Press, New York (1973).

15. Schultz, J.M. **Polymer Crystallization**. Oxford University Press, New York 2001.

16. Lagaly, G. and Dekany, I., *Advances in Colloid and Interface Science* 2005; 114:189–204.

17. Liang, G., Xu, J., and Xu, W., *Journal of Applied Polymer Science* 2004; 91:3054–3059.

18. Manias, E., Polizos, G., Nakajima, H., and Heidecker, M.J., **Flammability of Polymer Nanocomposites.** Editors: Wilkie and Morgan, Wiley & Sons, NJ, 2007.

19. Perkins, W.G., *Polymer Engineering and Science* 1999; 39:2445–2460.

20. Way, J.L., Atkinson, J.R., and Nutting, J., *Journal of Materials Science* 1974; 9:293–299.

21. Yeh, J.T. and Runt, J., *Journal of Polymer Science: Part B: Polymer Physics* 1991; 29:371–388.

22. Phillips, P.J., and Edwards, B.C., *Polymer Letters Edition* 1976; 14:449–454.

23. Zhang, X., Xie, F., Pen, Z., Zhang, Y., Zhang, Y., and Zhou, W., *European Polymer Journal* 2002; 38:1–6.

Chapter 4

Melt-Blended Polycarbonate/Montmorillonite Nanocomposites

4.1   Summary

Alternative surfactant treatments were investigated to determine their applicability for Polycarbonate/montmorillonite nanocomposites. The subsequent degradation behaviors and the enhancements in the mechanical behaviors of the nanocomposites were analyzed. It was determined that conventional quaternary ammonium surfactant chemistries provide a better overall mix of properties as compared to the more thermally stable alkyl-imidazole and alkyl-phosphonium surfactant chemistries as, in certain instances, the thermally stable surfactants catalyzed PC matrix degradation. Additionally the degree of platelet alignment was varied by adjusting the amount of shear generated during the injection molding process in order to ascertain its effect on the mechanical properties of the nanocomposite. Although the alignment of the nano-scale filler was effectively altered, no significant improvement in the mechanical behaviors of the aligned nanocomposites was observed.

4.2   Introduction

Recent success in improving polymer performance through the addition of small loadings (≤ 5 wt. %) of nano-fillers such as layered silicates to form polymer/layered-

silicate nanocomposites have shown drastic improvements in the mechanical, thermal, barrier, and flammability characteristics.[1][2][3] The potential for matrix enhancement in high-performance polymers such as PC is of particular interest for a wide-variety of industrial applications, however the applicability of Polycarbonate (PC)/montmorillonite (mmt) nanocomposites is considered to be challenging. PC is known to break down by hydrolysis (see **Figure 4.1**).[4][5][6]

Figure **4.1**
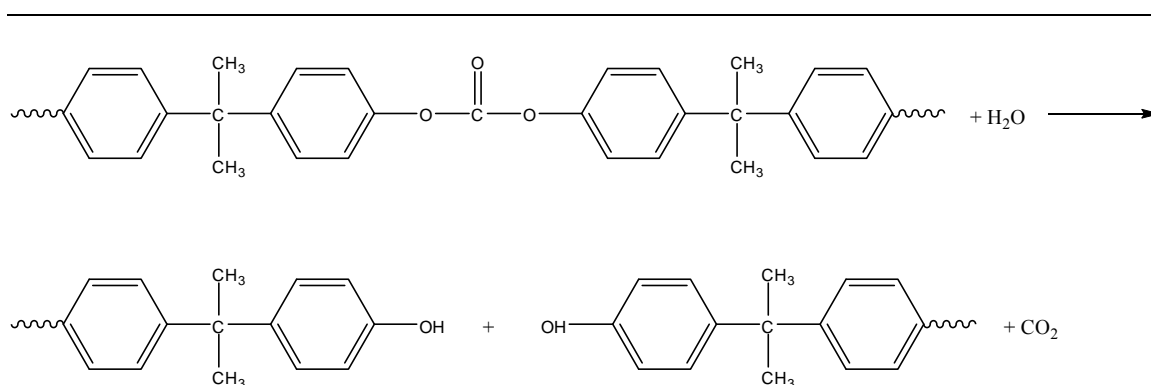
Figure **4.1**: Hydrolytic degradation of bisphenol-A PC with the formation of phenolic end groups at the carbonate linkage.[4][5]

This hydrolysis of PC has been found to be acid and base catalyzed.[4][7] Considering that the alkyl-ammonium surfactants, typically used to promote polymer/mmt miscibility, have degradation temperatures [8] below that of the melt-processing temperature of PC (280 to 290 °C), additional matrix degradation from amine catalyzed hydrolysis is expected to occur. Literature studies have found degradation does occur during the melt-blending process of PC/mmt nanocomposites and leads to severe color formation and molecular weight reduction, although mechanical properties appear to be influenced little by such degradation.[9][10][11] However, the impetus remains

strong to produce thermally stable melt-processable PC/organo-mmt nanocomposites using high thermal stability surfactants.

For high melt-blending temperature systems such as poly(ethylene terephthalate) (PET) [12] and syndiotactic Polystyrene [13], thermally stable alkyl-imidazolium surfactants have been used to enable melt-processing of their nanocomposites. Alkyl-imidazolium modified mmt has an onset of thermal degradation (5 % wt. loss) greater than 300 °C under inert conditions and about 280 °C in an oxidizing environment (under air).[13] The applicability of alternative surfactant chemistries such as phosphonium based surfactants as surface treatments for mmt has also been examined in the literature.[14] Phosphonium modified mmt's have been observed to maintain maximum degradation between 300 to 400 °C under inert conditions with broad onset temperatures indicating the potential for use in high thermal stability polymers. Surfactant chemistries similar to alkyl-imidazole and quaternary phosphonium may offer the potential to generate a stable PC/mmt nanocomposite with minimal degradation upon melt-blending.

The interest in PC/mmt nanocomposites from an industrial standpoint is rooted in their potential applicability to structural applications in which the retention of the inherent optical clarity of PC is not a concern. With this known, the mechanical properties of such systems become of utmost importance. Polymer/layered silicate nanocomposites typically require loading levels of less than 5 wt. % to impart the mechanical properties associated with conventional composites loadings of 30 to 60 wt. %. Conventional composites develop severe embrittlement at such high loading levels whereas the penalty for nano-scale filler addition is less severe when the loading level is held below the approximate percolation limit of about 5 wt. % mmt.

The detailed discussion from **Chapter 2** regarding the origins of mechanical properties enhancements in polymer/mmt nanocomposites explains that the enhancement is rooted in the ability to effectively disperse high-aspect ratio filler (aspect ratio of 10 to 1000, surface area of about 700 m^2/g) with a modulus on the order of 2 TPa.[15] Two factors have been found to limit the efficiency of mmt as a reinforcing agent: (1) a lack of complete exfoliation and (2) a deviation of the platelet orientation away from perfect biaxial in plane alignment.[16] Such findings have led to attempts to preferentially align the mmt platelets and other high-aspect ratio fillers such as carbon nanotubes.[17][18][19] A prime example of such systems would be triaxially oriented epoxy/mmt nanocomposites that have been developed by uniaxial electric fields.[20] The end goal here is to control filler dispersion, through alignment of the mmt, such that 'functional' nanocomposites are developed with superior mechanical properties.

Thus, the goals of this work are to: (1) ascertain the thermal stability of PC/mmt nanocomposite systems in which surfactant induced matrix degradation is evaluated, and (2) estimate any filler alignment effects on the mechanical (tensile) properties for this high stiffness matrix. In this work we employ ammonium, imidazolium, and quaternary phosphonium based surfactant treatments as surface modifications for montmorillonite. The stability of such melt-blended PC/organo-mmt nanocomposites is closely monitored. We also vary the degree of alignment of the mmt platelets during the injection molding process to enhance the mechanical properties of a specific PC/organo-mmt system.

4.3   Experimental

4.3.1   Materials

The PC used in these studies was a standard medium-molecular weight resin that was provided by BAYER MaterialScience (Grade 2608, M_w = 51 kg mol^{-1} determined by THF gel permeation chromatography (GPC) that was calibrated with polystyrene standards). Quaternary-ammonium modified montmorillonites were donated by Southern Clay Products: (1) Cloisite 25A (C25A) which is modified by dimethyl, hydrogenated tallow, 2-ethlyhexyl quaternary ammonium surfactant, (2) Cloisite 30B (C30B) which is modified by methyl, tallow, bis-2-hydroxyethyl, quaternary ammonium surfactant and by Nanocor: (1) Nanomer I42E (I42E) which is modified by dimethyl, ditallow, quaternary ammonium surfactant. All commercially supplied mmt and organo-mmt was used as received. Na$^+$ montmorillonite (PGW) with a cation exchange capacity (CEC) of ca. 1.4 meq/g was obtained from Nanocor.

Synthesis of the thermally stable alkyl-imidazole surfactant and the corresponding ion-exchange process was completed according to the procedure outlined in **Chapter 3**. The PGW was also exchanged with the high thermal stability quaternary phosphonium based surfactants purchased as salts and used as received from TCI America: (1) n-hexadecyl tri-n-butyl phosphonium bromide (P-3C$_4$C$_{12}$) with a molecular weight of 507.7 g/mol, (2) n-dodecyl triphenylphosphonium bromide (P-3PhC$_{12}$) with a molecular weight of 511.5 g/mol, and (3) tetra-N-octylphosphonium bromide (P-4C$_8$) with a molecular weight of 563.8 g/mol to prepare the phosphonium exchanged organo-mmt. See **Appendix 4.6.1** for the structure of the PC and the pertinent surfactant chemistries.

The cation exchange reaction for the quaternary phosphonium surfactants with Na$^+$ mmt (PGW) were identical to one another with several batches of organo-mmt produced for each surfactant under equivalent conditions. PGW (20 g) was dispersed in 1000 mL of distilled water in 2000 mL beaker at 50 °C with vigorous mechanical stirring for one hour. The surfactant (a 50 % excess – 42 meq) was dispersed in 1000 mL of ethanol at 50 °C with mechanical stirring also for one hour. Since the surfactants were purchased already protonated, the protonation step is unnecessary. The ion-exchange reaction was initiated by quickly adding the surfactant solution to the Na$^+$ mmt suspension while maintaining vigorous stirring at 50 °C with immediate flocculation occurring. The reaction was allowed to continue for 12 hours, with collection of the exchanged organo-mmt by filtration. The organo-mmt was then washed for 2 hours with 1000 mL of hot (50 °C) ethanol under constant stirring and filtered a total of three times to remove excess unbound surfactant. The organo-mmt was vacuum dried at 80 °C for 12 hours to remove all remaining solvent prior to thermogravimetric analysis.

4.3.2   Thermal Degradation Analysis

The thermal degradation of the organo-mmt and the corresponding nanocomposites were examined by thermogravimetric analysis (TGA) on a TA instruments SDT Q600 instrument. All samples were run under oxidizing (air) and inert (nitrogen) atmospheres with a purge gas flow rate of 100 mL/min from ambient conditions to 1000 °C at a ramp rate of 10 °C/min. The temperature at the onset of degradation, also known as the 5 % wt. loss temperature ($T_{0.05}$), and the temperature at

the maximum mass loss rate ($T_{max\ MLR}$) were evaluated from the weight loss and MLR vs. temperature curves.

4.3.3 Nanocomposite Preparation

The studies in this work are broken down into two categories: (1) thermally stable surfactant analysis and (2) optimization of PC/mmt mechanical properties through mmt platelet alignment.

The nanocomposites for the first series of the study, the surfactant degradation study, were extruded on a Haake counter-rotating twin screw extruder with an L/D ratio of 20, operated at 280 °C at a screw speed of 50 RPM. The extrudate was then hand pelletized prior to injection molding of micro-tensile and micro-flexural bars on a Boy 22D, 24 ton injection molding machine operated with a melt-temperature of 295 °C with the mold temperature at ambient conditions. Prior to extrusion all materials were dried at 100 °C overnight under vacuum and were tumbled for 20 minutes. The extrudate was again dried overnight at 100 °C prior to injection molding. The micro-tensile bars (dogbones) are ASTM D638 standard type IV specimens with a molded thickness (h) of about 3.2 mm. The micro-flexural bar profile was 65 mm in length, the width was 12.75 mm, and the thickness was 3.2 mm. No stabilizer for the PC/mmt nanocomposites was utilized in these samples.

Samples for the second series of experiments, the optimization of the mmt alignment and mechanical properties, were prepared via twin-screw extrusion on a Prism TSE 16TC extruder with an L/D ratio of 16, which was run at 280 to 330 RPM and

280 °C. All materials were dried at 100 °C overnight under vacuum and tumbled for 20 minutes prior to extrusion. Subsequent injection molding took place on a Cincinnati Milacron 110 ton injection-molding machine with two sets of samples being molded, one set with a mold temperature of 49 °C and the other at 80 °C, with the sample profile being a rectangular bar. The rectangular bar had a length of 155 mm, a width of 12.75 mm and the thickness was varied between 1 mm, 2 mm, and 3.2 mm. The injection velocity was maximized to develop the highest flow rate possible (set point was 115 cm^3/sec over 2 cavities). A similar nanocomposite (same PC and organo-mmt) was injection molded on the low shear rate Boy 22D press to compare the behaviors of two sample sets. The injection velocity on the Boy 22D was set such that the flow rate was 38 cm^3/sec (over 4 cavities).

Solution blending was also utilized to produce thin films for comparison with respect to the degree of alignment of the mmt platelets for PC/3 wt. % mmt nanocomposites. Dichloromethane (DCM) based solutions produced the best surface finish with excess solvent removal being possible upon simple vacuum drying. Dilute solutions (10 wt. % PC) were mechanically stirred at 60 °C for four hours followed by two hours of sonication at ambient conditions, followed by film deposition on flat glass plates with enclosed edges for four hours with vacuum drying overnight to remove the excess DCM. The average thickness of the films was 200 micrometers.

4.3.4 Dispersion Analysis

The dispersions developed in the nanocomposites for the first part of the study were examined via wide angle x-ray diffraction (XRD). The XRD was performed on the injection molded micro-flexural bars on a Rigaku powder diffractometer with a Cu K_α source ($\lambda = 1.5418$ Å); the generator tension was 50 kV run at 20 mA. The scanning from 1.5 ° to 10 ° on the 2θ scale was done at a continuous scan rate of 0.6 degrees/minute.

Additionally, dispersion and alignment characteristics were evaluated by a Bruker 2D X-Ray diffraction (XRD) at the Air Force Research Lab, on the Wright-Patterson Air Force Base, Dayton, OH. The source was a Cu K_α tube ($\lambda= 1.5418$ Å) with a generator tension of 50 kV, a current of 20 mA, and a sample to detector distance of 218.3 mm. The exposure time was 5 minutes for all samples. Silver behenate (Ag Beh) was used as a standard to calibrate 2θ prior to collecting data. Each specimen was probed in the three potential directions of orientation with the average sample thickness being about 0.85 mm.

Transmission electron microscopy (TEM) was used to complement the XRD to more effectively probe dispersion and alignment characteristics and to gain a visual, albeit local, representation of the degree of alignment. TEM images of the PC nanocomposites were obtained with a JEOL 1200 EXII instrument operated with an accelerating voltage of 80 kV, and equipped with a Tietz F224 digital camera. Ultra thin sections (70 to 100 nm) of the nanocomposites were obtained with an ultramicrotome (Leica Ultracut UCT) equipped with a diamond knife. The sections were transferred to carbon-coated copper grids (200-mesh) prior to imaging.

4.3.5 PC Matrix Degradation Analysis

Molecular weight degradation of the host PC matrix was examined via tetrahydrofuran (THF) based gel permeation chromatography (GPC) on all of the injection molded samples on polymer extracted from the nanocomposites after all processing was completed. Specifically, the PC was extracted from unfilled and filled injection molded bars by complete dissolution in GPC grade THF, followed by syringe filtration with a 0.2 micrometer filter (twice). The extracted polymer was precipitated and dried in vacuum at 60 °C. An injectable solution with a concentration of 1 mg of PC per mL of THF was then created with the precipitated PC and GPC-grade THF. The samples were analyzed on a Waters 1515 Isocratic HPLC pump with a Waters 2414 refractive index detector with two HR5E styragel columns and a guard column. The flow rate was 1 mL per minute and the temperature was 40 °C. Both extraction and filtering were done at conditions that would better evaluate the smaller-size PC fragments, i.e., if there is any systematic error introduced by this approach it would be towards underestimating PC molecular weight (overestimating extent of the degradation).

4.3.6 Mechanical Properties Analysis

The tensile properties of the bulk PET and its nanocomposites were measured by tensile testing on the injection molded ASTM type IV micro-tensile bars for the surfactant suitability analysis. The tensile tester, an Instron 5866 tensile tester, was operated with a crosshead speed of 50.8 mm/min and with a grip separation of 20 mm. The Young's modulus (E) and elongation-at-break will be reported as per the calculations

from the Instron software. The elongation at break is reported from the crosshead travel as a strain extensometer with sufficient travel was unavailable. All samples were tested under identical conditions.

The mechanical properties of the aligned nanocomposites were measured on the injection molded rectangular test bars. The moduli are reported based on tensile tests on the Instron 5866 tensile tester, which was operated with a crosshead speed of 50.8 mm/min with a gage length of 20 mm and a grip separation of 20 mm. All samples were tested under identical conditions.

4.4   Results and Discussion

4.4.1   Surfactant Suitability and PC Degradation Analysis

Prior to the melt-blending of the PC/mmt nanocomposites, the thermal stability of the organo-mmt was examined via TGA under inert (nitrogen) and oxidizing (air) atmospheres to elucidate the thermal stability of the surfactants (see **Table 4.1**, also refer to **Appendix 4.6.2** for the full data curves). The literature reports alkyl-ammonium modified mmt, similar to the surfactant chemistries of the commercial clays used in this study – C30B, C25A, and I42E, have degradation onset temperatures ($T_{0.05}$) below the melt-blending temperature of PC.[**8**] The quaternary phosphonium surfactants in the literature [**14**] reported only the degradation temperatures under inert conditions. Also, quaternary phosphonium surfactants utilized here had chemical structures in some instances from those in the literature, thus we must determine the applicability of such

surfactant treatments under atmospheres comparable to those that would be encountered during melt-blending of potential nanocomposites.

Table **4.1**

Table **4.1**: Thermogravimetric analysis of the conventional and alternative surfactant treatments for mmt under an oxidizing (air) and inert (N_2) atmosphere.

organo-mmt		$T_{0.05}$ (air) (ºC)	$T_{0.05}$ (N_2) (ºC)	$T_{Max\,MLR}$ (air) (ºC)	$T_{Max\,MLR}$ (N_2) (ºC)
C25A	mmt	260	279	297	312
I42E	mmt	244	274	254	310
C30B	mmt	261	301	268	391
imm-mmt	mmt	273	353	340	409
P-3C$_4$C$_{12}$	mmt	278	360	270	446
P-3PhC$_{12}$	mmt	315	311	324	321
P-4C$_8$	mmt	297	387	275	446

The lower onset of degradation temperatures ($T_{0.05}$) were confirmed for the quaternary ammonium modified mmt's. However, the alternative surfactant chemistries have superior thermal stability, especially with respect to the quaternary phosphonium modified mmt's, which in turn offers opportunities for stable melt-processed PC/mmt nanocomposites. Even with the improved thermal stability of the phosphonium and imidazolium surfactants, some degradation is expected to occur during melt-blending as the extrusion temperature was 280 °C and injection molding was at 295 °C (values which can further increase under the high-shear conditions).

Two distinct observations were made during the melt-blending of the PC/mmt nanocomposites, both of which are strong indicators that matrix degradation had occurred during the melt-blending process: (1) color formation was noted independent of surfactant chemistry and (2) qualitatively, in all cases the ease of flow of the

nanocomposites increased compared to the unfilled PC during injection molding, suggesting the viscosity decreased as a function of PC matrix degradation.

Analysis of the anticipated PC matrix degradation during melt-blending was completed through GPC molecular weight analysis of extracted PC from the injection molded PC and PC/mmt nanocomposites and through thermogravimetric analysis of the injection molded nanocomposites (see **Table 4.2;** also see **Appendix 4.6.2** for full data curves). A decline in the PC molecular weight was observed upon nanocomposite formation in all cases. Here we focus solely on the weight average molecular weight (M_w). A portion of the degradation products are below the detection limits of the GPC columns preventing a baseline to baseline integration when calculating the molecular weight, which in turn has led to inaccurate M_n readings.

Table **4.2**

Table **4.2**: Molecular weight (GPC) of the extracted PC from the melt-blended nanocomposites and thermogravimetric analysis (TGA) of the melt-blended nanocomposite bars after the injection molding process. All nanocomposites contained 3 wt. % mmt.

Sample	M_n (kg mol^{-1})	M_w (kg mol^{-1})	$T_{0.05}$ (air) (°C)	$T_{max\ MLR}$ (air) (°C)
Unfilled PC	22.1	50.6	452	500
PC/C30B	17.6	45.4	402	510
PC/C25A	18.8	38.2	413	513
PC/I42E	16.2	31.1	413	522
PC/imm-mmt	18.9	37.5	421	507
PC/P-3C$_4$C$_{12}$	17.6	33.7	446	520
PC/P-3PhC$_{12}$	17.4	34.2	447	515
PC/P-4C$_8$	15.0	28.4	440	512

Surprisingly, the improved thermal stability of the phosphonium surfactants was accompanied by more severe degradation during melt-blending compared to ammonium and imidazolium surfactants, indicating that the phosphonium surfactant chemistry catalyzes some degradation reactions of PC. The quaternary ammonium surfactants are, generally speaking, better from a molecular weight standpoint than even the imidazolium surfactants. The overall thermal stability (TGA) of the PC/quaternary phosphonium-mmt nanocomposites seems to be unaffected by mmt addition, and shows improvement over the alkyl-imidazole and quaternary ammonium modified mmt based nanocomposites which undergo a decline in the onset of degradation compared to unfilled PC (**Table 4.2**).

Figure **4.2**
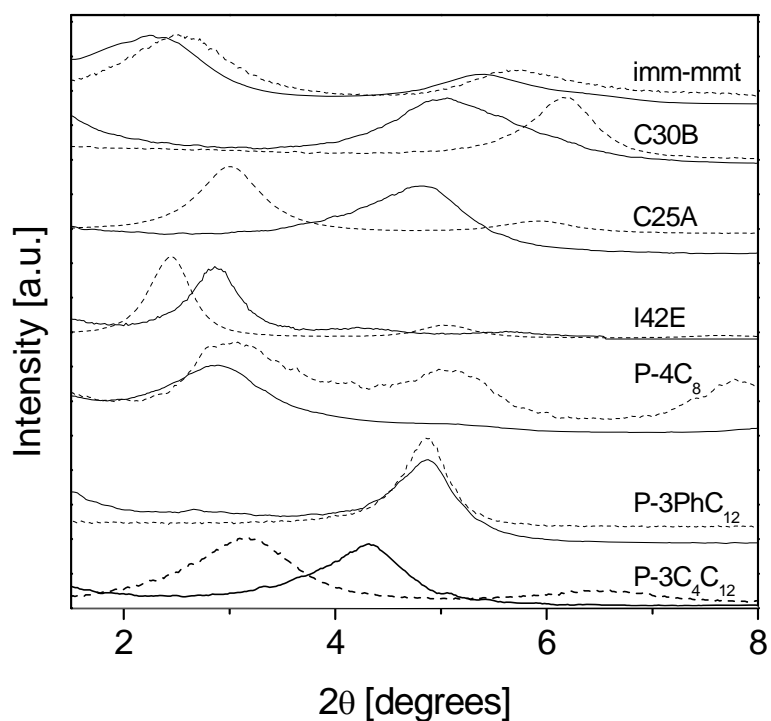
Figure **4.2**: XRD analysis of organo-mmt (solid lines) and the corresponding injection molded PC/mmt nanocomposites (broken lines) with varied mmt surfactant chemistry.

The dispersion of the melt-blended nanocomposites was analyzed via XRD to determine the morphologies of the subsequent nanocomposites with varied surfactant chemistry (see **Figure 4.2**). In order to select the proper candidate for optimization of the mechanical properties, it is important to examine the degradation characteristics coupled with the dispersive and mechanical behaviors. XRD analysis indicated several systems exhibited the classic d_{001} shift to lower 2θ values from the d_{001} of pure organo-mmt signifying the gallery intercalation of the host polymer matrix during melt-blending, a strong indicator of the formation of an intercalated nanocomposite. The remainder of the nanocomposites displayed no change or even slight reductions in the interlayer spacing as defined by Bragg's law (from the peak of the diffracted intensity) upon nanocomposite formation via extrusion and injection molding (see **Table 4.3**).

Table **4.3**

Table **4.3**: XRD d-spacing of the organo-mmt and the corresponding PC/mmt nanocomposite as calculated from Bragg's law from the peak diffracted intensity. All nanocomposites contain 3 wt. % mmt.

organo-mmt	organo-mmt d-spacing (nm)	PC/mmt nanocomposite d-spacing (nm)
C30B	1.8	1.4
C25A	1.8	2.8
I42E	3.1	3.6
imm-mmt	3.7	3.5
P-3C$_4$C$_{12}$	3.1	2.9
P-3PhC$_{12}$	1.8	1.8
P-4C$_8$	2.1	2.8

Classifying the dispersion of such systems through complementary TEM analysis is required if definitive conclusions with respect to the dispersion are to be drawn. We

find this to be unnecessary as we are mainly interested in choosing the mmt system with the best combination of degradation and mechanical behaviors. When considering the aforementioned degradation characteristics of the nanocomposites and the mechanical properties analysis below, the surfactant chemistry choice is obvious.

The mechanical properties of the nanocomposite systems were examined by tensile testing (see **Table 4.4**). The focus is directed to the relative modulus enhancements and the corresponding brittleness (reduction in elongation at break) caused by the introduction of the layered silicate.

Table **4.4**

Table **4.4**: Instron analysis of the mechanical properties of the melt-blended PC/mmt nanocomposites.

organo-mmt	wt. % mmt	Relative Modulus (E_{nano}/E_{neat})	Elongation at Break (%)
C30B	3	1.18	68 (± 6)
C25A	3	1.22	44 (± 17)
I42E	3	1.15	18 (± 3)
imm-mmt	3	1.10	63 (± 15)
P-3C$_4$C$_{12}$	3	1.17	12 (± 3)
P-3PhC$_{12}$	3	1.26	19 (± 7)
P-4C$_8$	3	1.11	35 (± 14)

When considering the degradation and mechanical behaviors – we find the quaternary ammonium based C30B mmt and the C25A mmt have relative modulus improvements on the order of 20 % – maintain nearly half of their elongation at break, and experience at most a 25 % reduction in their molecular weight upon nanocomposite formation. In contrast the conventionally filled composites (P-3C$_4$C$_{12}$, P-3PhC$_{12}$) showed similar improvements in E, but a substantial reduction in the strain at break. Furthermore,

we conclude the alternative high thermal stability surfactant chemistry did not limit PC degradation, and in fact appeared to catalyze more PC degradation compared to the common quaternary ammonium surfactant chemistries. The improvements in relative modulus were slightly greater in the C25A mmt and less severe color formation was developed (as determined by Ultraviolet-visible spectroscopy see **Appendix 4.6.2**). Therefore, the attempts to optimize the mechanical properties of the nanocomposite were carried out on the commercially available C25A mmt based nanocomposites (which is modified by dimethyl, hydrogenated tallow, 2-ethlyhexyl quaternary ammonium surfactant).

4.4.2   Mechanical Properties Optimization via mmt Filler Alignment

PC/C25A mmt nanocomposites were prepared via melt-blending and subsequent injection molding with varied (injection molded) bar thickness such that varying shear rates would be developed during the injection molding process. The goal was to alter the degree of alignment achieved during the melt-blending process. The apparent shear rate during injection molding ($\dot{\gamma}$) can be estimated using **Equation 4.1** where Q is the flow rate of the polymer during injection molding, h is the profile thickness, and w is the channel width in a given rectangular flow channel.[**21**] Three different thickness bars (1 mm, 2 mm, and 3.2 mm) were utilized in order vary the degree of alignment of the mmt platelets during injection molding as the shear rate is highly dependent upon the sample geometry.

Equation **4.1**

$$\dot{\gamma}_{app} = \frac{6Q}{wh^2}$$
(Equation **4.1**)

Varied mold temperatures were also utilized (49 °C and 80 °C) with the idea of preventing complete relaxation of the mmt platelets from their highly aligned state developed during injection molding. The lower mold temperature results in a thicker frozen layer during injection molding. This should improve the degree of alignment as relaxation will be less likely. A cross-sectional view of the injection molded bar illustrates the direction of flow during injection molding (see **Figure 4.3**).

Figure **4.3**
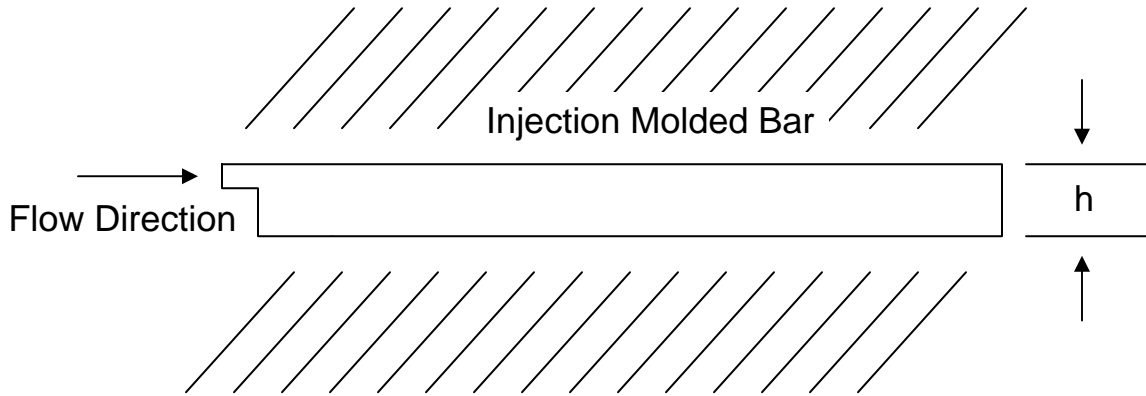
Figure **4.3**: A cross-sectional view of the injection molded rectangular test bar.

First, the overall dispersion was analyzed via 2D-XRD to establish if variations in the d-spacing of the nanocomposites took place during injection molding as a function of the varied processing conditions (see **Figure 4.4** and see **Appendix 4.6.2** for the full data set). An identical orientationally-averaged intercalated morphology is developed as the peak diffracted intensity is equivalent independent of processing conditions (i.e., molded

bar geometry, mold temperature, processing method). This holds true even in the zero-shear rate process of solution blending as again, no deviation in the peak of the diffracted intensity on the 2θ scale is observed (as expected from thermodynamic arguments).

Figure **4.4**
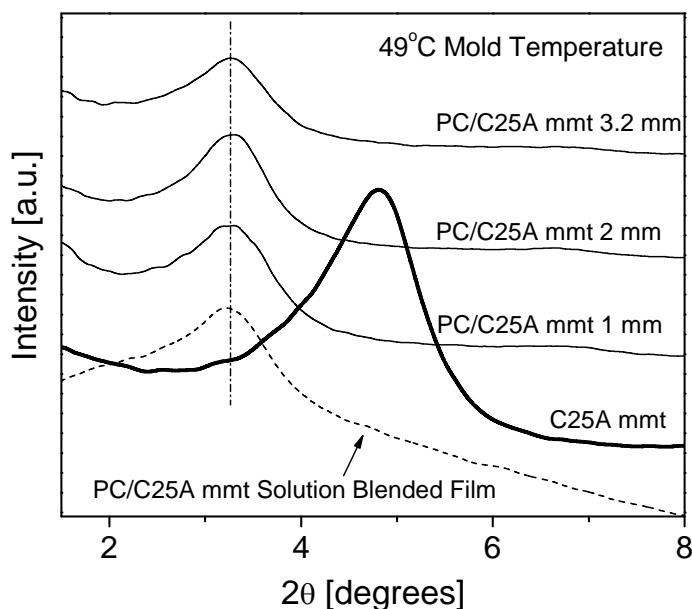
Figure **4.4**: 2D-XRD analysis of the dispersion of the PC/mmt nanocomposites with varied shear rates.

The mmt alignment of the nanocomposites was probed via 2D-XRD in all three potential axes of orientation (see **Figure 4.5**). When examining the azimuthal intensity of sections along these three axes we observe the development of distinct arcs during the scan of the 'front' section (see **Figure 4.6**). Samples developing arcs (see **Figure 4.6c** and **Figure 4.7b,c**) are understood to have developed orientation – as would be expected from a high-shear process such as injection molding. It is also understood that as the arc width narrows, the degree of alignment in that principal direction increases.

Figure **4.5**
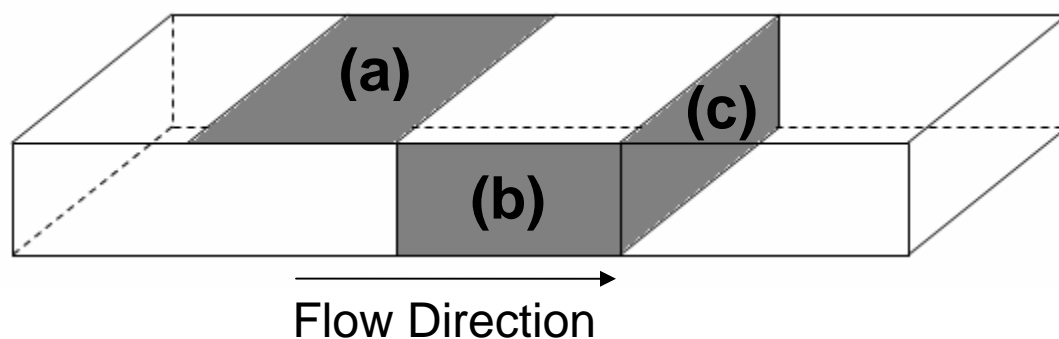
Figure **4.5**: Representation of the sections of the nanocomposite bars that were examined via 2D-XRD covering all the three potential axes of orientation: (a) the 'face', (b) the 'side', and (c) the 'front'.

Figure **4.6**
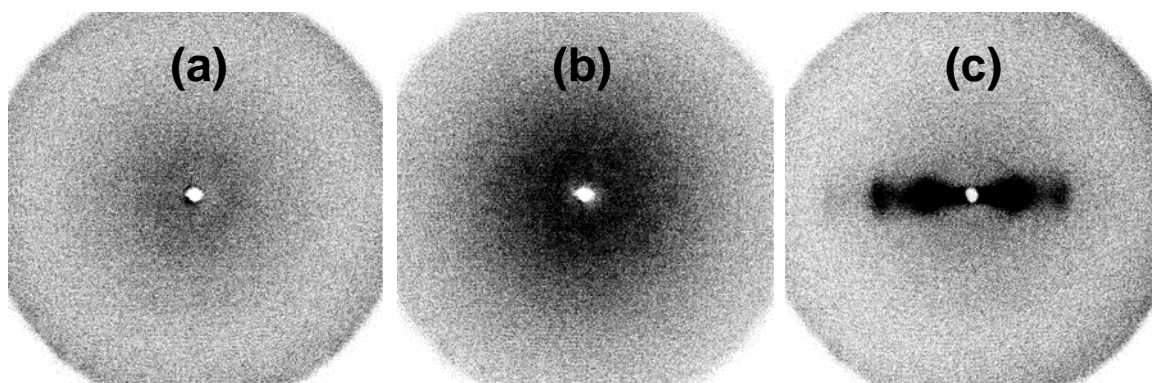
Figure **4.6**: 2D XRD scans for the 1 mm PC/mmt nanocomposite molded at the 49 °C mold temperature where the three axes are probed: (a) is a section from the 'face', (b) is a section from the 'side', and (c) is a section from the 'front'; orientation is observed in the 'front' section.

Upon evaluation of these 2D-XRD scans of the azimuthal intensity on the 'front' sections (see **Figure 4.7**), we find indications of alignment in the injection molded nanocomposites. 2D XRD patterns of non-aligned nanocomposites develop a characteristic ring, such as the solution blended nanocomposite film (**Figure 4.7a**), since

they have a random orientation in the principal direction. Likewise, when considering the systems of study here, we were able to successfully vary the processing such that distinct differences in the alignment were developed across the various samples as notable changes in the arc width and overall intensity were noted.

Figure **4.7**

| (a) Typical PC/C25A mmt Solution Blended Film | (b) Typical PC/C25A mmt 1 mm IM Bar | (c) Typical PC/C25A mmt 3.2 mm IM Bar |
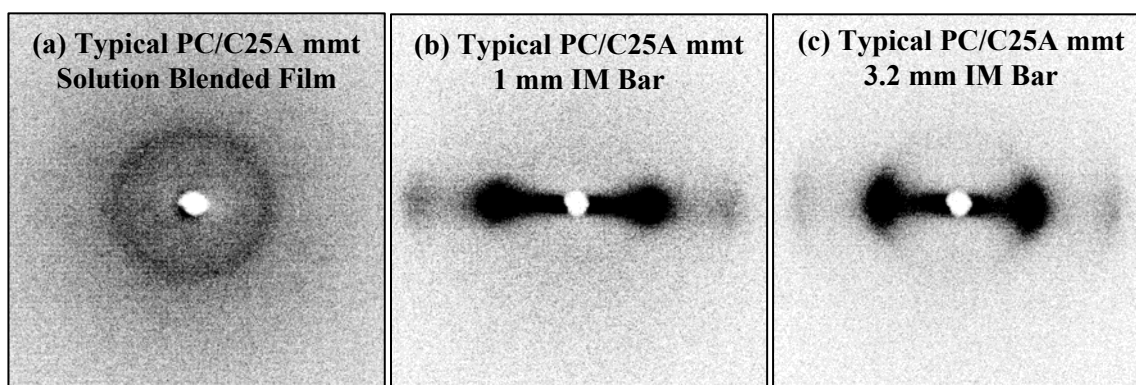
Figure **4.7**: 2D XRD scans for the PC/mmt nanocomposites where: random alignment occurs in a 200 micrometer solution blended film (a), and high degrees of alignment occur in the injection molded 1 mm (b) and 3.2 mm (c) melt-blended nanocomposites.

A numerical estimation for the degree of alignment/orientation, order parameter, can be obtained by calculating the Herman's Orientation Parameter (HOF).[**22**] In this work raw data in the form of intensity was plotted as a function of the azimuthal angle from a 2D XRD scan. The background intensity was subtracted and the maximum intensity peak (I_{max}) was shifted to an azimuthal angle of 180°. Once these factors were corrected, the average cosine squared of Φ is determined by evaluating **Equation 4.2** where I is the intensity and Φ is the azimuthal angle.

Equation **4.2**

$$<\cos^2 \Phi >= \frac{\int_0^{2\pi} I(\Phi)\cos^2(\Phi)\sin(\Phi)d\Phi}{\int_0^{2\pi} I(\Phi)\sin(\Phi)d\Phi} \qquad \text{(Equation 4.2)}$$

The orientation parameter may then be found by evaluating **Equation 4.3** with the average cosine squared value acquired from **Equation 4.2**. When $S_d = 1$ there is perfect alignment in the principal direction. Conversely, $S_d = 0$ denotes random alignment, and $S_d = -0.5$ denotes perfect alignment in the transverse direction (normal to the principal direction).

Equation **4.3**

$$S_d = \frac{3 <\cos^2 \Phi > -1}{2} \qquad \text{(Equation 4.3)}$$

When examining the degree of mmt platelet orientation developed during injection molding, we find the thinner bars generally developed a higher degree of orientation (see **Table 4.5**), as expected. This may be attributed to the synergy of reduced relaxation time for the platelets (as the no-flow temperature is reached quicker in the thinner bars) and the greater shear developed during the injection molding process in the thinner profiles. Likewise, the difference in the degree of orientation between samples from the 49 °C and the 80 °C mold temperature is most likely associated with the greater ability of the higher mold temperature samples to allow for better mmt platelet relaxation (when comparing between samples of the same thickness).

Table **4.5**

Table **4.5**: Herman's orientation parameters (S_d) of the aligned PC/mmt nanocomposites as determined by analysis of the 2D XRD plots.

h	I.M. Press	Q (mm^3/sec)	Mold Temperature (ºC)	Shear Rate (sec^{-1})	H.O.F - S_d
1 mm	Milacron	57400	49	27000	0.761
1 mm	Milacron	57400	80	27000	0.716
2 mm	Milacron	57400	49	6800	0.743
2 mm	Milacron	57400	80	6800	0.677
3.2 mm	Milacron	57400	49	2800	0.714
3.2 mm	Milacron	57400	80	2800	0.695
3.2 mm	Boy	9600	25	500	0.664

TEM imaging was utilized to probe the dispersive characteristics of the nanocomposites and to visually connect the degree of mmt platelet alignment to the respective HOF values. The alignment of the mmt platelets was probed in two regions within the injection molded bar: (1) near the surface of the injection molded bar with the microtomed sections being taken within 20 microns from the surface (when speaking from a thickness standpoint), and (2) near the center of the bar.

Analysis of the thinnest, highest shear rate sample (1 mm thick), that developed the greatest Herman's factor (S_d = 0.761) via TEM reveals a substantial degree of preferential mmt alignment in the principal direction and the well-dispersed intercalated morphology is confirmed (see **Figure 4.8**).

Figure **4.8**
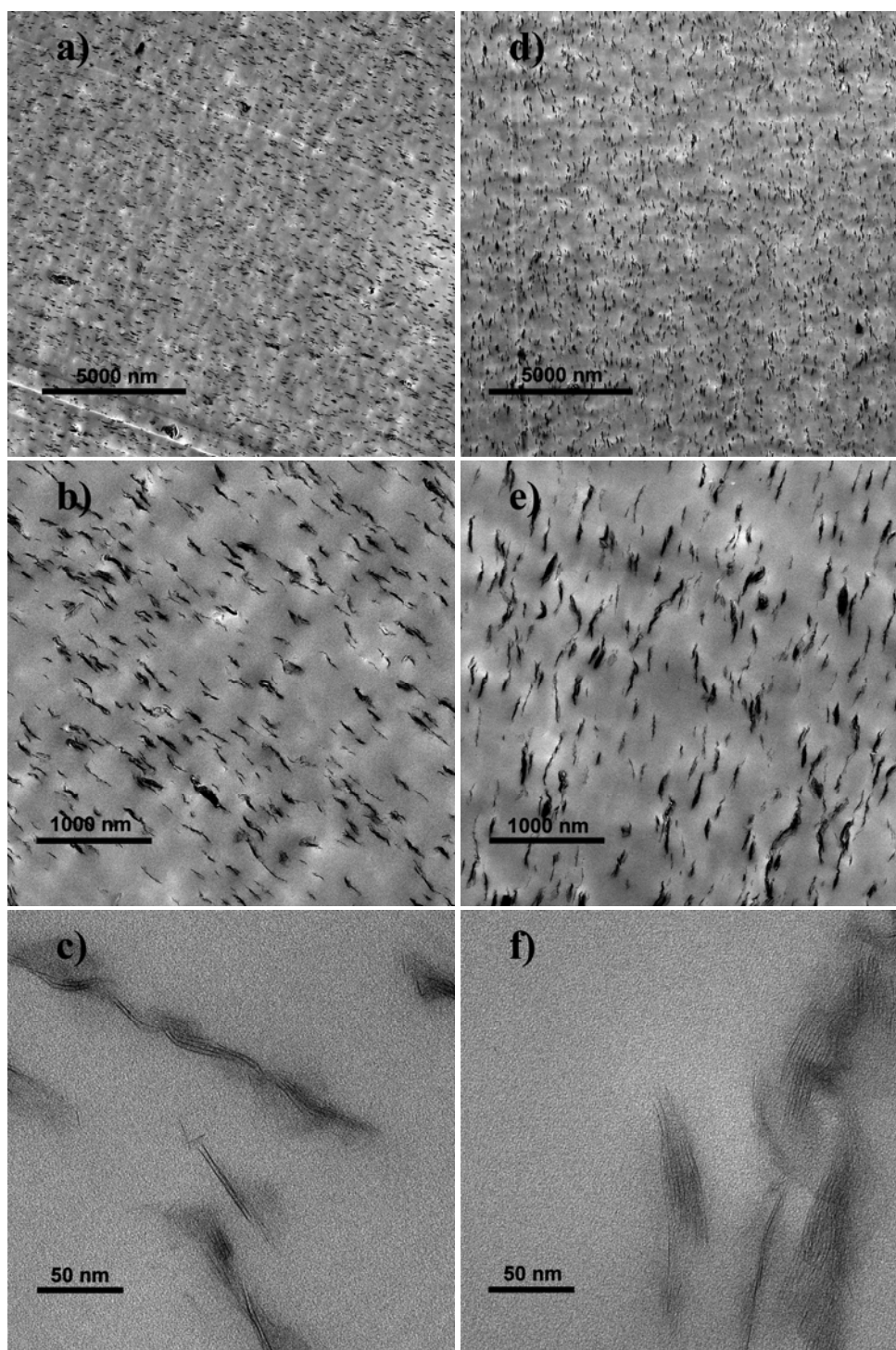
Figure **4.8**: TEM images of the 1 mm PC/C25A mmt nanocomposite (S_d = .761): a-c) microtomed 20 micrometers from the bar surface, d-f) sectioned from the bar center.

Figure **4.9**
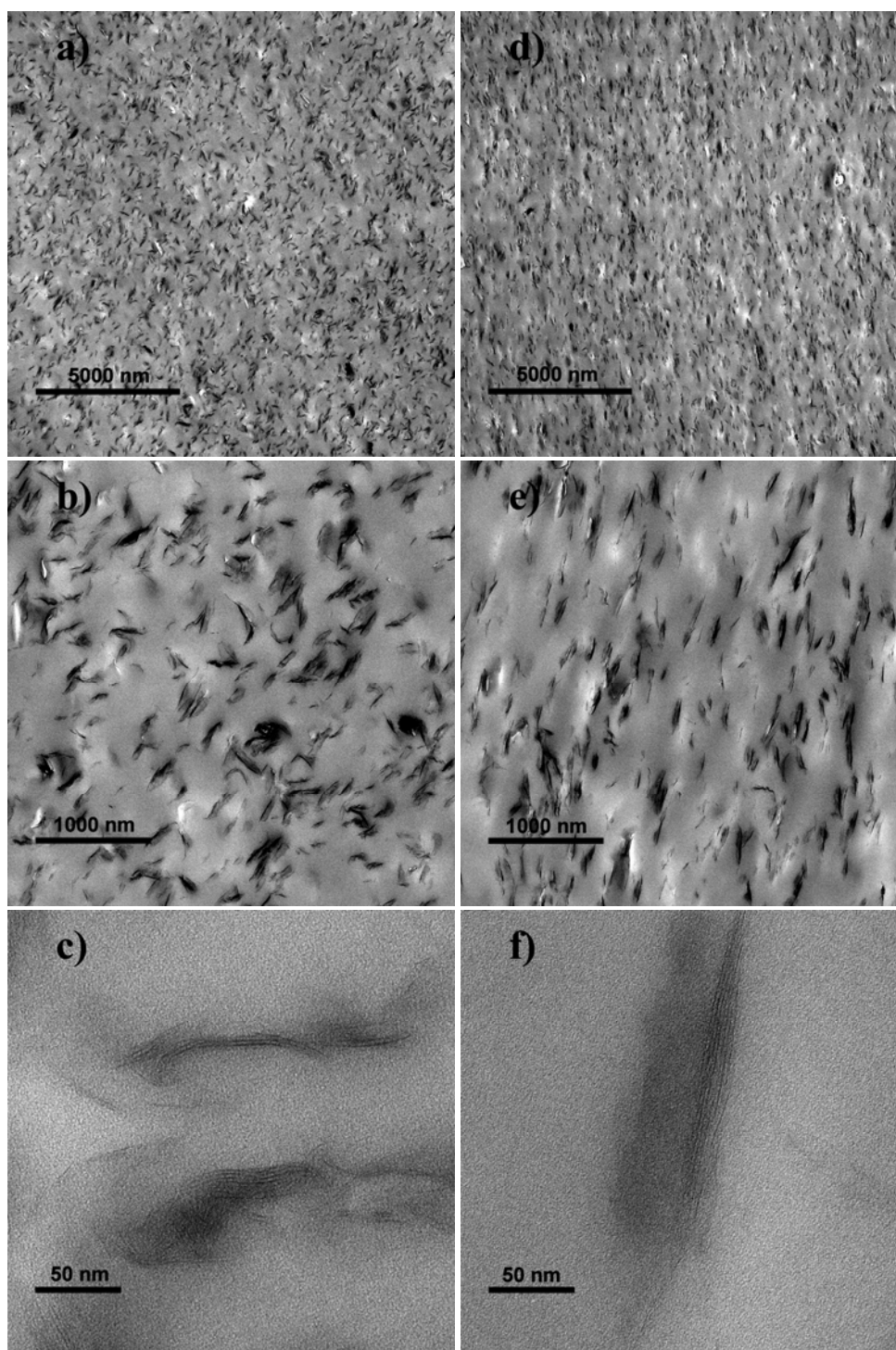
Figure **4.9**: TEM images of the 3.2 mm PC/C25A mmt nanocomposite (S_d = .664): a-c) microtomed 20 micrometers from the bar surface, d-f) sectioned from the bar center.

The lowest shear rate sample from injection molding, the 3.2 mm PC/C25A mmt nanocomposite (see **Figure 4.9**) melt-blended on the smaller injection molding machine (Boy 22D), also has a significant degree of alignment in the principal direction (Sd = .664) – but lacks the startling overall degree of alignment observed in the highest shear rate sample.

We again confirm the well-dispersed intercalated morphology of the nanocomposite. The alignment at/near the surface in this thicker profile (**Figure 4.9a-c**) is less than the corresponding alignment at the center of the bar, and is believed to originate from a combination of fountain flow, the fact the sample develops much lower shear, and the frozen layer would be greatest in the 25 °C mold (**Figure 4.9d-f**).

In general, considering the nanocomposite morphology, we observe small tactoids that vary from as few as two individual layers to as many as ten layers per stack in both series of nanocomposites. The diminutive tactoid size may be attributed to shear stress as these forces combine to overcome the strong adhesive forces of the multilayer structure during melt-blending to allow for tactoid breakdown. This shear induced tactoid breakdown is apparent when considering the 1 mm and 3.2 mm thick samples side-by-side where we find the overall tactoid size to be reduced in the higher shear 1 mm thick specimen (since the dispersion thermodynamics are identical).

The first segment of this study indicated a strong decline in the PC molecular weight associated with nanocomposite formation. To ensure equivalent degradation had occurred across the spectrum of aligned samples, we again examined the molecular weight of the extracted PC from the unfilled bulk specimens and their corresponding nanocomposites. GPC analysis confirmed there were no distinct variations in the

molecular weight amongst the nanocomposites (see **Table 4.6**). Full GPC curves can be

found in **Appendix 4.6.2**.

Table **4.6**

Table **4.6**: GPC molecular weight analysis of the extracted PC polymer from the identically processed unfilled PC and the aligned PC/C25A mmt nanocomposites with varying bar thickness and mold temperature. GPC was run with THF as the carrier solvent with polystyrene standards.

h	Mold Temperature (°C)	Unfilled M_w (kg mol^{-1})	Nanocomposite M_w (kg mol^{-1})	% Reduction
1 mm	49	52.3	36.8	30
2 mm	49	52.2	36.3	30
3.2 mm	49	51.7	39.1	24
1 mm	80	53.2	38.7	27
2 mm	80	53.0	37.0	30
3.2 mm	80	52.7	36.7	30
3.2 mm	25	50.6	38.2	25

Therefore, when considering the similar intercalated morphologies and equivalent

molecular weight degradation of the aligned nanocomposites, the sole remaining factor

that could impact the mechanical properties of the nanocomposite is the variation in the

degree of alignment of the mmt filler. Examination of the mechanical properties of the

melt-blended flexural bars was completed via tensile testing analysis (see **Figure 4.10**).

The tensile test direction was parallel to the direction of mmt platelet alignment. Our

equipment was not sufficient to test in the perpendicular direction. The relative modulus

of the nanocomposites is effectively equivalent regardless of degree of alignment. At the

outset, it was believed that improving the degree of alignment of the mmt platelets would

drive the modulus of the nanocomposites higher. The potential also exists that a greater

range of degrees of alignment are needed as we have a relatively narrow range here in our

work. Perhaps if a Herman's parameter of 0.3, 0.5, and so on could be generated as a form of comparison we may see substantial differences in the relative modulus as a function of the degree of alignment.

Thus, based on the mechanical properties analysis below, when considering PC/mmt nanocomposites, it may be best to examine the effect of the surfactant chemistry on PC matrix degradation above all other considerations.

Figure 4.10
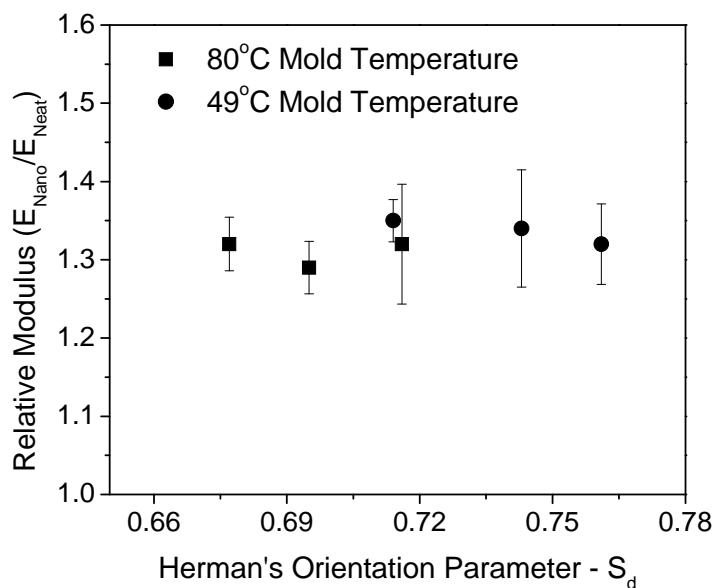
Figure **4.10**: Relative tensile modulus comparison with varied Herman's Parameter for the aligned PC/mmt nanocomposites.

4.5   Conclusions

Through the introduction of high thermal stability alternative surfactant treatments, an attempt was made to control the degradation introduced during the melt-

blending of PC/organo-mmt nanocomposites. In the absence of any stabilizer for PC, the high-thermal stability surfactant chemistries of the alkyl-imidazole and quaternary phosphonium chemistries actually resulted in more extensive molecular weight degradation for PC rather than limiting such decomposition. Surprisingly, the conventional quaternary ammonium modified montmorillonites provided the most favorable improvements in mechanical properties with the lowest PC matrix degradation (in the absence of any stabilizer for the PC). The commercially available C25A mmt had the most favorable mix of mechanical properties and limited matrix degradation, and was chosen as the candidate to attempt to maximize the mechanical properties of its nanocomposites through maximizing montmorillonite alignment.

The degree of filler alignment within the nanocomposites was effectively altered by varying the injection molded bar thickness, which in turn led to varied shear rates during injection molding. Generally speaking, as the shear rate increased, the degree of alignment as quantified by the Herman's Orientation Parameter from 2D XRD followed suit. At the same time, no significant variations in the d-spacing of the nanocomposites were observed. The PC molecular weight degradation upon nanocomposite formation was also independent of the melt-blending conditions or bar geometry. Most importantly, no definitive improvement in the mechanical properties was observed with increasing Herman's Orientation Parameter, probably due to the absence of any extensive polymer chain alignment. We conclude it is more important to focus on limiting the original matrix degradation during injection molding than to attempt to preferentially align the layered silicate, unless a unique application requires such alignment.

4.6   Appendix

4.6.1   Pertinent Chemical Structures

Figure **4.11**
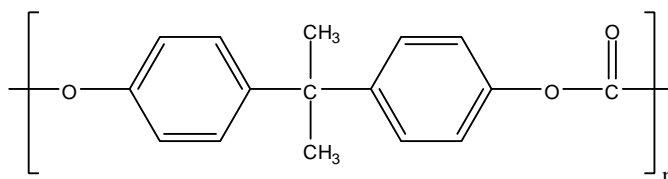
Figure **4.11**: Polycarbonate repeat unit structure.

Figure **4.12**
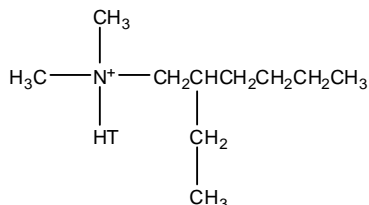
Figure **4.12**: Structure of the commercial Cloisite C25A surfactant, with HT referring to hydrogenated tallow which is 65% $C_{18}H_{37}$, 30% $C_{16}H_{33}$, and 5% $C_{14}H_{29}$, (C25A).

Figure **4.13**
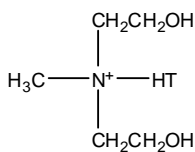
Figure **4.13**: Structure of the commercial Cloisite C30B surfactant, with HT referring to hydrogenated tallow which is 65% $C_{18}H_{37}$, 30% $C_{16}H_{33}$, and 5% $C_{14}H_{29}$, (C30B).

Figure **4.14**
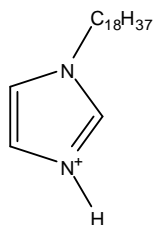
Figure **4.14**: Structure of the lab synthesized alkyl-imidazolium surfactant, (imm-mmt).

Figure **4.15**
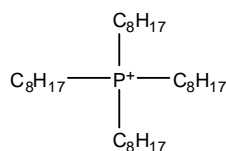
Figure **4.15**: Structure of the tetra-N-octylphosphonium surfactant, (P-4C$_8$).

Figure **4.16**
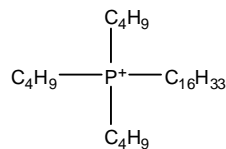
Figure **4.16**: Structure of the n-hexadecyltri-n-butyl surfactant, (P-3C$_4$C$_{12}$).

Figure **4.17**
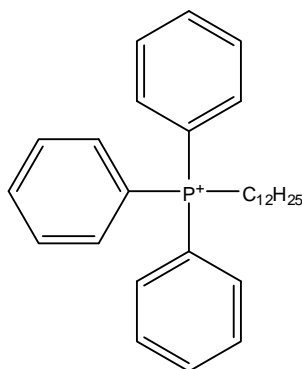
Figure **4.17**: Structure of the n-dodecyl triphenylphosphonium surfactant, (P-3PhC$_{12}$).

4.6.2 Additional Supporting Data

Figure **4.18**
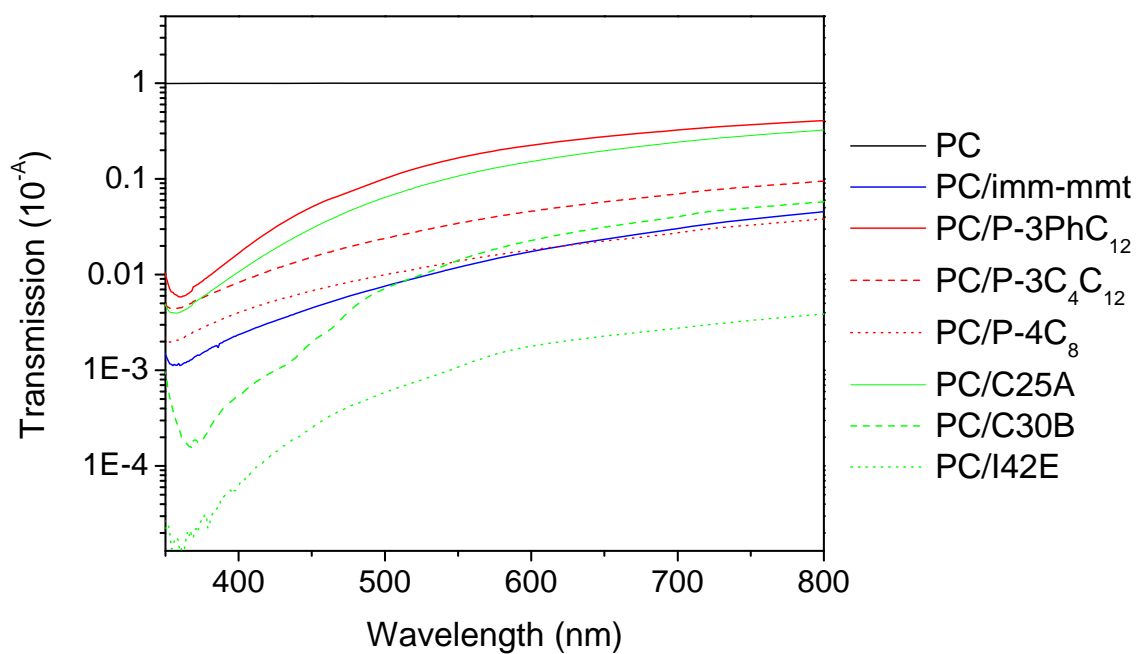
Figure **4.18**: UV-VIS spectroscopy transmittance measurements of the injection molded micro-flexural bars.

Table **4.7**

Table **4.7**: Yellowness Index (YI) calculated from transmittance values acquired from UV-VIS spectroscopy on the injection molded micro-flexural bars with corresponding scanned images for PC and the PC/organo-mmt nanocomposites. YI is calculated by dividing the difference between the transmission at 680 nm and 420 nm by the transmission at 560 nm. All samples were melt-blended without a stabilizer.
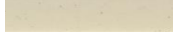
Sample	wt. % mmt	Y.I.	Scanned Image
PC	-	0.02	
PC/C25A	3	1.78	
PC/C30B	3	2.24	
PC/I42E	3	2.13	
PC/imm-mmt	3	1.87	
PC/P3C$_4$C$_{12}$	3	1.47	
PC/P3PhC$_{12}$	3	1.55	
PC/P4C$_8$	3	1.36	

Figure **4.19**
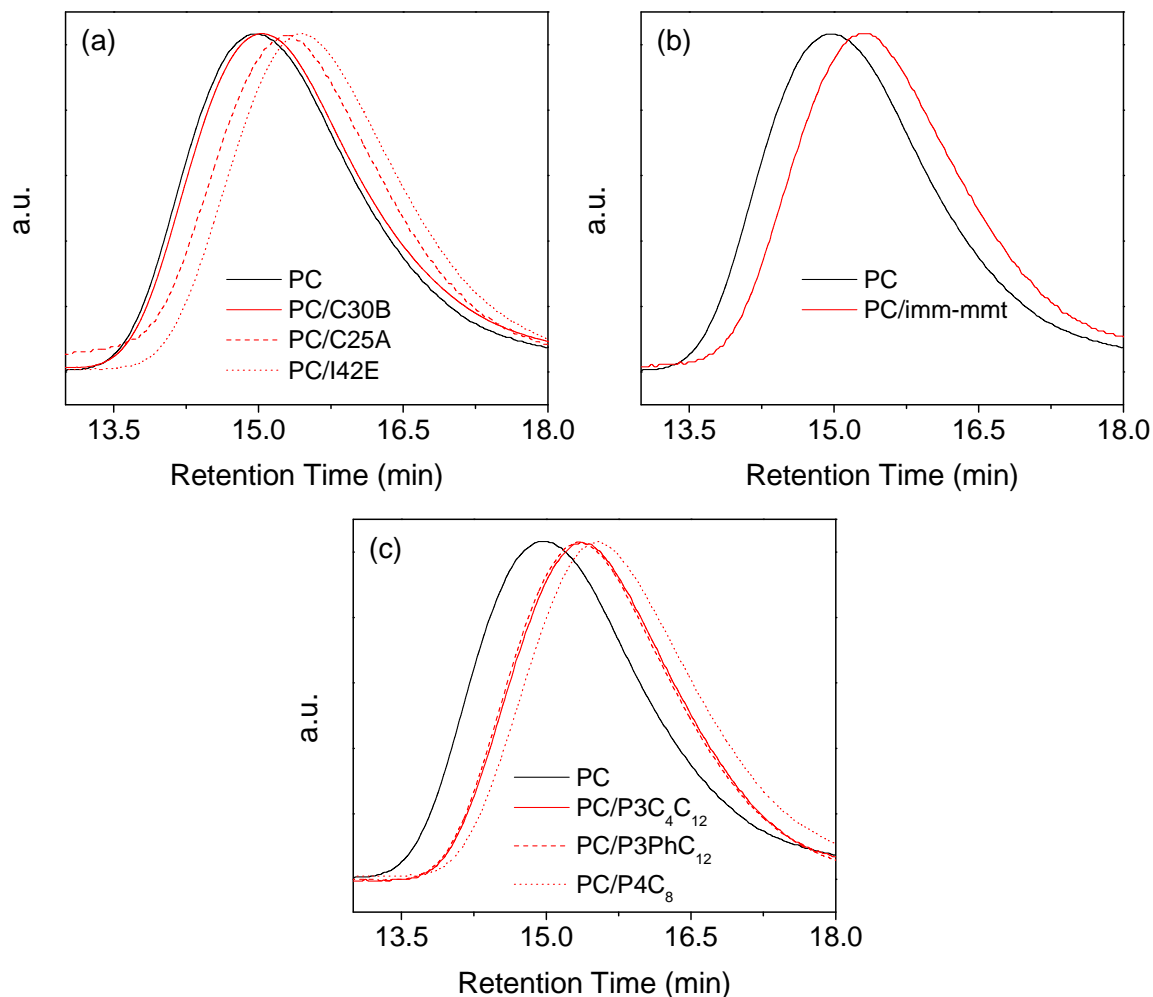
Figure **4.19**: GPC curves of extracted PC from the unfilled PC and the PC/organo-mmt nanocomposites: (a) Quaternary ammonium modified mmt, (b) alkyl-imidazolium modified mmt, and (c) Quaternary phosphonium modified mmt. All samples were injection molded at 25 °C on the Boy press. All curves are normalized by intensity for clarity purposes.

Figure **4.20**
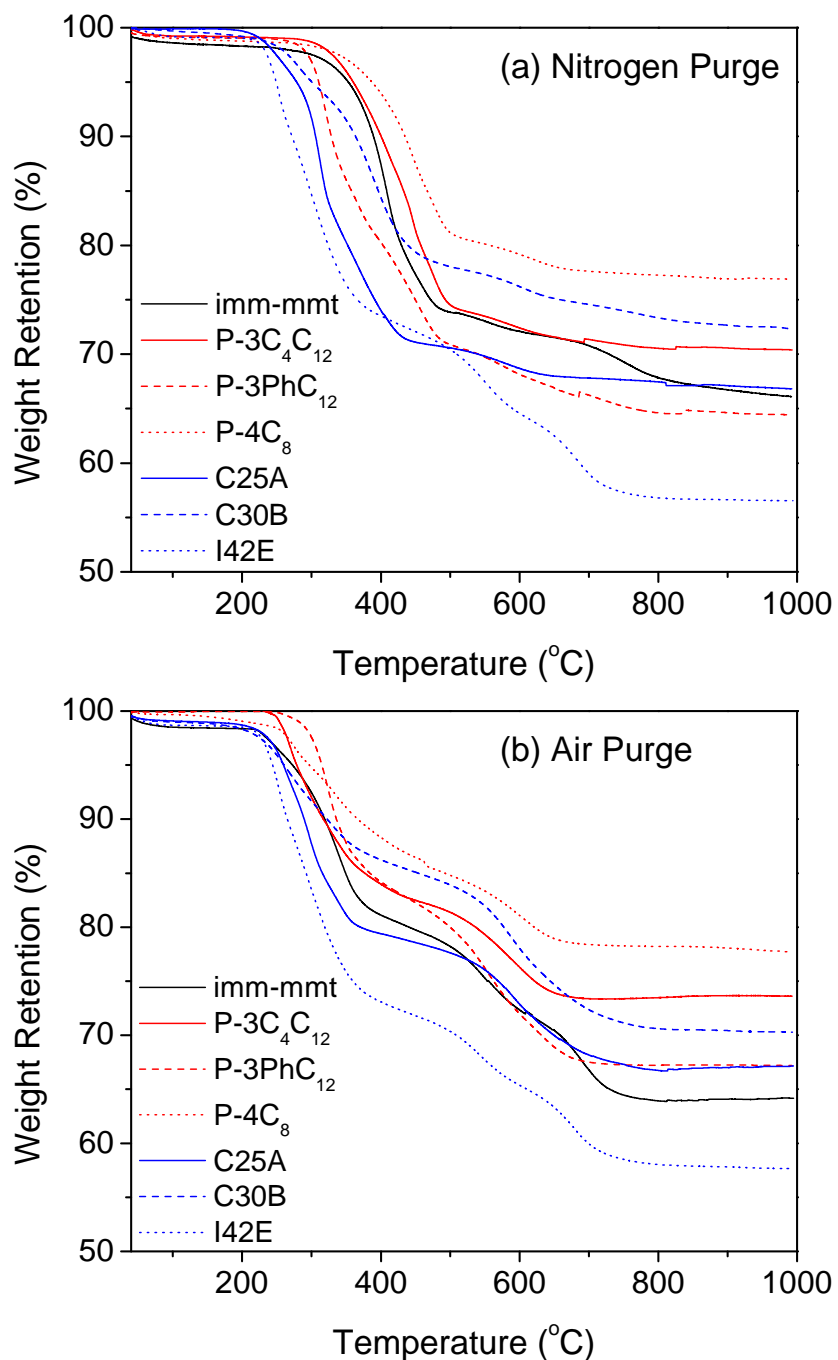
Figure **4.20**: TGA weight loss curves for organo-mmt run under: (a) nitrogen purge (100 mL/min) and (b) an air purge (100 mL/min) at a ramping rate of 10 °C/minute.

Figure **4.21**
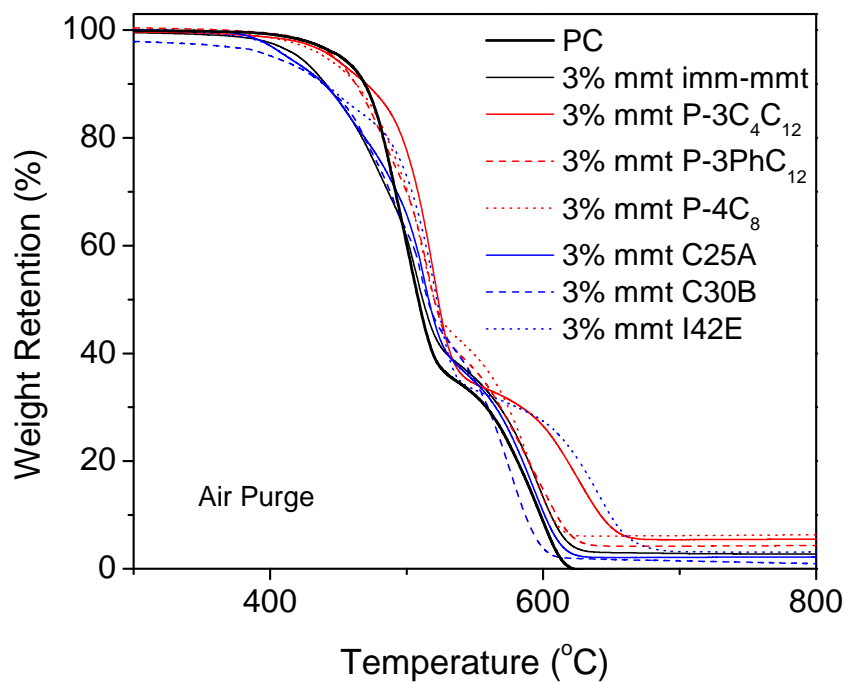
Figure **4.21**: TGA weight loss curves for injection molded PC/organo-mmt nanocomposites that were run under an air purge (100 mL/min) at a ramping rate of 10 °C/minute.

Figure **4.22**
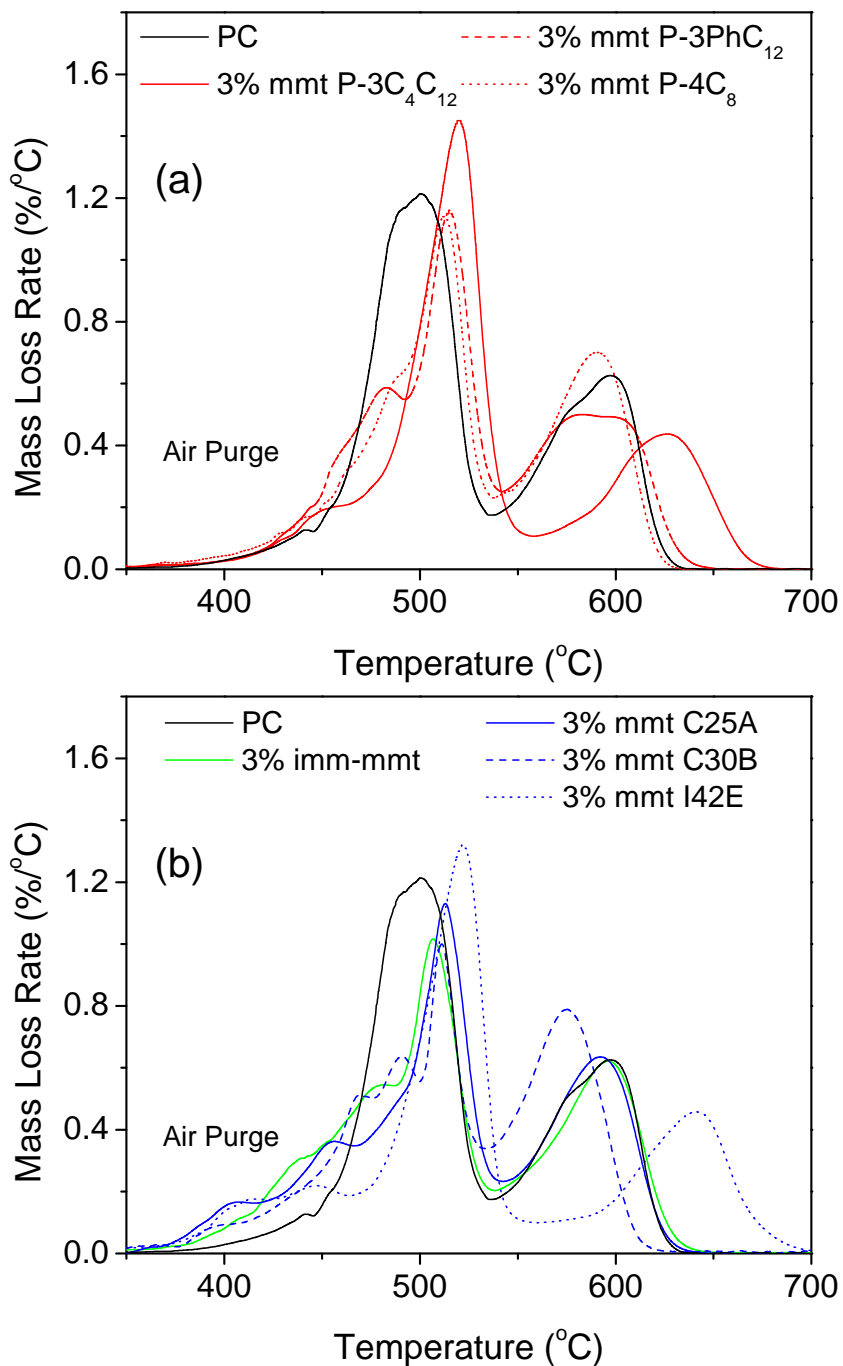
Figure **4.22**: Mass Loss Rate (MLR) curves of the injection molded (a) PC/quaternary phosphonium organo-mmt nanocomposites and (b) PC/quaternary ammonium and alkyl-imidazolium organo-mmt nanocomposites from the derivative of the TGA weight loss curves found in **Figure 4.21**.

Figure **4.23**
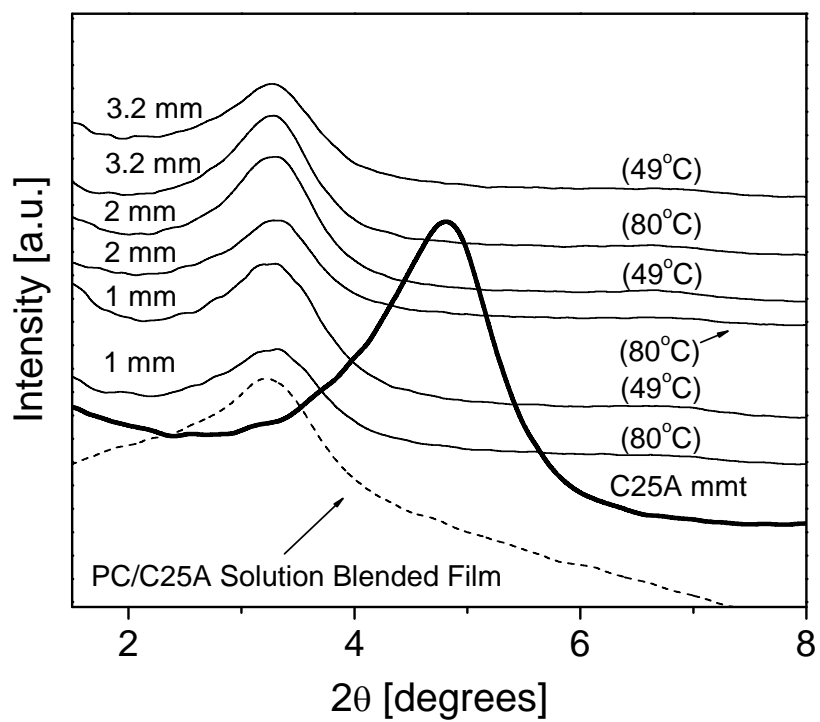
Figure **4.23**: XRD analysis of all samples examined in the aligned PC/mmt nanocomposites segment, with varied conditions.

Figure **4.24**
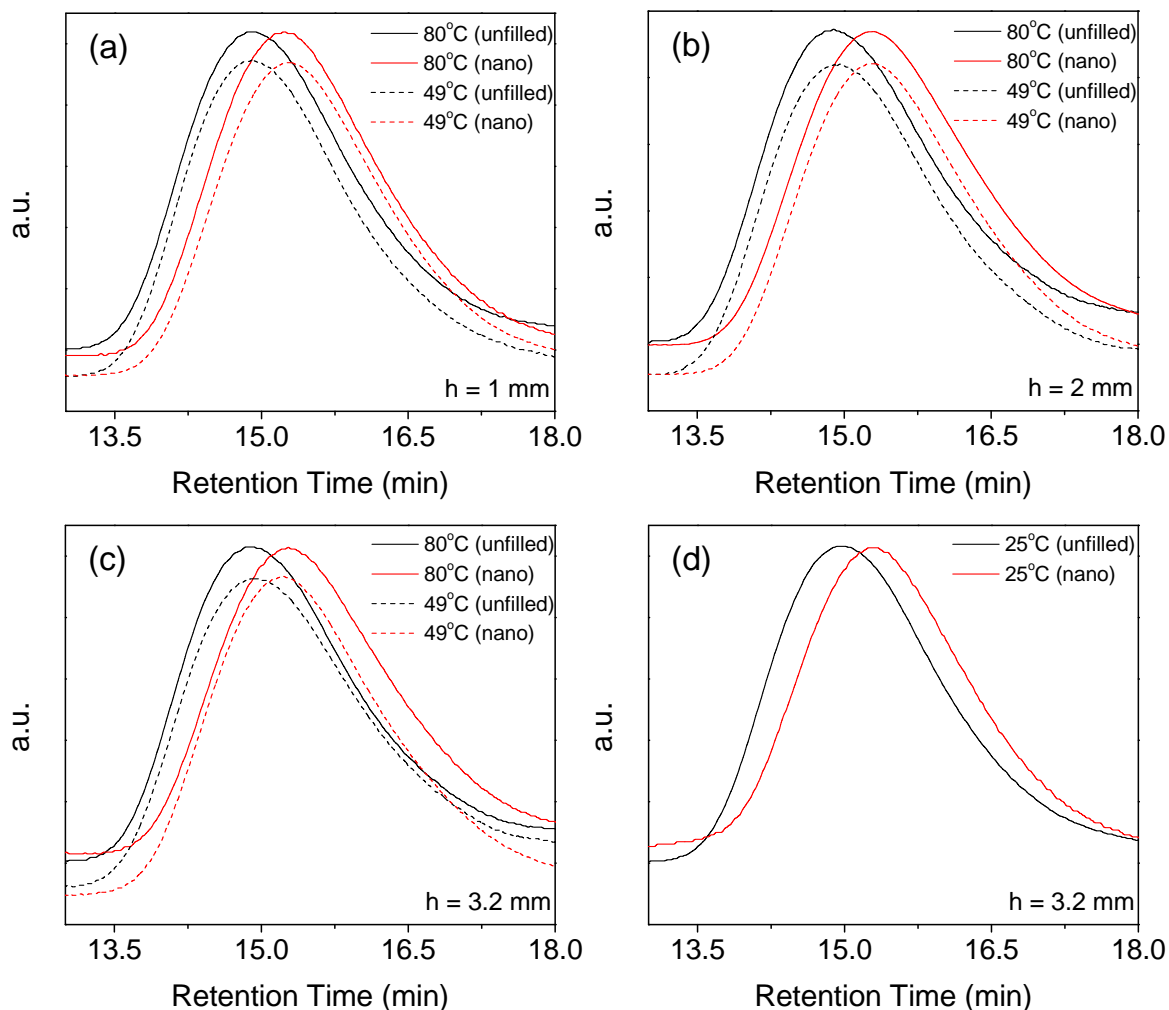
Figure **4.24**: GPC curves of the extracted PC from the unfilled PC and the aligned PC/mmt nanocomposites: (a) 1 mm bar thickness, (b) 2 mm bar thickness, (c) 3.2 mm bar thickness, and (d) 3.2 mm bar thickness with the mold temperature at 25 °C. The samples from (a), (b), and (c) were molded on the Cincinnati Milacron press and the samples from (d) were molded on the Boy press. All curves are normalized by intensity and are offset slightly on the y-axis (arbitrary units) for clarity purposes.

References

1.   Alexandre, M. and Dubois, P., *Materials Science and Engineering* 2000; R28:1-63

2.   Ray, S.S. and Okamoto, M., *Progress in Polymer Science* 2003; 28:1539–1641.

3.   Giannelis, E.P., Krishnamoorti, R., and Manias, E., *Advances in Polymer Science.* 1998; 138:107–148.

4.   Schilling, F.C., Ringo, W.M., Sloane, N.J.A., and Bovey, F.A., *Macromolecules* 1981; 14:532–537.

5.   Ghorbel, I., Akele, N., Thominette, F., Spiteri, P., and Verdu, J., *Journal of Applied Polymer Science* 1995; 55: 173–179.

6.   Pryde, C.A., and Hellman, M.Y., *Journal of Applied Polymer Science* 1980; 25: 2573–2587.

7.   Gaines, G.L., *Polymer Degradation and Stability* 1990; 27: 13–18.

8.   Xie, W., Gao, Z., Pan, W-P., Hunter, D., Singh, A., and Vaia, R., *Chemistry of Materials* 2001**;** 13:2979–2990.

9.   Yoon, P.J., Hunter, D.L., and Paul, D.R., *Polymer* 2003; 44:5323–5339.

10.   Yoon, P.J., Hunter, D.L., and Paul, D.R., *Polymer* 2003; 44:5341–5354.

11.   Mitsunaga, M., Ito, Y., Ray, S.S., Okamoto, M., and Hironaka, K., *Macromolecular Materials and Engineering* 2003; 288:543-548.

12.   Ke, Y., Long, C.F., and Qi, Z.N., *Journal of Applied Polymer Science* 1999; 71:1139–1146.

13.   Wang, Z.M., Chung, T.C., Gilman, J.W., and Manias, E., *Journal of Polymer Science: Part B: Polymer Physics* 2003; 41:3173–3187.

14.   Xie, W., Xie, R., Pan, W-P., Hunter, D., Koene, B., Tan, L-S., and Vaia, R., *Chemistry of Materials* 2002; 14:4837–4845.

15.   Chen, B. and Evans, J.R.G., *Scripta Materialia* 2006; 54:1581–1585.

16. Manias, E., Polizos, G., Nakajima, H., and Heidecker, M.J., **Flammability of Polymer Nanocomposites.** Editors: Wilkie and Morgan, Wiley & Sons, NJ, 2007.

17. Thostenson, E. T. and Chou, T-W., *Journal of Physics D: Applied Physics* 2002; 35:L77–L80.

18. Sennett, M., Welsh, E., Wright, J.B., Li, W.Z., Wen, J.G., and Ren, Z.F., *Applied Physics A – Materials Science and Processing* 2003; A76:111–113.

19. Park, C., Wilkinson, J., Banda, S., Ounaies, Z., Wise, K.E., Sauti, G., Lillehei, P.T., and Harrison, J.S., *Journal of Polymer Science: Part B: Polymer Physics* 2006; 44:1751–1762.

20. Koerner, H., Hampton, E., Dean, D., Drummy, L., Mirau, P., and Vaia, R., *Chemistry of Materials* 2005; 17:1990–1996.

21. Malloy, R.A., **Plastic Part Design for Injection Molding,** Hanser Publishers, New York, NY, 1994.

22. Alexander, L.E., **X-ray Diffraction Methods in Polymer Science,** Wiley, New York, NY, 1969.

Chapter 5

Melt-Blended Poly(ethylene terephthalate)/Polycarbonate Blends

5.1   Summary

Mechanical mixtures of two high-performance polymers, poly(ethylene terephthalate) (PET) and polycarbonate (PC), were produced via melt-blending. The blend morphology was phase immiscible, as expected in systems without extensive degree of transesterification. Transesterification reactions were found to be below the detectable limits of ATR-FTIR, and two distinct glass transition temperatures were observed via DSC and DMA studies, all indicating the presence of minimal copolymer formation. The addition of amorphous PC had little impact on the crystallization behavior of PET. We do observe a reduction in the spherulite size upon blend formation, although the overall degree of crystallinity was markedly unaffected. Prior to or concurrently with the PET spherulite nucleation and growth, PC and/or PET phase coalescence occurs such that larger crystallizable PET domains are developed.

5.2   Introduction

Mechanical blends of compatible and non-compatible polymers have drawn interest because of the novel blend behaviors that often develop by the mixing or the combination of two polymers with different property-sets, and the high potential

applicability of such blend in innovative applications.[1][2] PET/PC blends are a rather well-studied class of materials, both from a fundamental and an application standpoint, since they offer good abrasion, chemical, and impact resistance coupled with good rigidity and thermal stability. The literature generally focuses on the fundamental understanding –and on the subsequent optimization of the degradation and copolymer formation mechanisms– and its effect on the crystalizability of the PET in these blends.[3][4][5][6] It is well established that in the absence of transesterification reactions (copolymer reactions at the PET/PC interfaces), melt-blended PET/PC blends are immiscible.[5][6][7] It is understood that when transesterification reactions do occur, the rate of conversion is greatest in the PC rich blends with the highest overall ratios occurring in a 50PET/50PC blend.[8] The caveat to this route of achieving miscibility is that such transesterification reactions are typically limited and generally absent, unless excess catalyst from the PET polymerization process is present or additional catalyst is introduced to promote copolymer formation/miscibility (via catalysis of the ester-carbonate transesterification reaction).[7][9]

Phase behavior and domain sizes of PET/PC blends depend on the extent of transesterification reactions, PET/PC fractions present in the blend, and melt-processing conditions. In the absence of transesterification reactions the blend is immiscible and the domain size can be controlled through the melt-blending conditions (e.g. shear rate [10]) and post-blending thermal conditions. A mechanical blend with a ratio of 20PET/80PC developed PET regions that ranged in size from 0.5 to 2.0 micrometers. Even with such a narrow size distribution, the PET domain size could be controlled by varying the screw speed (and thus the mechanical shear).[10] Likewise, when the PET/PC ratio is inverted,

it is common to find PET domains approaching 100 micrometers. The post-blending thermal history can also influence phase behavior as annealing at high temperatures can lead to phase coalescence and may also promote transesterification reactions if catalysts for such reactions are present (intentionally or unintentionally). Domain reorganization as a function of transesterification has been well-documented.[11][12] The PET domain crystallization is typically hindered and the glass transition temperatures of PET and PC have been found to merge.[3][5][11][12]

Phase continuity of a polymer blend is governed by viscous effects. A relation has been developed by Jordhamo, Manson, and Sperling based on an approach that examines the viscosity (η) of the polymer phases (η_1, η_2) and the corresponding weight fraction of the phases (Φ_1, Φ_2) (see **Equation 5.1**).[13] Phase continuity is defined such that when x ≤ 1 phase 1 is the continuous phase, when $x \geq 1$ phase 2 is continuous, and when x approaches unity the phase behavior becomes co-continuous (dual phase continuity).

Equation **5.1**

$$\frac{\eta_1}{\eta_2} \times \frac{\Phi_1}{\Phi_2} = x \qquad\qquad (\text{Equation } \mathbf{5.1})$$

The phase continuity of PET/PC blends was examined with the aid of the viscosity data for the PET and PC studied in this work (see **Table 5.1**). Based on these values of viscosity at 280 °C, the processing temperature, if assigning the PC to be phase 1 and PET to be phase 2, we expect the PET phase to be the continuous phase for the blends of this study.

Table **5.1**

Table **5.1**: Viscosity data for PET (Voridian 12822) and PC (Makrolon 3208) acquired at T = 280 °C and $\dot\gamma = 600$ s^{-1}.

	η (Pa-s)
PET	240
PC	940

A phenomenon also observed within this work that will be briefly discussed and is different than phase coarsening is phase coalescence. Two types of phase coalescence are understood to occur in immiscible polymer blends: (1) flow driven coalescence which leads to breakup and produces a distribution of particle (phase domain) sizes, and (2) static coalescence which occurs during annealing and involves particle-particle fusion.[**14**]

Three factors are expected to influence the crystallization behavior of PET in the blends: (1) the reduction of crystallizable PET, proportional to the extent of transesterification reactions occurring, (2) the physical (*cf.* geometric) restriction by the amorphous PC domains, and (3) the possible nucleating effect of PC inclusions and or interfaces. In this body of this work, we will focus on the investigation of three blend compositions: (A) 75PET/25PC blend (PET rich), (B) 50PET/50PC blend (symmetric), and (C) 25PET/75PC (PC rich). The goal is to elucidate the full spectrum of the PET/PC blends crystalizability and produce a comprehensive study encompassing the crystallization behaviors, while at the same time reporting on the spherulitic structures and sizes, all in the absence of considerable transesterification reactions. We will also briefly report on the phase coalescence in PET/PC blends prior to the commencement of nucleation and growth of the PET crystals.

5.3   Experimental

5.3.1   Materials and Samples Preparation

Melt-blending (twin-screw extrusion followed by injection molding) was utilized to produce PET/PC blends. The PET in this study was a standard high molecular weight, high intrinsic viscosity (M_n = 35 kg mol^{-1}, 0.95 dl/g) homopolymer as provided by Voridian. The PC was a standard high molecular weight (M_n = 32 kg mol^{-1} as per PS standards), high viscosity grade provided by Bayer MaterialScience.

Twin-screw extrusion of the nanocomposites took place at BAYER MaterialScience on a Prism TSE 16TC extruder with an L/D ratio of 16, run at 280 °C with a screw speed of 280 to 330 RPM. The PET and PC were dried, at 100 °C overnight under vacuum, prior to pre-extrusion mixing –mechanized tumbling of the PET pellets and PC powder for 20 minutes. The pelletized extrudate was dried again under vacuum overnight at 100 °C, prior to injection molding of micro-tensile and flexural bars on a BOY 22D hydraulic injection molding press, operated with a barrel temperature of 295 °C with the mold at ambient conditions (see **Appendix 5.6** for the full melt-processing data sheets). Blend compositions of 75PET/25PC (PET rich), 50PET/50PC (symmetric) and 25PET/75PC (PC rich) were produced to compare to the bulk PET.

5.3.2   Mechanical Properties

The tensile properties of bulk PET and its blends were measured by tensile testing of injection molded micro-tensile bars. The tensile bars (dogbones) are ASTM D638

standard type IV specimen with a molded thickness of approximately 3.18 mm. The tensile tester, an Instron 5866 tensile tester, was operated with a crosshead speed of 50.8 mm/min. The Young's modulus (E), yield strength, and elongation-at-break will be reported as per the calculations from stress-strain curves on the Instron software. The elongation at break is reported from the crosshead travel, as a strain extensometer with sufficient travel was unavailable. It is also important to note the tensile properties were measured on the "as-molded" tensile bars with no post-molding annealing.

Dynamic mechanical analysis (DMA) was utilized to quantify the thermomechanical behavior. A TA Instruments Q800 Dynamic Mechanical Analyzer with a 35mm dual cantilever setup was utilized. The samples were studied using a standard constant frequency (1 Hz), constant strain (0.01 %) test, coupled with temperature sweep from 25 °C to 180 °C at a ramp rate of 4 °C/minute. The storage modulus (G'), the real part of the complex modulus that relates to the material's elastic modulus, along with the tan δ behavior, the damping coefficient that is an indicator of the glass transition temperature (T_g), will be of particular interest for this study.

5.3.3 Transesterification Analysis

The copolymer formation was monitored by attenuated total reflectance Fourier-transform infrared spectroscopy (ATR-FTIR) using a Digilab FTS 800 instrument. The surface of injection molded micro-flexural bars were analyzed with 64 scans at a resolution of 2 cm^{-1}, with three separate scans of each specimen being averaged prior to comparative analysis. When examining transesterification via infrared spectroscopy (IR),

three distinct bands are of particular interest: (a) the 1775 cm^{-1} band that corresponds to the carbonyl stretching of an amorphous aromatic carbonate (PC), (b) the 1720 cm^{-1} band associated with the carbonyl stretching of an aliphatic ester (PET), and (c) the 1740 cm^{-1} band associated with the stretching of a mixed aliphatic-aromatic carbonate, which is a product of the ester-carbonate transesterification reaction (see **Figure 5.1**).[8][15]

Figure **5.1**

Figure **5.1**: The products of the PET/PC ester-carbonate transesterification reaction leading to copolymer formation.[8][15]

Transesterification was also monitored via glass transition temperature (T_g) shifts with modulated differential scanning calorimetry (MDSC). The MDSC studies were performed on a TA Instruments Q100 DSC calibrated with sapphire and indium standards under helium purge with a secondary nitrogen purge. A conventional MDSC experiment was run in order to separate the reversing heat flux (glass transition) and the non-

reversing heat flux (crystallization and melting). Data from the MDSC scans were collected from a temperature ramp rate of 3 °C per minute with modulation of 1 °C every 60 seconds. The reversing heat capacity will be reported to best resolve the T_g (defined as the midpoint of the step change in reversing heat capacity).

5.3.4 Crystallization Behavior

The isothermal and non-isothermal crystallization behaviors of the PET and PET/PC blends were examined using DSC and polarized light optical microscopy (PLOM). The DSC studies were performed on the aforementioned TA Instruments Q100 DSC. The scanning rate was 10 °C/min in all cases, unless otherwise noted. The comparisons of as-molded and annealed samples were carried out on three specimens from each blend concentration. The PET crystallinity was calculated by **Equation 5.2** where ΔH_m is the enthalpy of fusion and ΔH_m° is the enthalpy of fusion of the perfect crystalline PET (125.5 J/g).[**16**]

Equation **5.2**

$$\chi_c = \frac{\Delta H_m}{\Delta H_m^o} \times 100 \qquad \text{(Equation 5.2)}$$

Optical microscopy with the crossed polarizers, the axis of the analyzer at 90° with respect to the axis of the polarizer, was also employed to examine the spherulitic morphology/structure. An Olympus BX-41 microscope equipped with a SPOT Insight QE camera and outfitted with a liquid nitrogen cooled Linkam LTS 350 hot stage, used to crystallize thin sections isothermally for 30 minutes following controlled cooling from

the melt. The samples were annealed above the melt temperature of PET at 280 °C for 3 minutes, to allow for complete melting, followed by fast cooling (25 °C per minute) to the crystallization temperature (237 °C for bulk PET, and 227 °C for PET/PC blends). It is important to note that no glass cover slips were used in this work, as this has been found to influence the spherulite growth behaviors.[17] Phase coalescence in the blends was monitored by color inversion of the PLOM images, such that crystallizable regions were now dark blue and the amorphous regions are light blue, rather than by running conventional optical microscopy coupled with subsequent PLOM experiments.

5.4   Results and Discussion

5.4.1   Mechanical Behaviors

Dynamic mechanical analysis was utilized to examine the thermomechanical behaviors of the bulk polymers and the PET and PC blends. Initially we focus on the storage modulus (G') as a function of temperature (see **Figure 5.2**). Since G' is a good indicator of the elastic modulus, we expect – and find – a good correlation between the T_g of the PET and PC phases and the decline in modulus anticipated at the transition between the glassy and rubbery region. We expect and observe a distinct trend with respect to the storage modulus as a function of temperature and blend concentration. When the PET transitions to its rubbery state (just above 80 °C) the storage modulus decreases with increasing PET fraction in the PET/PC blends. A sharp rise in the G' of the bulk PET is noted at 130 °C, associated with cold crystallization of the PET. As was

observed in the PET and PET/mmt nanocomposites (see **Chapter 3**), injection molding

led to a low degree of crystallinity as a result of the near quenching mold temperature

(ambient conditions 25 °C).

Figure **5.2**
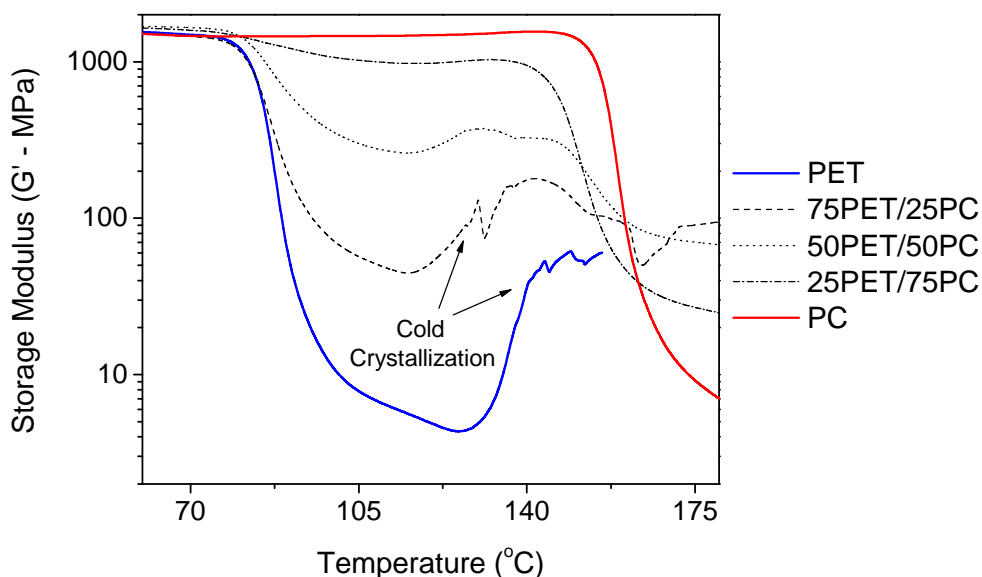
Figure **5.2**: Storage modulus (G'), an indicator of the elastic modulus, of PET, PC, and the PET/PC blends as a function of temperature.

Simple visual observations of the DMA specimens confirmed the cold

crystallization, as the bulk PET was transparent prior to DMA analysis and opaque after

the completion of the temperature sweep, with similar increases in opacity occurring for

the PET/PC blends.

When we examine the peak tan delta behaviors, a good indicator of the apparent

glass transition temperature, the data indicates that two separate and distinct T_g's are

present for all blend compositions, independent of blend concentration (see **Figure 5.3**).

The third peak, as discussed previously, is attributed to cold crystallization of the PET phase in the blend. Thus, the absence of a distinct peak shift from blend to blend suggests that no extensive transesterification takes place (see **Table 5.3**). This is not surprising as the literature asserts that transesterification reactions are limited in the absence of catalyst and would require melt-blending times that are far longer than what was employed here (greater than 60 minutes for the temperature employed here). [**3**][**5**]

Figure **5.3**
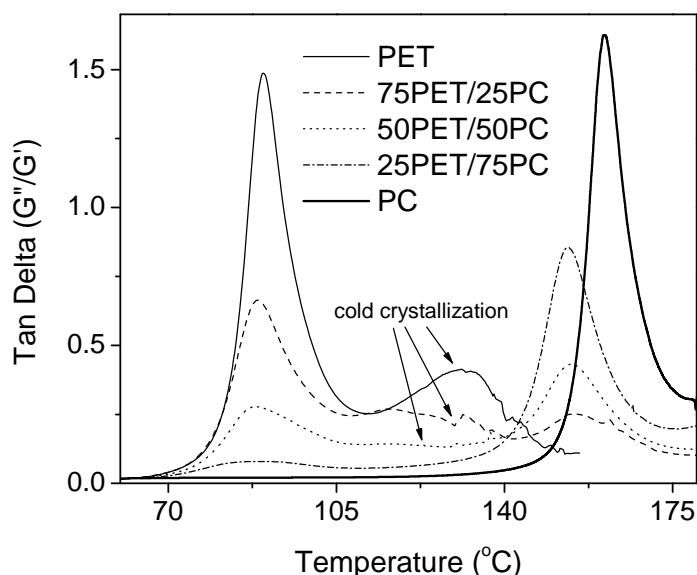
Figure **5.3**: Mechanical loss factor (apparent glass transition) behavior of the bulk PET and PC and the PET/PC blends. A pronounced cold crystallization peak is also noted.

The mechanical properties via tensile testing of the PET/PC blends have been well-studied in the literature and are presented here only to illustrate the effects of blend formation on modulus and the elongation-at-break (see **Table 5.3**). We note that the measured mechanical properties here are in good agreement with the literature.

Table **5.2**

Table **5.2**: Instron analysis of the bulk polymers (PET and PC) and the PET/PC blends.

| | **Instron** | | **DMA** | |
Φ_{PET}	Tensile Modulus [MPa]	Elongation at Break (%)	PET T_g[a] (^oC)	PC T_g[a] (^oC)
0	1600 ($\pm$ 30)	110 ($\pm$ 7)	-	161
0.25	1590 ($\pm$ 20)	117 ($\pm$ 3)	89	154
0.50	1610 ($\pm$ 30)	150 ($\pm$ 5)	88	154
0.75	1600 ($\pm$ 20)	233 ($\pm$ 8)	89	155
1	1550 ($\pm$ 50)	230 ($\pm$ 16)	90	-

[a] as measured by DMA from the peak tan delta (G"/G')

5.4.2   Transesterification Analysis

High ratios of copolymer formation via transesterification reactions between PET and PC have been shown to lead to the development of a single T_g [**5**][**7**] that is readily predicted by the Fox [**18**] equation (**see Equation 5.3**) where the copolymer or miscible blend T_g is calculated from the weighted average of the glass transition temperature of the two polymers (in this case T_g^{PET} and T_g^{PC}) where W_{PET} and W_{PC} are the corresponding weight fractions.

Equation **5.3**

$$\frac{1}{T_g} = \frac{W_{PET}}{T_g^{PET}} + \frac{W_{PC}}{T_g^{PC}}$$ (Equation **5.3**)

The T_g behavior of the blends was investigated by MDSC. MDSC can separate the reversible and non-reversible transitions, such that the thermodynamic and kinetic

events are easily distinguished. We again observe no distinct deviations in the PET or PC T_g as the blend concentration varies (see **Figure 5.4**), a result that confirms the findings of the DMA. Most importantly, the T_g behavior does not follow the Fox prediction for copolymer/miscible blend formation.

Figure **5.4**
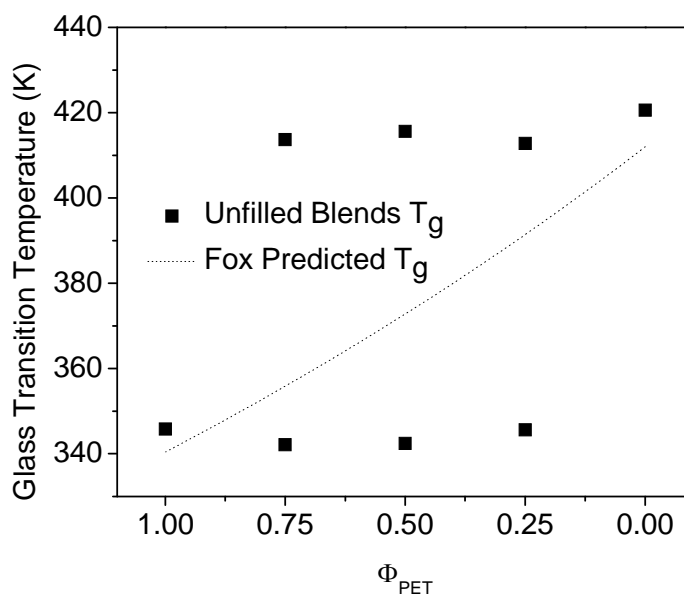
Figure **5.4**: MDSC analysis of the PET and PC glass transition temperatures compared to the Fox-Flory copolymer relation.

Transesterification was also monitored via ATR-FTIR (see **Figure 5.5**). When copolymer formation occurs the PC peak (1780 cm^{-1}) decreases in intensity while the PET peak (1720 cm^{-1}) increases in intensity and a new peak develops at the 1740 cm^{-1} band associated with the stretching of a mixed aliphatic-aromatic carbonate, which is a product of the ester-carbonate transesterification reaction.
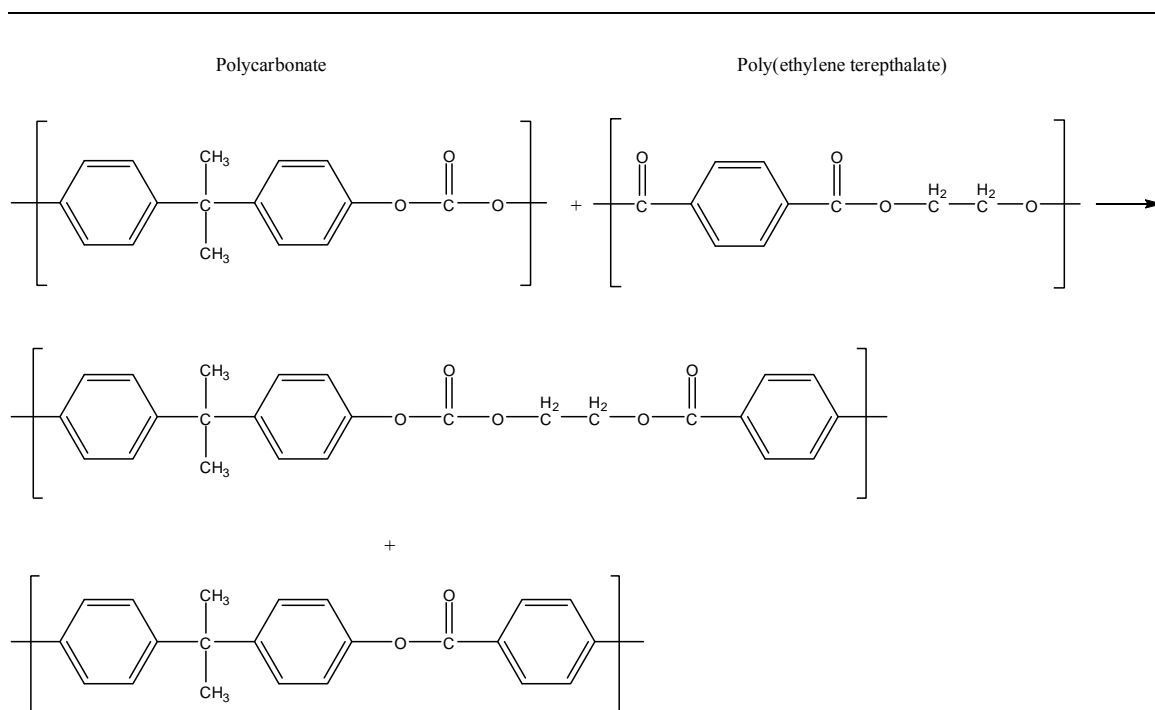
Figure **5.5**
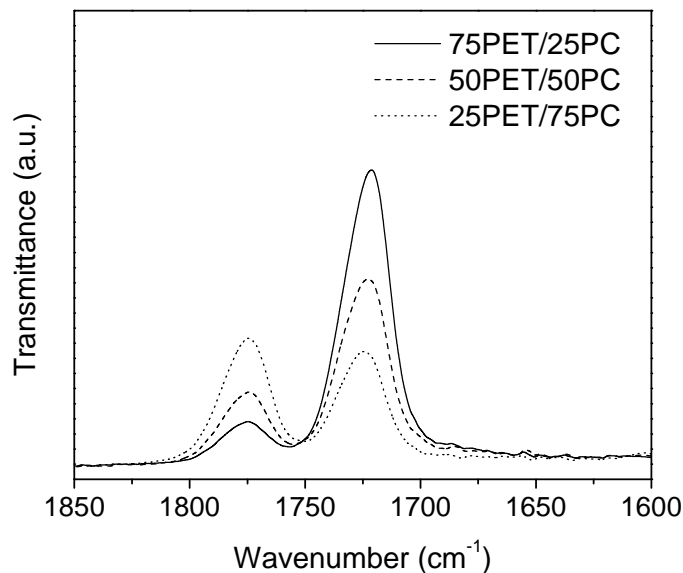
Figure **5.5**: ATR-FTIR comparison of the as-molded PET/PC blends.

Here we examine the data obtained from the as-molded specimens and find that no peak-splitting has occurred. Solution IR was also done on these samples and no distinct deviations were observed (data not shown here). The difficulty in using IR, or for that matter ATR-FTIR, is the fact that low levels of transesterification are undetectable. Relative comparisons are difficult from this limited data, thus when combining the T_g data from the DMA and MDSC experiments, we may come to the conclusion that no significant amount of copolymer formation has occurred during melt-blending. This conclusion is consistent with literature, in which forced transesterification by catalyst addition was avoided.[**19**] Further verification regarding the extent of copolymer formation may be inferred from DSC studies examining the overall degree of PET crystallinity: If there are no sharp declines in crystallinity, transesterification reactions are limited.

5.4.3 PET/PC Blends Crystallization

The general crystallization behaviors of the PET/PC blends were examined through DSC studies. To aid comparison, the as-molded and annealed samples were examined side-by-side (see **Figure 5.6**). The distinct cold crystallization peak (T_{cc}) observed in the DMA was present in all blend concentrations and the bulk PET itself, when examining the as-molded samples, indicating a low-degree of crystallinity developed during melt-blending.

Figure **5.6**
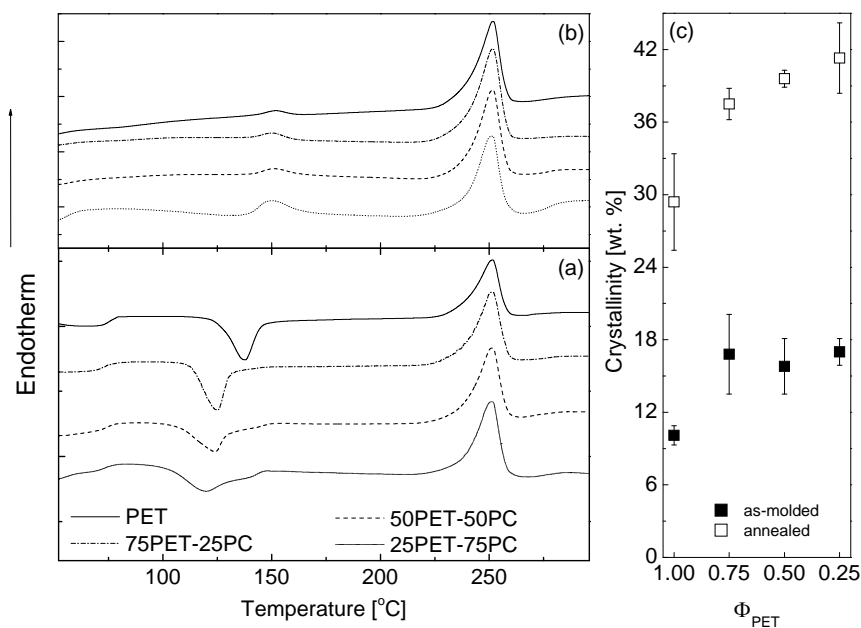
Figure **5.6**: DSC scans normalized by the weight fraction of PET for the: (a) as-molded samples, (b) annealed samples for 1.5 hours at 140 °C, and (c) the crystalline fraction.

Mirroring the PET/mmt nanocomposite behavior (where the inorganic fillers act as nucleating agents), the peak T_{cc} of the blends shifted from 138 °C in the bulk PET to 125 °C in the 75PET/25PC blend and continued to decline with increasing amorphous PC

fraction (peak $T_{cc\ 25PET/75PC}$ at 119 °C). Annealing at 140 °C for 1.5 hours is sufficient in driving the crystallization process to near completion (**Figure 5.6b**), indicated by the cold crystallization peak disappearance. The overall crystallinity of the blends, when normalized by the fraction of crystallizable PET, shows no distinct difference regardless of the amorphous and non-crystallizable PC fraction.

PLOM was employed to examine the spherulitic structure of PET and its blends. Prior to crystallization occurring while held isothermally, unique domain reorganization was observed in the PET/PC blends. Such phase behavior is not normally observed under cross-polarizers, yet in this work simple image analysis techniques (namely, color inversion coupled with adjustments to the contrast and brightness) have been utilized such that domain reorganization and the phase boundaries of the distinct two phase system can be observed by topographical differences. It is important to note that when examining subsequent images regarding phase behavior and crystallization, color inversion is used exclusively to view the phase behavior and spherulitic growth at the PET/PC interface when PLOM images can not resolve phase contrast. This approach shows the spherulites to be the dark features, whereas the light features denote amorphous PC.

Initial examination of the blend morphology and phase coalescence allows confirmation of the phase continuity predictions, indicating the PET as the continuous phase. Second, we clearly observe static phase coalescence, the process in which two particles of the same phase merge: Prior to nucleation and growth, the PET and PC domains reorganize, such that larger PET domains develop (**Figure 5.7**).

Figure **5.7**
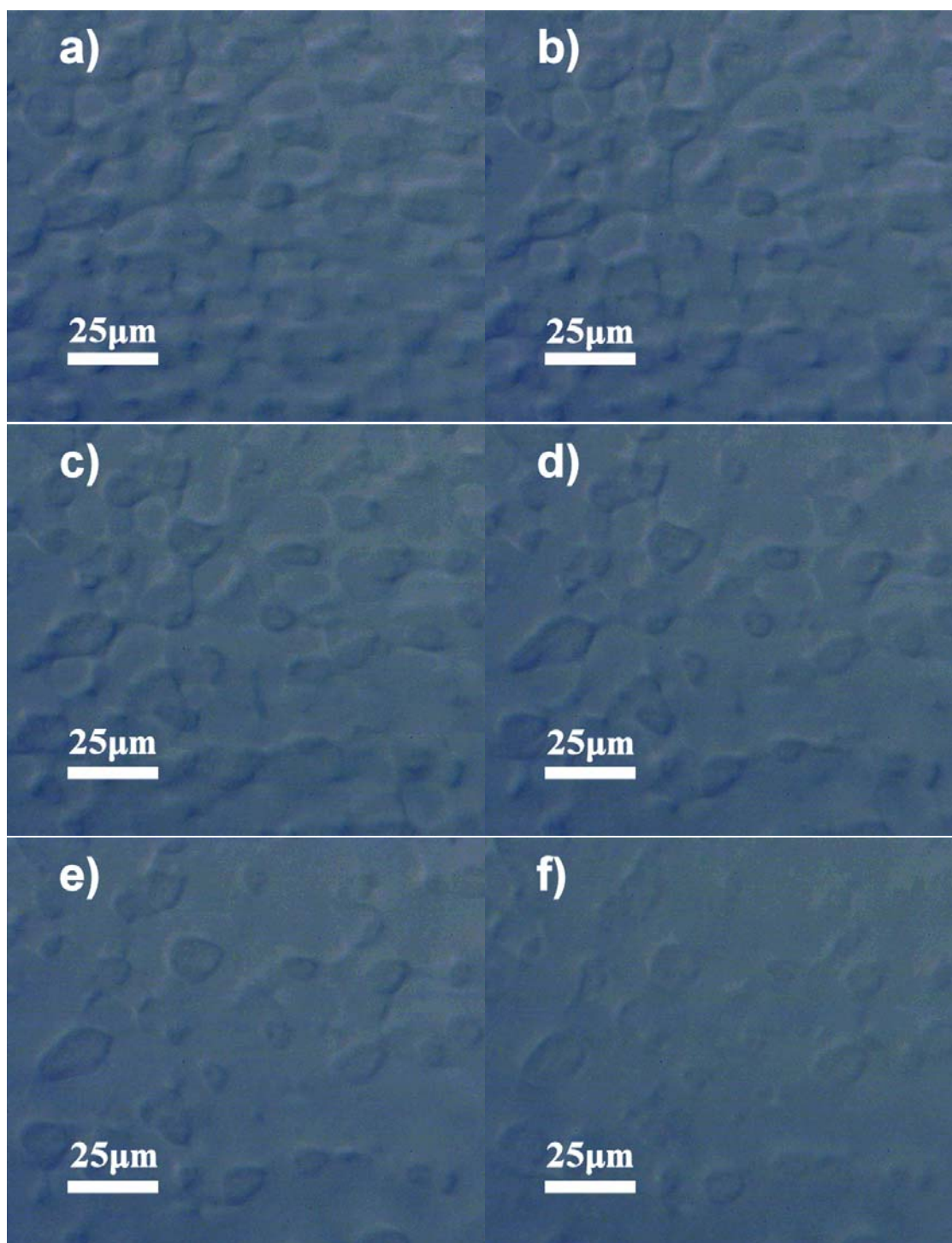
Figure **5.7**: Phase coalescence of the 75PET/25PC during isothermal crystallization at 227 °C: a) 1 minute, b) 3 minutes, c) 5 minutes, d) 7 minutes, e) 9 minutes, f) 11 minutes.

This series of images is a time progression in which **image a** corresponds to 1 minute of isothermal crystallization, **image b** is 3 minutes, **image c** is 5 minutes and so on. A high degree of disruption in the phase continuity is present at the outset (**Figure 5.7a**), but just prior to nucleation and growth the more mobile PET phase has reorganized such that larger PET domains exist (**Figure 5.7f**). Once this distinct phase coalescence has completed, nucleation and spherulite growth commences (see **Figure 5.8**).

Figure **5.8**
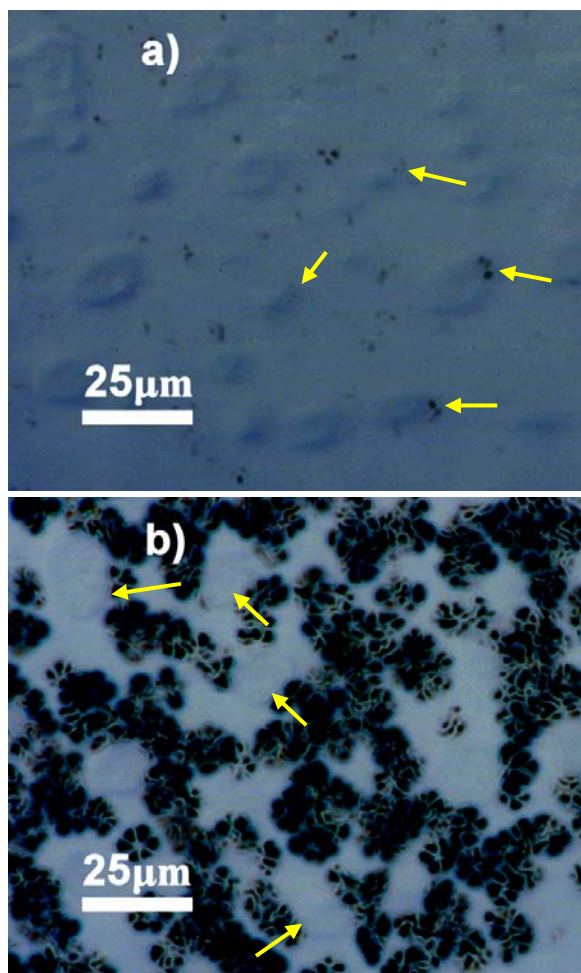
Figure **5.8**: Inverted PLOM micrographs of the 75PET/25PC blend at: a) where nucleation occurs at the PET/PC interface and in the PET domains at $T_{iso} = 14$ min., and b) spherulite growth termination and impingement occurs at the interface at $T_{iso} = 30$ min.

Spherulite nucleation and growth begins shortly after phase coalescence completes. Nucleation occurred (**Figure 5.8a**) after about 14 minutes of isothermal crystallization at 227 °C. Some irregular spherulites were developed as a result of nucleation at the interfaces, with outward growth away from the amorphous inclusion. The PC domains were also observed to serve as spherulite growth termination surfaces (**Figure 5.8b**), where abnormal spherulite shapes can be seen as a result of growth into and subsequent termination of the spherulites at the PET/PC interface.

PLOM imaging was utilized to examine the size and shape of the PET spherulites under similar conditions (*cf*. **Chapter 3**). Bulk PET crystallized quickly at 237 °C with nucleation occurring in just one minute with initial impingement occurring shortly thereafter. The impinged structure after 30 minutes of isothermal crystallization is observed in **Figure 5.9** with the spherulite size of PET being 24 ± 2 micrometers just prior to complete impingement.

Figure **5.9**
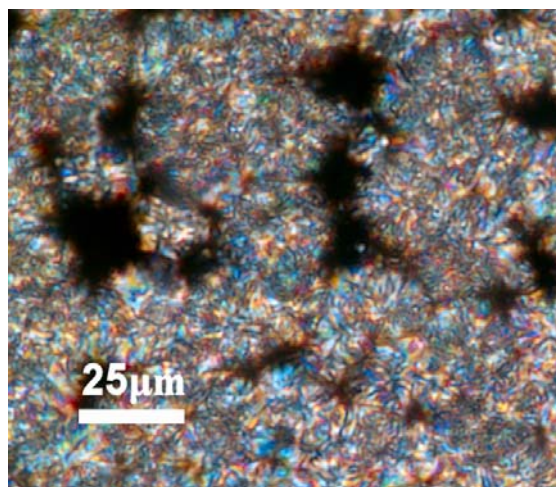
Figure **5.9**: PLOM image of PET isothermally crystallized for 30 minutes at 237 °C.

The PET/PC blends were examined from a spherulitic structure standpoint via PLOM at an isothermal crystallization temperature of 227 °C, a 10 °C lower than the bulk PET (see **Figure 5.10**). Upon examination after 30 minutes of isothermal crystallization, we find as the amorphous content of the blends increases a significant reduction in spherulite size is observed. PLOM imaging indicates the 75PET/25PC blends have a spherulite size of 11 ± 2 micrometers whereas the 50PET/50PC blend has spherulites with a size of just 9 ± 1 micrometers. The 25PET/75PC blend is inhibited in nuclei formation and growth such that after 30 minutes, the growth of normal spherulites was not possible. The immature spherulite size was found to be about 2 ± 0 micrometers and to better illustrate such immature spherulites, image inversion was applied such that the spherulites became black and the amorphous fraction is again light colored (fig. **5.10**c).

Figure **5.10**
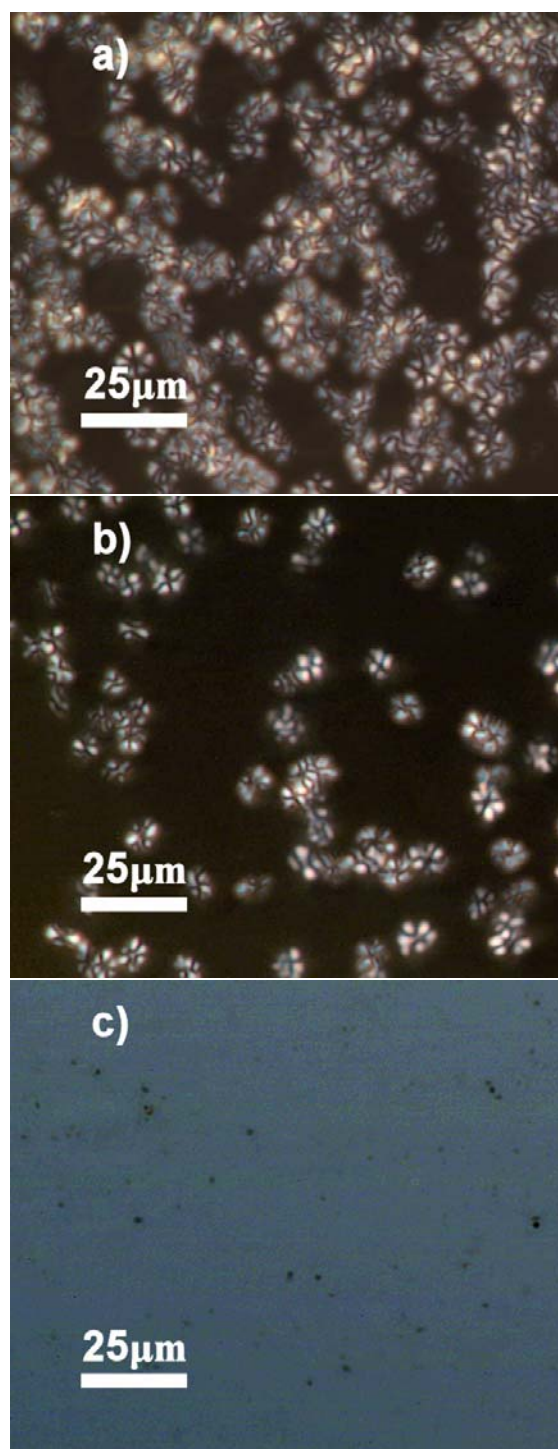
Figure **5.10**: PLOM images of PET/PC blends isothermally crystallized for 30 minutes at 227 °C: a) 75PET/25PC, b) 50PET/50PC, and c) inverted 25PET/75PC.

5.5 Conclusions

Blends of PET and PC were produced via melt-blending. Two distinct glass transition temperatures were observed via DMA and MDSC, which do not follow the Fox relation for predicting the T_g of a miscible blend or copolymer. Transesterification was not observed within the limits of the ATR-FTIR either, further substantiating the conclusion that there is no substantial copolymer formation. Thus, we conclude, although some amount of transesterification is inevitable it was limited to minimal levels, below the detectable levels of the instruments.

Crystallization was also studied for the PET/PC blends. Injection molding (with the mold held at ambient temperatures) led to a low degree of crystallinity and promoting cold crystallization upon heating. The overall crystallinity was not markedly impeded by the amorphous PC content. Unique phase coalescence was observed to occur in the blends prior to crystal nucleation. During the subsequent growth of the PET spherulites, amorphous PC domains acted as spherulite nucleation and growth termination points, leading to a reduction in the spherulite size.

References

1.   Robeson, L.M., *Polymer Engineering and Science* 1984; 24:587–597.

2.   Utracki, L.A. **Polymer Blends Handbook.** Kluwer Academic Publishers, Boston, MA, 2002.

3.   Suzuki, T., Tanaka, H., and Nishi, T., *Polymer* 1989; 30:1287–1297.

4.   Tan, Q. and Ma, D.Z., *Journal of Applied Polymer Science* 1993; 48:747–749.

5.   Marchese, P., Celli, A., and Fiorini, M., *Macromolecular Chemistry and Physics* 2002; 203:695–704.

6.   Reinsch, V.E. and Rebenfeld, L., *Journal of Applied Polymer Science* 1996; 59:1913–1927.

7.   Denchev, Z., Sarkissova, M., Radusch, H-J., Luepke, T., and Fakirov, S., *Macromolecular Chemistry and Physics* 1998; 199:215–221.

8.   Zheng, W-g., Wan, Z-h., Qi, Z-n, and Wang, F-s., *Polymer International* 1994; 34:301–306.

9.   Godard, P., Dekoninck, J.M., Devlesaver, V., and Devaux, J., *Journal of Polymer Science: Part A: Polymer Chemistry* 1986; 24:3315–3324.

10.   Molinuevo, C.H., Mendez, G.A., and Muller, A.J., *Journal of Applied Polymer Science* 1998; 70:1725–1735.

11.   Kong, Y. and Hay, N., *Journal of Polymer Science: Part B: Polymer Physics* 2004; 42:2129–2136

12.   Garcia, M., Eguiazabal, J.I., and Nazabal, J., *Journal of Applied Polymer Science* 2001; 81:121–127.

13.   Jordhamo, G.M., Manson, J.A., and Sperling, L.H., *Polymer Engineering and Science* 1986; 26:517–524.

14.   Lyu, S-P., Bates, F.S., and Macosko, C.W., *AIChE* 2000; 46:229–238.

15.   Porter, R.S., and Wang, L-H., *Polymer* 1992; 33:2019–2030.

16.   Wunderlich, B., **Macromolecular Physics, Vol. 1, Crystal Structure, Morphology, Defects**, Academic Press, New York, NY, 1973.

17.   Schultz, J.M., **Polymer Crystallization**, Oxford University Press, New York 2001.

18.   Fox, T.G., *Bulletin of the American Physical Society* 1956; 1:123.

19.   Murff, S.R., Barlow, J.W., and Paul, D.R., *Journal of Applied Polymer Science* 1984; 29:3231–3240.

<center>**Chapter 6**</center>

Design of Selective Montmorillonite Phase Dispersion and Compatibilized Poly(ethylene terephthalate) / Polycarbonate / Montmorillonite Nanocomposite Blends

6.1   Summary

The thermodynamics of dispersion governing polymer/layered silicate nanocomposites were tested and confirmed. Novel poly(ethylene terephthalate)/Polycarbonate/montmorillonite nanocomposite blends were melt-blended and by tailoring the surfactant chemistry, the dispersion and phase morphology of the resultant nanocomposites were able to be controlled. The use of melt-blending techniques such as masterbatching to overcome the strength of the thermodynamic driving force in an attempt to control the dispersive phase of the layered silicate was unsuccessful. Depending on the subsequent phase morphology developed in the melt-blending process, some of these novel nanocomposite blends displayed a remarkable improvement in ductility over the unfilled blend, proving to be superior materials from a structural standpoint and likewise warrant further investigation for their applicability to industrial applications.

6.2   Introduction

Polymer blends, in particular PET/PC blends, have been well studied with regards to blend miscibility, structure, crystallization, degradation (transesterification) and the resultant materials properties.[1][2][3] Polymer nanocomposites derive much of their interest from the remarkable concurrent improvements that have been observed at low filler loading levels (< 5 wt. % inorganic) in mechanical properties, flammability characteristics, thermal resistance, barrier properties, and crystalizability.[4][5][6][7] The addition of a nano-filler such as montmorillonite to PET/PC blends is of interest from an industrial and scientific standpoint as such nanocomposite blends could have applicability to a wide-variety of applications and are considered to be novel materials.

The morphological behaviors observed in this study can best be broken down into two distinct categories: 1) 'non-compatibilized' and 2) 'compatibilized'. The non-compatibilized systems are best described as phase separated on the micron and sub-micron scale, with distinct domains of each polymer present without significant boundary overlap. Remarkably, the layered silicate remains selectively dispersed in only one phase. The montmorillonite platelets are present at the boundary between the two phases; however, their presence outside this layer is absent. The compatibilized morphology is used to describe the phase behavior of such blends alone, and is not an accurate indicator of the resultant material properties in the sense that the individual properties which make each polymer matrix unique are still present on the macro scale. However, we find the phases to be compatibilized such that micron and even in most cases sub-micron detection of the distinct phases is not readily apparent. Thus, we, although partially

inaccurate, refer to such morphologies as compatibilized only in the sense of the phase behavior for both 'non-compatibilized' and 'compatibilized' nanocomposites.

Commercially available organo-montmorillonites (o-mmt) are typically modified with quaternary ammonium based surfactants in order to promote miscibility with organic materials (solvents, polymer, paints, etc.). Despite the favorable thermodynamics of mixing, alkyl ammonium modified mmt's have surfactant degradation temperatures below 260 °C in oxidizing environments (air) presenting a substantial challenge when attempting to melt-blend high melt-processing temperature polymers such as PET and PC in their presence.[8] Thermal degradation of such alkyl-ammonium surfactants occurs in both PET/mmt [9][10] and PC/mmt [11][12] nanocomposites leading to matrix molecular weight degradation. Likewise, the melt-blending temperature of PET/PC blends is also above the degradation temperature of alkyl-ammonium surfactants, leading to the promotion of molecular weight degradation of the host matrices.

Thus, both hybrid systems and the blends themselves could benefit from the introduction of a thermally stable o-mmt. Previous studies from this end have shown that high temperature surfactants such as an alkyl-imidazole are thermally stable in the range of and above the PET and PC processing temperatures.[13][14] In principle, an alkyl-imidazole surfactant could reduce the extent of degradation during melt-blending while offering comparable yet varied thermodynamics of mixing to the alkyl-ammoniums, bearing promise for these nanocomposites and warranting further consideration.

The opportunity to modify one of the two polymers, if selective dispersion of the filler can be achieved in one of the two phases only, is presented especially since in the absence of transesterification reactions PET/PC blends are immiscible (see

Chapter 5).[15] Transesterification between PET and PC is regarded as an ester-carbonate exchange reaction and takes place in the molten phase and the reaction is catalyzed by the presence of residual catalysts from the polymerization process.[1][15][16] When the transesterification reaction continues to completion the two distinct glass transition temperatures of the mechanical blend of PET and PC merge according to the Fox relation and the crystallization and melting behaviors of the PET are generally absent.[17] As one would expect, the degree of transesterification has been found to be highest in 50PET/50PC blends, although the rate of transesterification is greatest in PC rich blends.[18] There is no reason to believe the presence of mmt or surfactant chemistries utilized in this work will promote transesterification reactions in the PET/PC nanocomposite blends.

In this study we designed and prepared novel PET/PC/mmt nanocomposites by the melt-blending process. Our objectives are to (1) design and test appropriate organic modification for montmorillonite in these novel nanocomposites and elucidate the subsequent phase morphology and dispersive behaviors of such PET/PC/o-mmt nanocomposite blends, and (2) determine the mechanical properties of the resulting nanocomposites, connecting – if possible – to the polymer and composite morphologies.

6.3   Experimental

6.3.1   Materials

The polymers used in this study were donated by BAYER MaterialScience. The PET was Voridian 12822 which is a high molecular weight (M_n = 35 kg mol^{-1}) high intrinsic viscosity (IV = 0.95 dl/g) grade. The PC was a standard high molecular weight high viscosity (M_n = 32 kg mol^{-1}) PC resin, Makrolon 3208 in powder form. Commercially available organo-mmt, Cloisite 25A (C25A), with a cation-exchange capacity (CEC) of 0.95 meq/gram and a dimethyl hydrogenated tallow 2-ethylhexyl quaternary ammonium surfactant was used as received from Southern Clay Products. The high-thermal stability alkyl-imidazole modified mmt (imm-mmt) was synthesized for this work and the corresponding ion exchange process was detailed in **Chapter 3**.

6.3.2   Nanocomposite Preparation by Melt-Blending

All nanocomposites systems were extruded on a Prism TSE 16TC twin-screw extruder with an L/D ratio of 16 run at 280 to 330RPM. The polymers and mmt were dried at 100 °C overnight and were tumbled for 20 minutes prior to extrusion at 280 °C. Subsequent injection molding of the extruded samples into micro-flexural and tensile bars took place on a BOY 22D machine operated at a melt temperature of 295 °C with the mold at ambient conditions (see **Appendix 6.6.2** for full operating parameters). Unfilled PET/PC blends and the corresponding nanocomposites utilizing the two different mmt surfactant chemistries were produced with PET/PC ratios of: a)

75PET/25PC, b) 50PET/50PC, and c) 25PET/75PC. All nanocomposites studied within this work contained 3 wt. % inorganic mmt.

6.3.3   Dispersion Analysis

Wide angle x-ray diffraction (XRD) and complementary transmission electron microscopy (TEM) were utilized to examine the dispersion characteristics of the nanocomposites. The XRD was completed on a Rigaku powder diffractometer with Cu K_α tube source (λ = 1.5404 Å), scanning from 1.5 ° to 8 ° at a continuous scan rate of 0.6 degrees per minute. The generator tension was 50 kV and the current was 20 mA. Complementary TEM images of the nanocomposites were obtained with a JEOL 1200 EXII microscope operated with an accelerating voltage of 80 kV, and equipped with a Tietz F224 digital camera. Ultra thin sections (70 to 100 nm) of the nanocomposites were obtained with an ultramicrotome (Leica Ultracut UCT) equipped with a diamond knife. The sections were transferred to carbon-coated copper grids (200-mesh). No heavy metal staining of the sections prior to imaging was necessary since the contrast between the layered silicate and the polymer matrix was sufficient to observe the filler dispersion.

6.3.4   Mechanical Properties and Transesterification Analysis

The tensile properties of the bulk PET and its nanocomposites were measured by tensile testing on the injection molded micro-tensile bars. The tensile bars (dogbones) are ASTM D638 standard type IV specimen with a molded thickness of approximately

3.18 mm. The tensile tester, an Instron 5866 tensile tester, was operated with a crosshead speed of 50.8 mm/min. The Young's modulus (E) and elongation-at-break will be reported as per the calculations from the Instron software. The elongation at break is reported from the crosshead travel as strain extensometers with sufficient travel were unavailable. It is also important to note the tensile behaviors were measured on the as-molded tensile bars with no post-molding annealing.

The copolymer formation was monitored by attenuated total reflectance Fourier spectroscopy (ATR-FTIR) using a Digilab FTS 800 instrument. Injection molded micro-flexural bars were analyzed with 64 scans at a resolution of 2 cm^{-1} with three separate scans of each specimen being averaged prior to comparative analysis. When examining transesterification via infrared spectroscopy (IR), three distinct bands are of particular interest: (1) the 1775 cm^{-1} band that corresponds to the carbonyl stretching of an amorphous aromatic carbonate (PC), (2) the 1720 cm^{-1} band associated with the carbonyl stretching of an aliphatic ester (PET), and (3) the 1740 cm^{-1} band associated with the stretching of a mixed aliphatic-aromatic carbonate, which is a product of the ester-carbonate transesterification reaction (see **Chapter 5**).[18][19] Complementary Raman Spectroscopy was utilized to confirm the results of the ATR-FTIR; it is important to note the same laser was used such that the shifts in each sample were equivalent.

Transesterification was also monitored via the glass transition temperature (T$_g$) shifts of both phases using modulated differential scanning calorimetry (MDSC). The instrument was a TA Instruments Q100 DSC calibrated with sapphire and indium standards run under a helium purge with a secondary nitrogen purge. A conventional MDSC experiment was run in order to acquire the T$_g$'s of both polymers. Data was

collected from a ramp rate of 3 °C per minute with a modulation of 1 °C every 60 seconds. The reversing heat capacity shall be used to resolve the T_g's in order to better define the thermodynamic T_g effects. We shall define the T_g as being the midpoint of the step change in the heat capacity.

6.4   Results and Discussion

6.4.1   Validation of the Thermodynamics of Dispersion (PET/mmt and PC/mmt)

PET/mmt and PC/mmt nanocomposites were examined to determine the miscibility of the base polymers of the study with the two mmt surfactant treatments alone. The driving force of dispersion was discussed in detail in **Chapter 2** of this thesis. A cursory review reminds us that dispersion of a filler (s) modified with a surfactant (s) attempted to be dispersed within a polymer matrix (p) is dependent upon the development of sufficient favorable excess enthalpic interactions – *e.g.* when the polymer/filler interactions are greater than corresponding surfactant/filler interactions, nano-scale dispersion will be achieved (see **Equation 6.1**).[20][21] The dispersion can be predicted following the van Oss-Chaudhury-Good formalization of surface tensions [**22**] as modified by Vaia to be applied to polymer/organo-clay mixing (see **Equation 6.2**) where γ^{LW} is the Lifschitz-van der Waals component to the surface tension, γ^{AB} is the acid-base component, γ^{+} is the electron acceptor and γ^{-} is the electron donor parameter of the polar component (γ^{AB}).

Equation **6.1**

$$\gamma_{excess}^{total} = \gamma_{ps} - \gamma_{as}$$ (Equation **6.1**)

Equation **6.2**

$$\gamma_{ij} = \gamma_{ij}^{LW} + \gamma_{ij}^{AB} \quad \text{with} \quad \begin{vmatrix} \gamma_{ij}^{LW} = \left(\sqrt{\gamma_i^{LW}} - \sqrt{\gamma_j^{LW}}\right)^2 \\ \gamma_{ij}^{AB} = 2\left(\sqrt{\gamma_i^+} - \sqrt{\gamma_j^+}\right)\left(\sqrt{\gamma_i^-} - \sqrt{\gamma_j^-}\right) \end{vmatrix}$$ (Equation **6.2**)

From a theoretical standpoint, based on **Equations 6.1** and **6.2,** and the surface tensions of the individual components (see **Table 6.1**); favorable dispersion of a simple alkane-modified montmorillonite is predicted to occur within both the PET and PC matrices upon melt-blending. It is important to note that this analysis ignores the contribution of the ammonium/imidazolium ion to the surface tension. This omission will receive further attention in the context of the prediction of the dispersive phase of the nanocomposite blends.

Table **6.1**

Table **6.1**: Surface tension components of PET [**23**], PC [**24**][**25**], montmorillonite [**21**], and surfactant treatments [**26**]

	γ^{LW} (mJ/m^2)	γ^+ (mJ/m^2)	γ^- (mJ/m^2)	Reference
PC	38.6	0.20	1.3	24,25
PET	43.5	0.01	6.8	23
Montmorillonite	66	0.70	36	21
Hexadecane	26	0	0	26

The surface tension components of the PC were calculated based on contact angles from the literature using the well-established Young-Dupre relation (see

Equations 6.3) where θ is the contact angle of a liquid (subscript *L*) on a solid (subscript

S), where γ^{LW} is the Lifschitz-van der Waals component to the surface tension, γ^+ is the

electron acceptor, and γ^- is the electron donor parameter of the polar

component (γ^{AB}).[22] If the contact angles of three liquids with known γ^{LW}, γ^+, and γ^- are

measured (two of which must be polar liquids) on the unknown solid – in this case PC –

Equation 6.3 can be used to determine the surface tension components by solving a

series of three equations with three unknowns.

Equation **6.3**

$$(1+\cos\theta)\gamma_L = 2(\sqrt{\gamma_s^{LW}\gamma_L^{LW}} + \sqrt{\gamma_s^+\gamma_L^-} + \sqrt{\gamma_s^-\gamma_L^+})$$ (Equation **6.3**)

These simple theoretical arguments were verified experimentally. The XRD trace

of the PET/mmt nanocomposites (see **Figure 6.1**) indicates an intercalated morphology.

The classic shift in the 2θ to lower values occurs after melt-blending the commercial mmt

(C25A) with the PET (**Figure 6.1a, b**). The imm-mmt has an expanded gallery at the

outset (**Figure 6.1c**), most likely from excess water/solvent, making it difficult to draw

concrete morphological conclusions from XRD alone as a slight gallery collapse occurs

from the swollen state upon nanocomposite formation.

Figure **6.1**
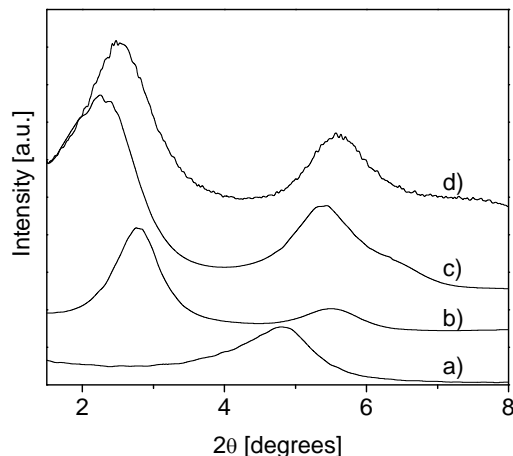
Figure **6.1**: XRD patterns of pure o-mmt and PET/o-mmt nanocomposites: a) C25A o-mmt, b) PET/3% mmt C25A nanocomposite, c) imm-mmt, and d) PET/3% imm-mmt nanocomposite.

Complementary TEM imaging corroborates the intercalated structure in the PET/C25A mmt nanocomposites and indicates a similar intercalated morphology is developed in the PET/imm-mmt nanocomposites despite the swollen gallery (see **Figure 6.2**). TEM also indicates the clay tactoids are well-dispersed throughout with no large agglomerations, and in the high magnification images (**Figure 6.2b, d**) we find individual mmt layers visible in the classic 'deck of cards' structure, substantiating the long-range order of the intercalated nanocomposite.

Figure **6.2**
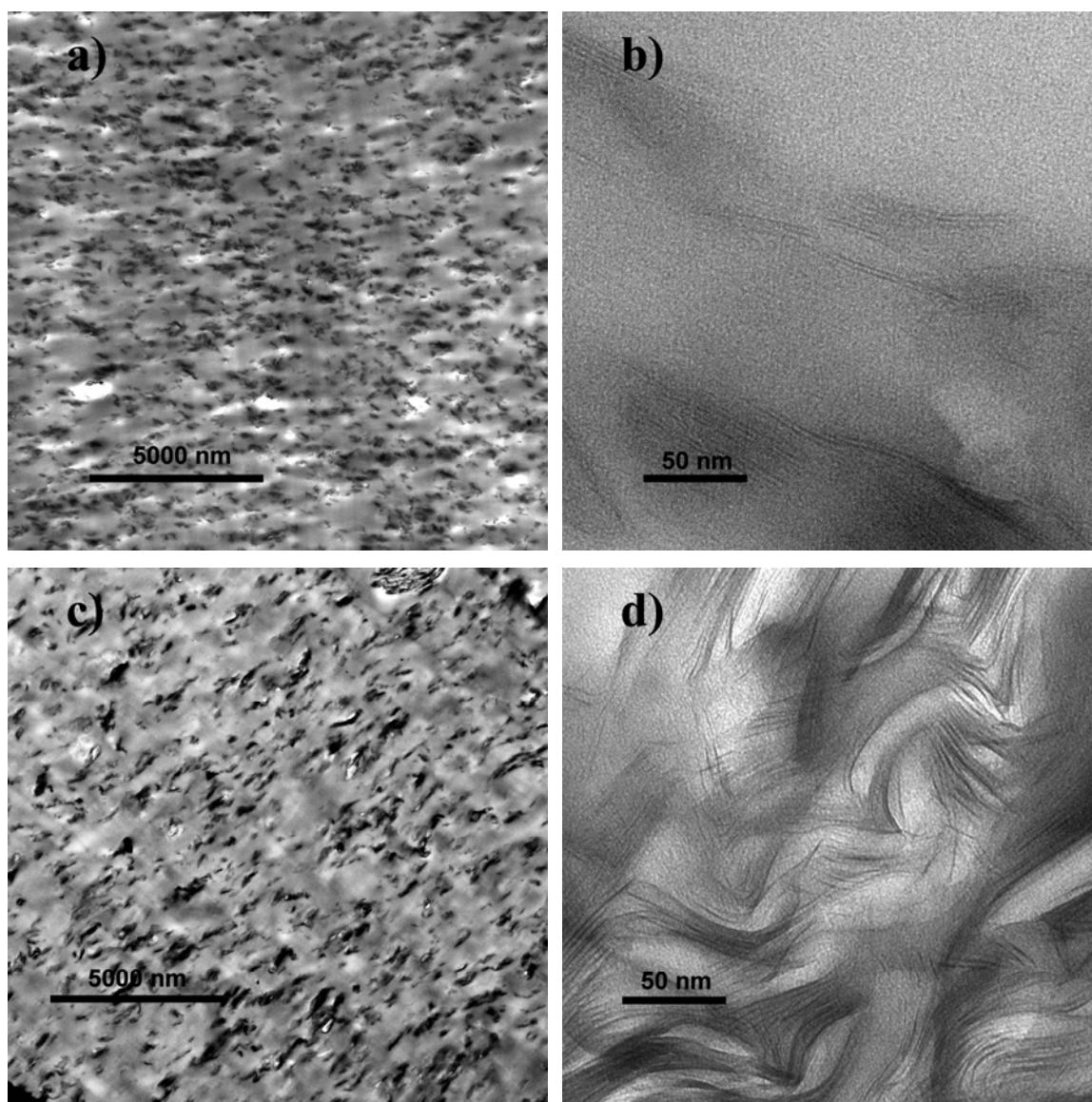
Figure **6.2**: TEM images of low and high magnification intercalated PET/mmt nanocomposites. a) low mag PET/C25A mmt, b) high mag PET/C25A mmt, c) low mag PET/imm-mmt and d) high mag PET/imm-mmt nanocomposites.

Similar intercalated morphologies were confirmed in the PC/mmt nanocomposites, again confirming the theoretical prediction of mmt dispersion within the PC matrix. The dispersed alkyl-ammonium modified C25A mmt (see **Figure 6.3**) and

swollen imm-mmt exhibit near identical behaviors in the PC nanocomposites as compared to the PET nanocomposites. The characteristic shift to lower values of 2θ occurs for the PC/C25A mmt nanocomposites and a slight decrease in the d-spacing again occurs for the PC/imm-mmt nanocomposite (**Figure 6.3**, **Table 6.2**).

Figure **6.3**
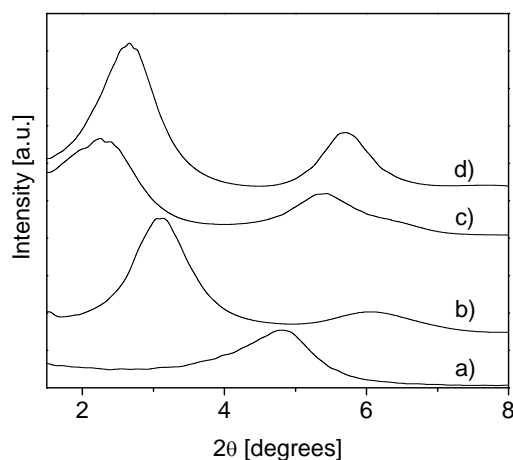
Figure **6.3**: XRD patterns of pure o-mmt and PC/o-mmt nanocomposites: a) C25A o-mmt, b) PC/3% mmt C25A nanocomposite, c) imm-mmt, and d) PC/3% imm-mmt nanocomposite.

TEM imaging verified the intercalated morphology (see **Figure 6.4**). The low magnification images show well-dispersed mmt tactoids without large agglomerations and the high magnifications again detail the well-ordered individual layers within the tactoid. One discernible difference was observed between the PET and PC nanocomposites; the average tactoid size observed in the PC nanocomposites was smaller than the corresponding PET nanocomposites. The reduction in tactoid size is rooted in the viscosity of the host matrix polymer. When exposed to near identical high shear rates

during melt-blending, the higher viscosity PC has greater viscous forces to aid in breaking apart the clay tactoids leading to size reduction.

Figure **6.4**
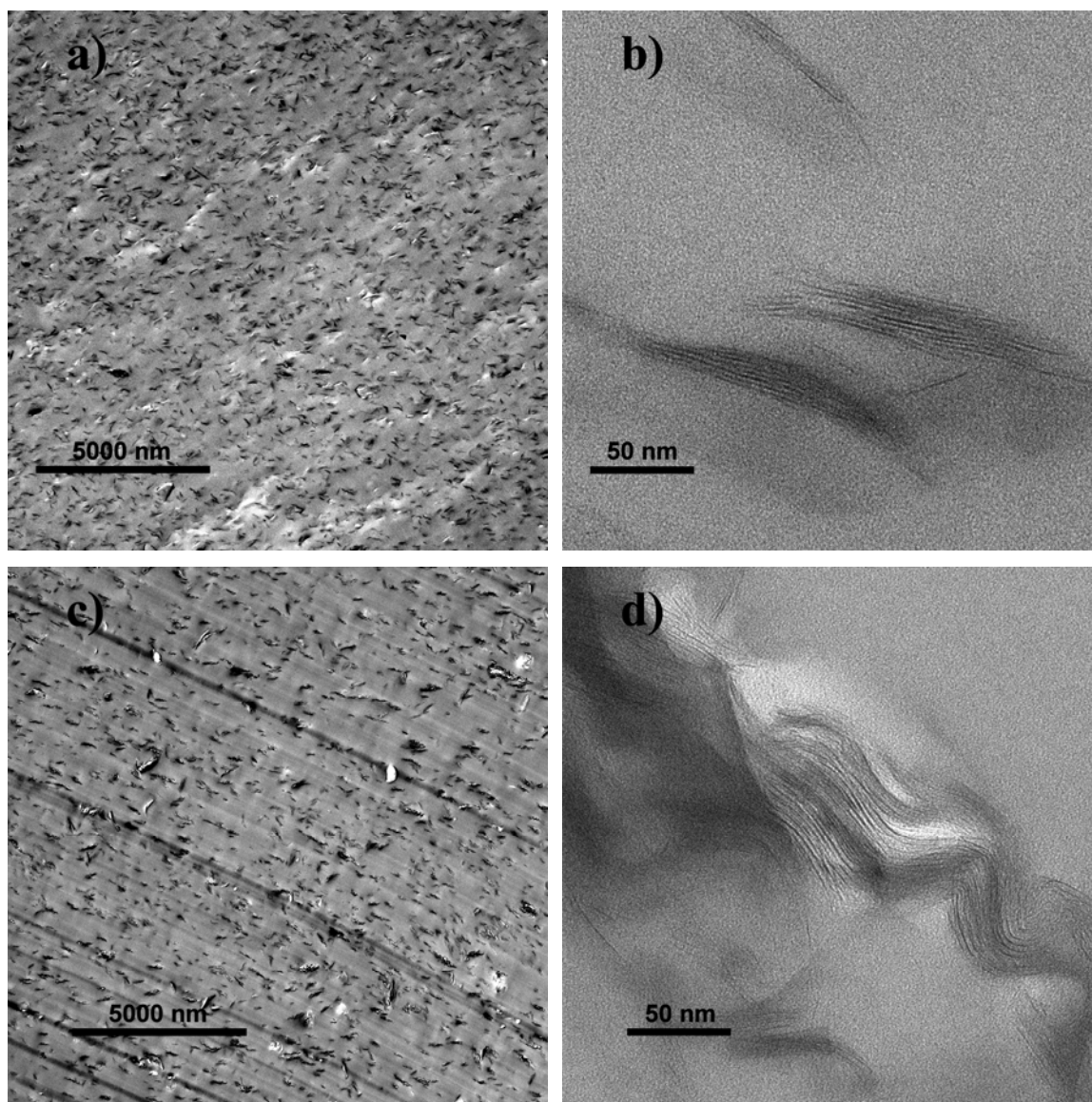
Figure **6.4**: TEM images of low and high magnification intercalated PC/mmt nanocomposites. a) low mag PC/C25A mmt, b) high mag PC/C25A mmt, c) low mag PC/imm-mmt and d) high mag PC/imm-mmt nanocomposites.

Thus, as proven from an experimental standpoint, the validity of the simple thermodynamic arguments defining polymer/organo-mmt dispersion is applicable for the polymers of interest in this work.

Table **6.2**

Table **6.2**: XRD d-spacing as determined by Bragg's law for the organo-mmt prior to and after nanocomposite formation with PET and PC.

	d-Spacing (nm)
C25A mmt	1.8
PET/3% mmt C25A	3.1
PC/3% mmt C25A	2.8
imm-mmt	3.7
PET/3% mmt imm-mmt	3.5
PC/3% mmt imm-mmt	3.5

6.4.2　Predictive Approach to Defining mmt Dispersion

Shifting to the nanocomposites based on PET/PC blends, the dispersion of the mmt should be encouraged from a thermodynamics standpoint in the matrix in which the favorable excess enthalpic interactions are greater. Thus, if we examine the excess enthalpic interactions for PET/alkyl-mmt and PC/alkyl-mmt from a comparative standpoint according to **Equations 6.1** and **6.2** based on the surface tensions of **Table 6.1**, we find that γ_{excess}^{total} PET is slightly greater than γ_{excess}^{total} PC. Now, if we consider the sheer number of such polymer/mmt contacts, the driving force for dispersion becomes much stronger in favor of dispersion within the PET matrix. Therefore, if considering for a moment the PET/PC/alkyl-modified mmt nanocomposite blends (which are very much

like the PET/PC/C25A mmt nanocomposite blends) from the thermodynamics of dispersion standpoint we might predict selective dispersion of the mmt within the PET phase if we ignore the ammonium/imidazolium contribution. The incorporation of the ammonium/imidazolium is difficult as the surface tension components for such surfactants are not readily found within the literature.

However, we consider a secondary approach in which the solubility parameters of the surfactants are used to determine the surface tension for comparative purposes. The Hildebrand solubility parameter (δ) is defined as the square root of the cohesive energy density (c) which is determined by a simple relation where ΔH is the heat of vaporization, R is the gas constant, T is the temperature and V_m is the molar volume (see **Equation 6.4**).[27]

Equation **6.4**

$$\delta = \sqrt{c} = \left[\frac{\Delta H - RT}{V_m} \right]^{\frac{1}{2}}$$ (Equation **6.4**)

The Hildebrand solubility parameter (δ) is composed of the Hansen parameters; the dispersive (δ_D), polar (δ_P), and hydrogen bonding (δ_H) components can be used to calculate the Hildebrand parameter through a simple relation (see **Equation 6.5**).[27]

Equation **6.5**

$$\delta^2 = \delta_D^2 + \delta_P^2 + \delta_H^2$$ (Equation **6.5**)

A relation (see **Equation 6.6**) has been developed to convert the Hansen components of the solubility parameter to surface tension values where δ_D is the

dispersive, δ_P is the polar, and δ_H is the hydrogen bonding component of the Hansen solubility parameter, and V_m is the molar volume.[27]

Equation **6.6**

$$\gamma = \frac{\left(\delta_d^2 + (2 \times \delta_p^2) + (0.488 \times \delta_h^2)\right)}{59 \times V_m^{-1/3}}$$

(Equation **6.6**)

The group contribution method can be used to determine the solubility parameters of most simple molecular structures (in this case the surfactants of interest to this work) using simple relations (see **Equations 6.7-6.9**).[27]. We explicitly use the constants as determined by Beerbower for the group contribution approach for molar volumes and Hansen Solubility Parameters (see **Table 6.3**).

Equation **6.7**

$$\delta_d = \frac{\sum_z zF_d}{V}$$

(Equation **6.7**)

Equation **6.8**

$$\delta_p = \frac{\left(\sum_z zF_p^2\right)^{1/2}}{V}$$

(Equation **6.8**)

Equation **6.9**

$$\delta_h = \left(\sum_z -\frac{zU_h}{V}\right)^{1/2}$$

(Equation **6.9**)

Table **6.3**

Table **6.3**: Group contributions for Molar Volumes and Hansen Parameters compiled by Beerbower.[**27**]

	F_d $(J^{1/2}\ cm^{3/2}/mol)$	F_p $(J^{1/2}\ cm^{3/2}/mol)$	U_h (J/mol)	$V\ (cm^3/mol)$
-CH3	420	0	0	33.5
-CH2-	270	0	0	16.1
-NH2	280	419	8400	19.2
-NH-	160	211	3100	4.5
-N=	164	1323	0	4.0
-CH=	223	70	0	12.4
5-6 mem. ring	190	0	0	13.5

Using these relations and the Beerbower values, the individual solubility parameters were calculated for all the surfactants utilized within these studies (see **Table 6.4**). We also check the accuracy of the group contribution method by comparing the hexadecane ($C_{16}H_{34}$) value reported from a reputable source within the literature [**26**] to the values generated from the group contribution method.

Table **6.4**

Table **6.4**: Group contribution approach to calculating Hansen Solubility Parameters and the subsequent Surface Tension values for the common surfactants utilized in this thesis.

	Literature $C_{16}H_{34}$	Calculated $C_{16}H_{34}$	Calculated $C_{18}H_{38}$	Calculated NH_2	Calculated $C_3H_4N_2$ (imidazole)	Calc. $C_{18}NH_2$	Calculated $C_{18}C_3H_4N_2$
V_m (cm^3/mol)	294.1	292.4	324.6	19.2	59.2	343.8	383.8
δ_d ($MPA^{1/2}$)	16.4	15.8	15.9	14.6	20.0	15.4	16.9
δ_p ($MPA^{1/2}$)	0	0	0.0	21.8	22.9	1.2	3.5
δ_h ($MPA^{1/2}$)	0	0	0.0	20.9	7.2	4.9	2.8
δ_{total} ($MPA^{1/2}$)	16.4	15.8	15.9	33.6	31.2	16.2	17.5
γ (mJ/m^2)	26.0	28.1	29.4	62.6	97.4	29.9	38.6

Even though good general agreement was observed between the hexadecane surfactant when comparing the literature to the group contribution method, predicting phase behavior of the nanocomposites proves to be elusive. Further analysis is required before definitive arguments can be made with respect to the anticipated phase behaviors.

6.4.3   PET/PC/alkyl-ammonium mmt (C25A) Nanocomposite Blends

Three different melt-blending methods were utilized to form PET/PC/C25A mmt nanocomposite blends: 1) a 'one-shot' extrusion in which all three components (PET+PC+C25A mmt) were added and extruded simultaneously, b) nanocomposite formation by letting down a pre-extruded PC/15wt% C25A mmt masterbatch to form PET/PC/C25A mmt nanocomposite blends, and c) nanocomposite formation by letting down a pre-extruded PET/15wt% C25A mmt masterbatch to form the PET/PC/C25A mmt nanocomposite blends. After the final extrusion step all samples were injection molded to form the test specimens for material properties testing.

The phase morphology and mmt dispersion was examined on the 'one-shot' samples by XRD and TEM. XRD indicated an intercalated morphology (see **Figure 6.5**), and upon close examination of the d-spacing (as determined by Bragg's law) we find the nanocomposite blends have identical d-spacing when compared to the PET/C25A mmt nanocomposite (see **Table 6.2 and 6.5**). XRD provides information for the periodic morphologies only and thus must be complemented by TEM in order to provide conclusive evidence on the complete morphology of the nanocomposite.

Figure **6.5**
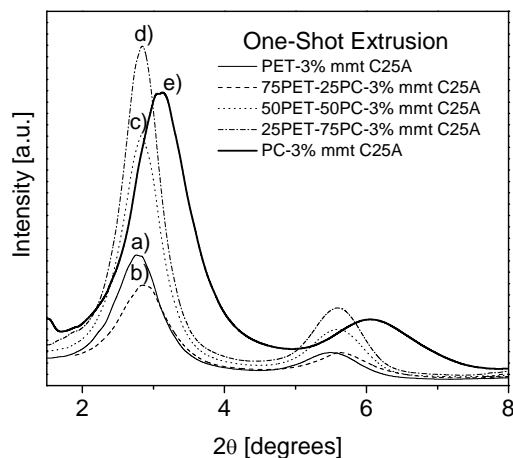
Figure **6.5**: XRD patterns of 'one-shot' PET/PC/C25A mmt nanocomposite blends: a) PET/mmt, b) 75PET/25PC/mmt, c) 50PET/50PC/mmt, d) 25PET/75PC/mmt, and e) PC/mmt.

Complementary TEM analysis confirmed the presence of a mainly intercalated morphology and verified the existence of selective mmt dispersion in the PET phase alone (see **Figure 6.6**) as was predicted by the thermodynamic arguments. The continuous phase in the 75PET/25PC (**Figure 6.6a, b**) and 50PET/50PC (**Figure 6.6c, d**) nanocomposites was the PET phase, as was governed by the viscous effects discussed previously (see **Chapter 5**). The PC phase is present in an unfilled yet well dispersed droplet-like morphology within the PET phase with distinct phase boundaries present.

It is impressive that even when PET is only 25% of the blend (**Figure 6.6e, f**) still all the filler is only dispersed in PET phase. This is more impressive when considering there are favorable thermodynamics of mixing for C25A and PC, which result in a well-dispersed intercalated PC/C25A nanocomposite with good mechanical properties (*c.f.* **Figure 6.4a, b**).

Figure **6.6**
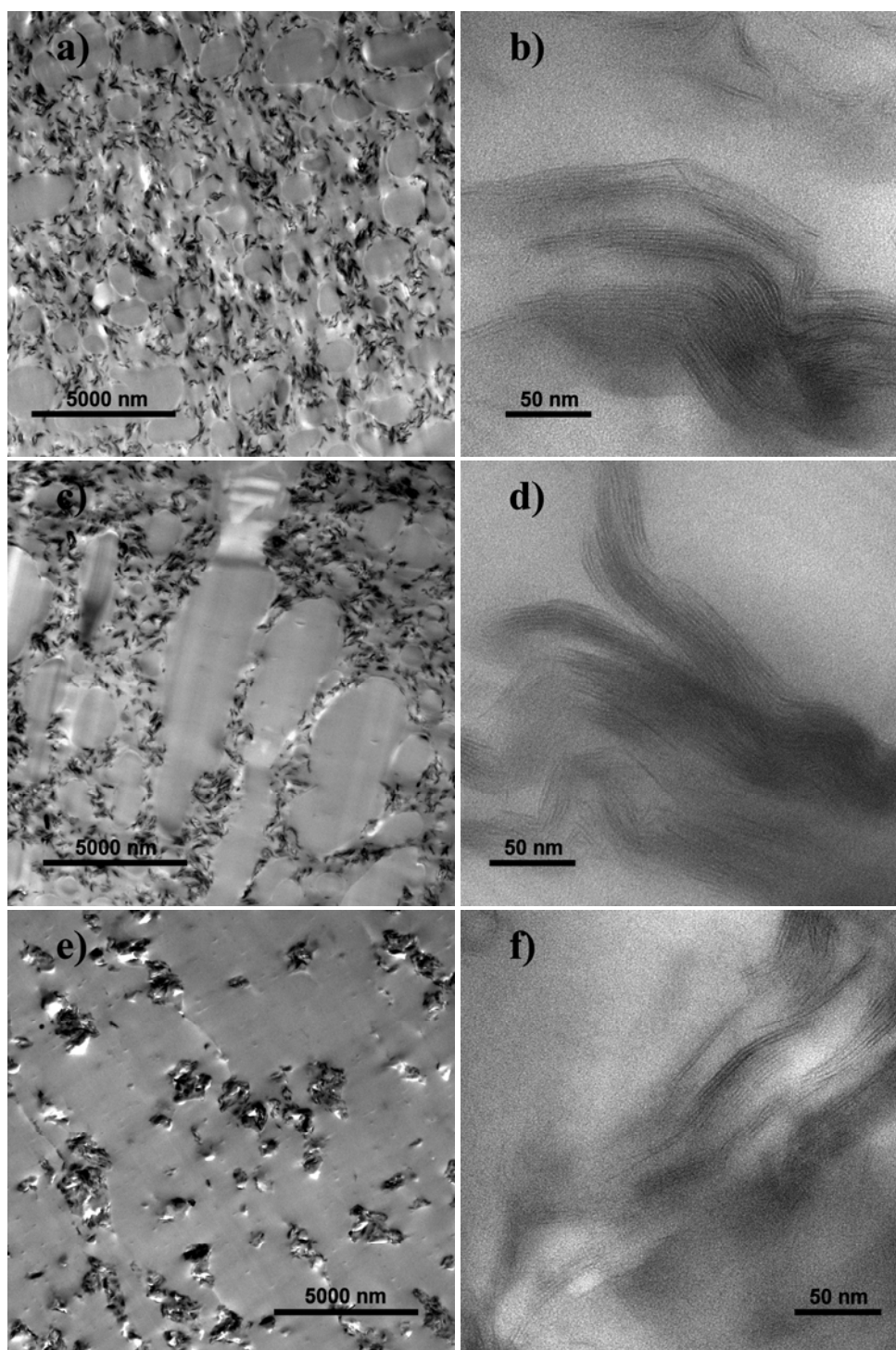
Figure **6.6**: TEM images of selective mmt dispersion in 'one-shot' PET/PC/C25A mmt blends: a-b) 75PET/25PC/C25A, c-d) 50PET/50PC/C25A, e-f) 25PET/75PC/C25A.

A processing related technique, masterbatching, was utilized in an attempt to overcome the thermodynamics of dispersion and control the dispersive phase of the mmt. Encapsulation of the mmt in the high-viscosity PC phase in a pre-extruded masterbatch prior to letting down the PC/mmt masterbatch to form the remainder of the nanocomposite blends was used in an attempt to either 'capture' the mmt in the PC phase or develop a morphology in which the mmt was dispersed in both the PET and PC phases. XRD analysis (see **Figure 6.7**) indicated the shift in 2θ developed in the 'one-shot' PET/PC/C25A nanocomposite blends was again present (**Table 6.5**).

TEM analysis verified the complete return of the mmt to the PET phase regardless of PET concentration (see **Figure 6.8**). Remarkably, no difference is observed between the 'one-shot' and PC based masterbatch samples, even when the PET was the minor component in the 25PET/75PC blend concentration (see **Fig. 6.8e,f**). The thermodynamic driving force was indeed strong enough to overcome the high viscosity of the PC phase to recapture all of the C25A mmt upon melt-blending.

Table **6.5**

Table **6.5**: XRD d-spacing of the PET/PC/C25A mmt Nanocomposite blends focusing on the three processing techniques used to attempt to control mmt dispersion.

	'One-Shot' d-Spacing (nm)	'PC-MB' d-Spacing (nm)	'PET-MB' d-Spacing (nm)
PET/3% mmt C25A	3.1	-	-
75PET/25PC/3% mmt C25A	3.1	3.1	3.1
50PET/50PC/3% mmt C25A	3.1	3.1	3.1
25PET/75PC/3% mmt C25A	3.1	3.1	3.1
PC/3% mmt C25A	2.8	-	-

Figure **6.7**
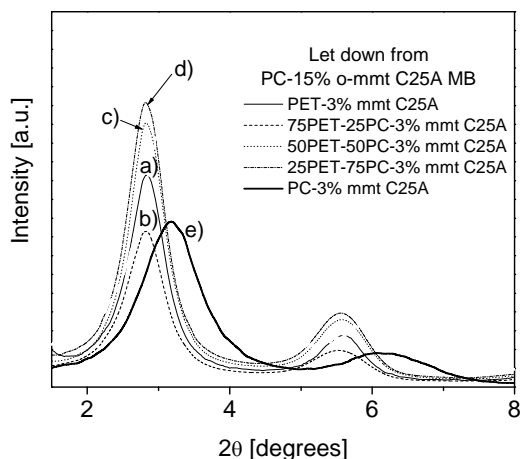
Figure **6.7**: XRD patterns of PET/PC/C25A mmt nanocomposite blends let down from PC/C25A MB: a) PET/mmt, b) 75PET/25PC/mmt, c) 50PET/50PC/mmt, d) 25PET/75PC/mmt, and e) PC/mmt.

To cover all possible systems, the C25A mmt was encapsulated within the PET phase in a masterbatch (PET-15% o-mmt) and was also let-down to form nanocomposite blends. The XRD and TEM confirmed identical behaviors to the 'one-shot' and the 'let-down from PC-MB' samples, with the mmt dispersed solely in the PET phase (not shown). Thus, regardless of the original dispersed phase, the thermodynamics governing the dispersion of polymer/o-mmt nanocomposites effectively predict the dispersed phase. Likewise, the first potential approach to altering the phase behavior, a melt-blending technique, was ineffective in controlling the dispersive phase of the layered silicate.

Figure **6.8**
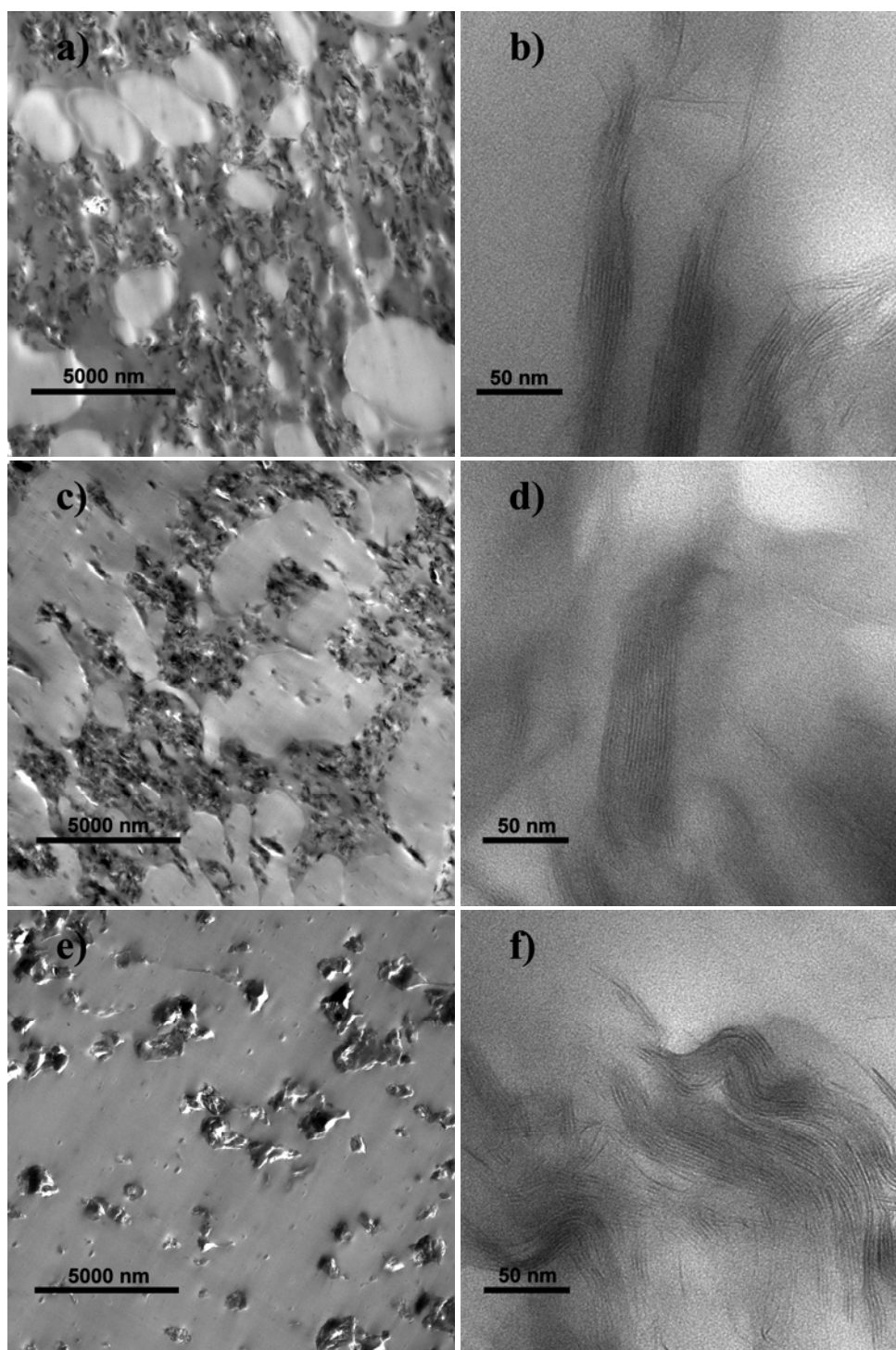
Figure **6.8**: TEM images of 'let-down from PC-MB' PET/PC/C25A mmt blends: a-b) 75PET/25PC/mmt, c-d) 50PET/50PC/mmt, e-f) 25PET/75PC/mmt.

6.4.4   PET/PC/imm-mmt (alkyl-imidazole) Nanocomposite Blends

The alternative approach to controlling the dispersive phase is through the utilization of modified surfactant chemistry. The alkyl-imidazole modified mmt, appears to offer the potential compatibility from a surface tension analysis, and also affords the opportunity to reduce the PET matrix degradation, albeit at the cost of being more detrimental to the PC matrix degradation.

Figure **6.9**

Figure **6.9**: XRD patterns of 'one-shot' PET/PC/imm-mmt nanocomposite blends: a) PET/mmt, b) 75PET/25PC/mmt, c) 50PET/50PC/mmt, d) 25PET/75PC/mmt, and e) PC/mmt.

A 'one-shot' extrusion approach and a let-down from a pre-extruded PET-MB approach were employed to produce PET/PC/imm-mmt nanocomposites. The dispersion of the 'one-shot' nanocomposites was characterized via XRD (see **Figure 6.9**). No further gallery expansion or definitive trends defining the potential mmt dispersive phase

were observed in the XRD. Thus, complementary TEM was required to provide further insight into the nanocomposite structure.

TEM confirms the presence of a well-dispersed intercalated morphology and revealed the development of "compatibilized" phase morphology (see **Figure 6.10**). These findings are in sharp contrast with the selective o-mmt dispersion observed in the C25A filled blends. The compatibilized structure has equivalent dispersion of the mmt throughout the PET and PC phases, with no true phase boundary recognition. Another key point of interest relates to the tactoid size reduction in comparison to the C25A mmt based nanocomposites indicating better dispersion of the alkyl-imidazole mmt in the PET/PC/imm-mmt nanocomposite blends as a function of the increased viscosity of the nanocomposite blend. We anticipate the 'compatibilized' morphology will have a unique influence on the material properties of the nanocomposite, specifically with respect to the mechanical and crystallization behaviors.[2] The changes will be rooted in the morphology of the nanocomposite, which is directly related to the absence of the distinct PET and PC domains.

Figure **6.10**
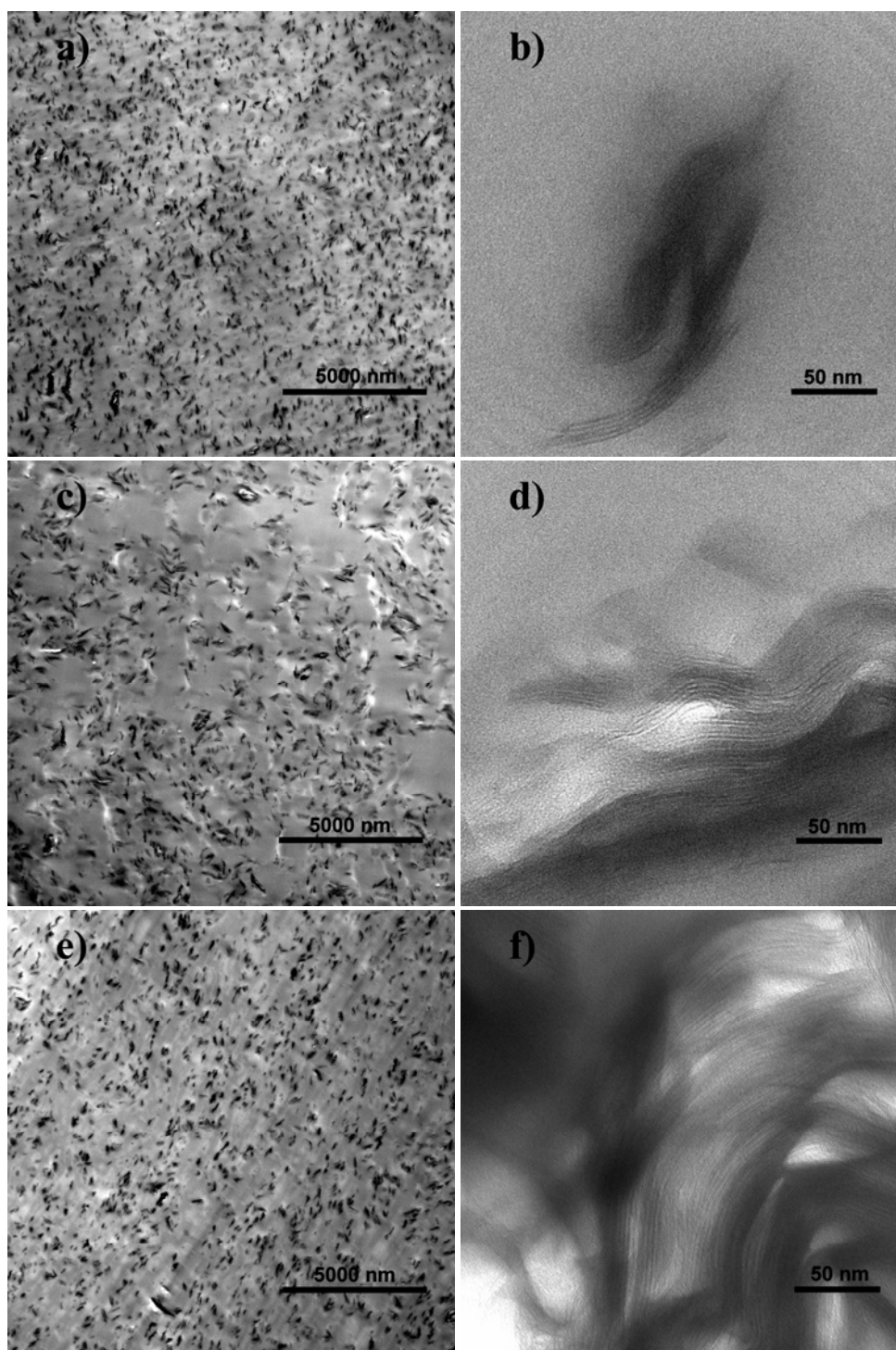
Figure **6.10**: TEM images of compatibilized 'one-shot' PET/PC/imm-mmt nano blends: a-b) 75PET/25PC/mmt, c-d) 50PET/50PC/mmt, e-f) 25PET/75PC/mmt.

Encapsulation of the o-mmt within a PET masterbatch prior to formation of the nanocomposite blends through the let-down process was also undertaken for the PET/imm-mmt nanocomposites. Upon examining the morphology of such nanocomposites, we find the XRD (see **Figure 6.11**) is identical to the 'one-shot' compatibilized blends. The intercalated and 'compatibilized' morphology is confirmed by TEM (see **Figure 6.12**).

Figure **6.11**
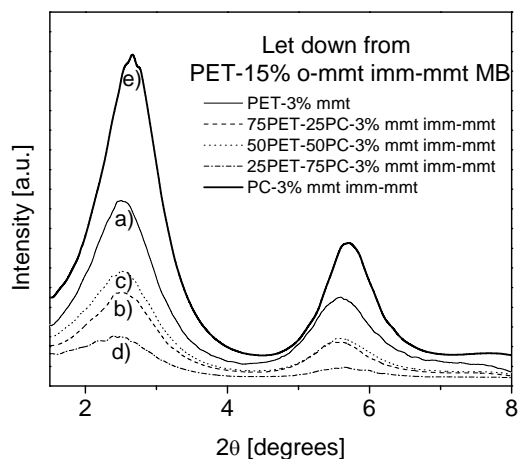
Figure **6.11**: XRD patterns of 'let-down from PET-MB' PET/PC/imm-mmt nanocomposite blends: a) PET/mmt, b) 75PET/25PC/mmt, c) 50PET/50PC/mmt, d) 25PET/75PC/mmt, and e) PC/mmt.
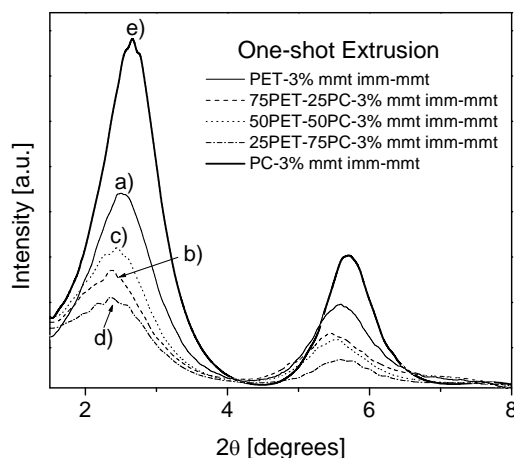
Figure **6.12**
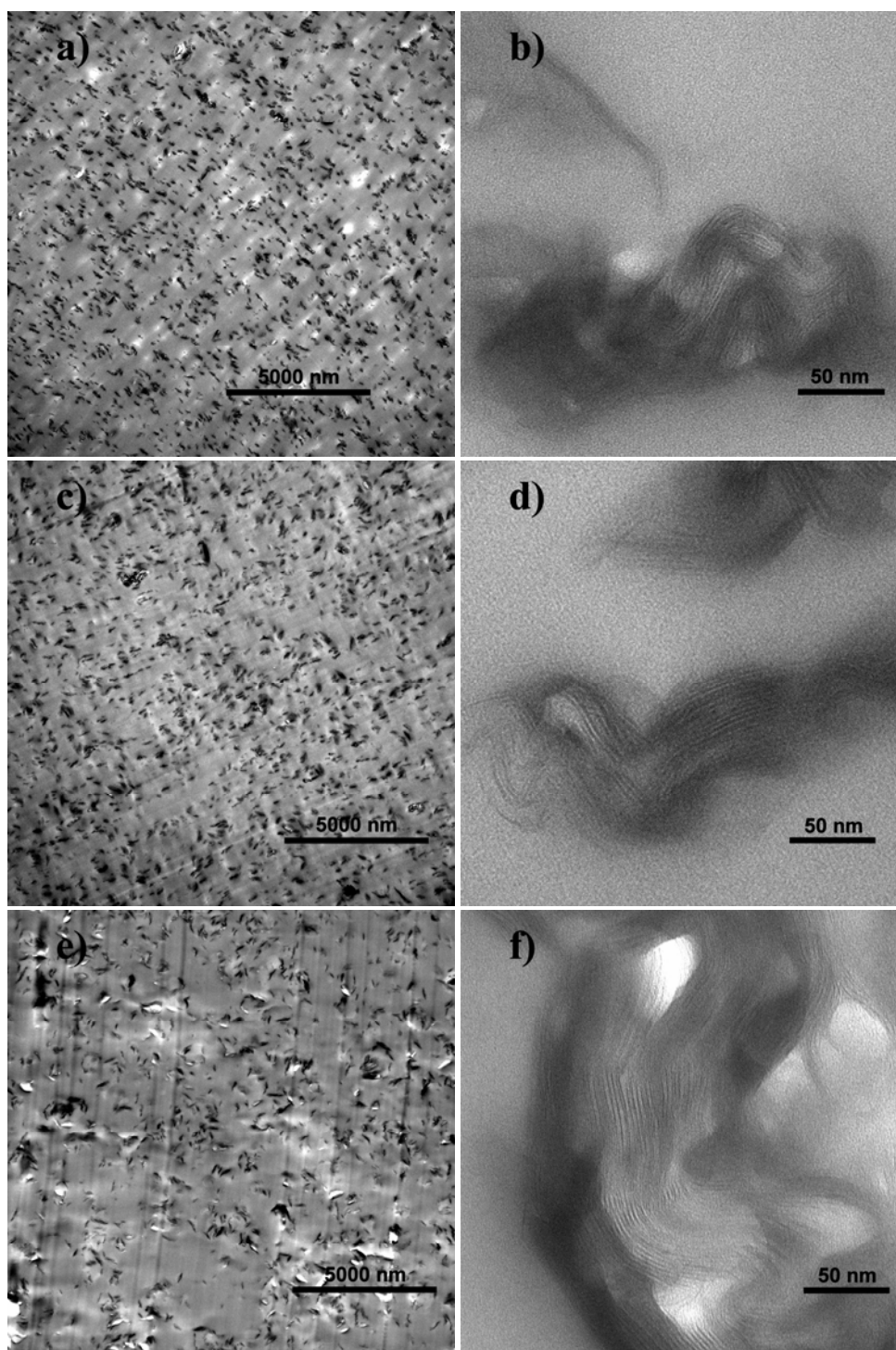
Figure **6.12**: TEM images of compatibilized 'let-down from PET-MB' PET/PC/imm-mmt nano blends: a-b) 75PET/25PC/mmt, c-d) 50PET/50PC/mmt, e-f) 25PET/75PC/mmt

6.4.5   Mechanical Behaviors

Instron tensile tests were conducted on the injection molded "dogbone" specimens in order to measure the stiffness and elongation (ductility) characteristics of the blends and their corresponding nanocomposites. Polymer/layered silicate nanocomposites exhibit superior mechanical properties when compared to the bulk polymer if favorable dispersion is achieved. The relative enhancement in tensile modulus of stiff polymers such as PET and PC is typically limited compared to lower stiffness polymers (PE, EVOH, PLA, etc.) which show improvements on the order of 100 % to 300 % over the bulk polymer (see **Chapter 2**). Without matrix or filler functionalization to promote covalent or hydrogen bonding between the two, the relative modulus improvement of the nanocomposite will remain limited in the instance of the PET/PC/mmt nanocomposite blends. Thus, we expect a nominal, yet distinct improvement in the stiffness of the nanocomposite blends.

Instron analysis indicates that dispersion of 3 wt. % mmt of the high-aspect ratio layered silicates improved the modulus on the order of 15 % to 20 % for the PET/mmt and all the PET/PC nanocomposite blends, and by 15 % for the PC/mmt nanocomposites (see **Figure 6.13**). It is rather striking that similar modulus enhancements are observed in all of the nanocomposite blend systems as drastic variance in the composite morphology was observed. This is especially the case for those nanocomposite blends where the mmt is preferentially dispersed within the PET phase ('non-compatibilized') and for those where a 'compatibilized' morphology, no distinct phase boundaries and equivalent mmt dispersion, were observed.

Figure **6.13**
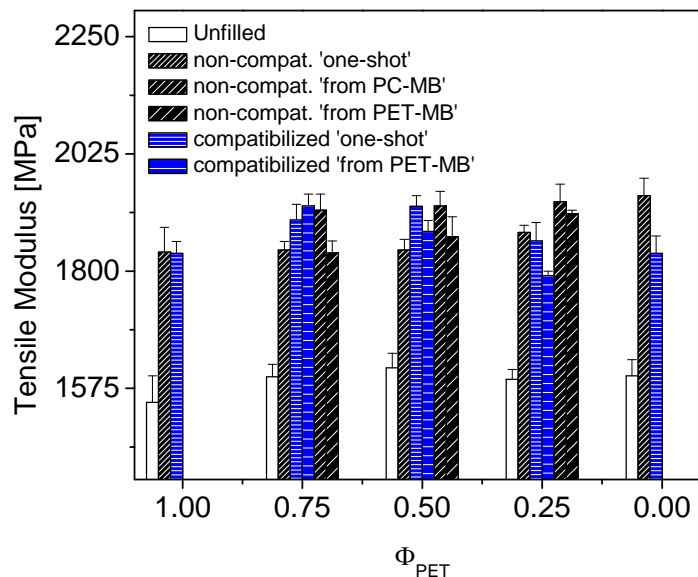
Figure **6.13**: Tensile modulus comparison of the unfilled PET/PC blends to the 'non-compatibilized' and 'compatibilized' PET/PC/mmt nanocomposite blends.

The morphology does have a substantial impact when considering the elongation-at-break (ductility) behavior of the nanocomposite blends (see **Figure 6.14**). In the PC rich nanocomposites ($\Phi_{PC} > 0.50$), the brittleness of the nanocomposite is noteworthy as it is regardless of phase morphology. The elongation at break drops 50 % to 90 % depending on the filler. As expected, the imm-mmt causes stronger brittleness in PC than the quaternary ammonium based C25A mmt given the greater PC matrix degradation in the presence of the imidazolium compound compared to an amine.

The most interesting behavior is found in the nanocomposites in which phase 'compatibilized' morphology is present, and for which $\Phi_{PC} \leq 0.50$. In these nanocomposites, the elongation-at-break remains at least equivalent to the bulk materials,

and in the case of the 75PET/25PC ratio has greater ductility than the unfilled blend itself. Prior to breakage, a significant amount of necking takes place.

Figure **6.14**
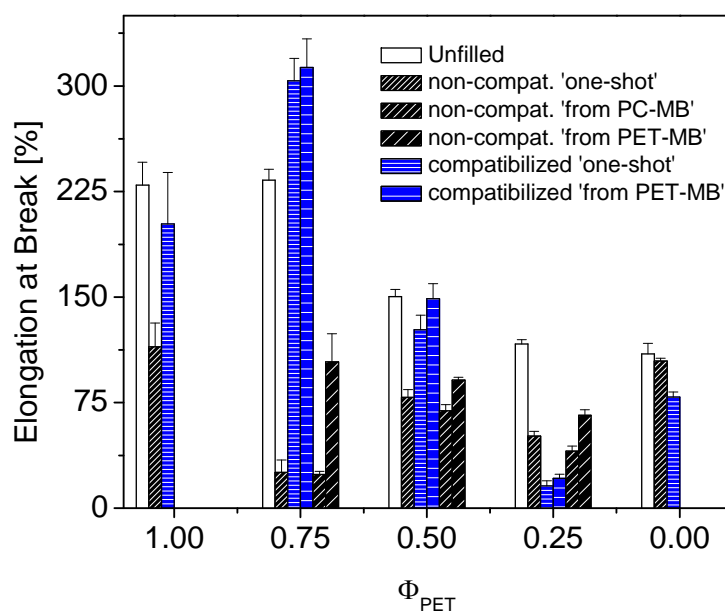
Figure **6.14**: Tensile elongation-at-break (ductility) comparison of the unfilled PET/PC blends to the 'non-compatibilized' and 'compatibilized' PET/PC/mmt nanocomposites.

Unique behaviors were noted when comparing TEM images of the region in which necking had occurred with images taken from an area in which no necking had transpired (see **Appendix 6.6.1**). The improvement in the ductility of such nanocomposites is most likely rooted in the crystallization behaviors coupled with the morphology. The uninterrupted phases of the compatibilized nanocomposite coupled with the smaller spherulites and the suspected increase in the number of inter-crystalline links is believed to be the impetus for the improvement in elongational characteristics (see **Chapter 3**). Likewise, the phase compatibility is most likely aided by a small amount of

transesterification. Thus, it must be verified that a high degree of copolymer formation does not drive ductility and is a true nano effect.

6.4.6   Transesterification Analysis

When examining transesterification via infrared spectroscopy (IR), three distinct bands are of particular interest: (1) the 1775 cm^{-1} band that corresponds to the carbonyl stretching of an amorphous aromatic carbonate (PC), (2) the 1720 cm^{-1} band associated with the carbonyl stretching of an aliphatic ester (PET), and (3) the 1740 cm^{-1} band associated with the stretching of a mixed aliphatic-aromatic carbonate, which is a product of the ester-carbonate transesterification reaction.[15][19][28]

Transesterification in the unfilled blends, 'non-compatibilized' nanocomposite blends, and 'compatibilized' nanocomposite blends was initially examined via ATR-FTIR on the injection molded micro-flexural bars (see **Figure 6.15**). The peak intensity of the PC reflection (1780 cm^{-1}) was normalized such that direct comparison of the PET peak intensity (1720 cm^{-1}) across the spectrum of samples (morphologies) could be examined.

Figure **6.15**
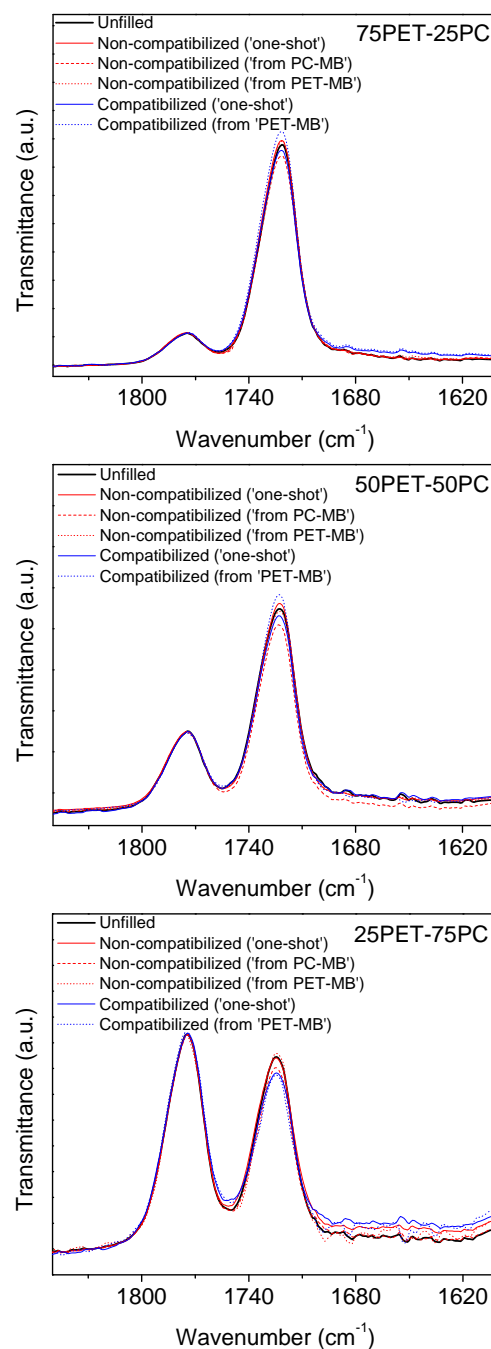
Figure **6.15**: ATR-FTIR studies examining the transesterification occurring in the unfilled blends compared to the 'non-compatibilized' (C25A mmt based) and 'compatibilized' (imm-mmt based) nanocomposite blends.

When comparing the carbonyl stretching of the aliphatic ester in the PET ($1720\,cm^{-1}$) in the PET rich blend (75PET/25PC) to the corresponding nanocomposites, no significant intensity deviation is observed and no peak splitting occurs. If transesterification in the nanocomposites had occurred to a much greater extent than in the unfilled blends, the intensity of the peak would have increased dramatically and would have shifted/split, with the new peak corresponding to the stretching of a mixed aliphatic-aromatic carbonate. Likewise, similar behaviors occur in the equivalent blends (50PET/50PC) and the PC rich blends (25PET/75PC) in which no significant intensity deviations or peak splitting occurs. Thus, the result of the ATR-FTIR indicates that independent of blend concentration, phase morphology, or if the sample is contains filler; no distinct differences in the transesterification behaviors are observed. Therefore, we may initially conclude any transesterification that may be occurring in the nanocomposite blends is no greater than what occurs is in the unfilled blends – and in general, any amount of transesterification that may be occurring is undetectable in the ATR-FTIR.

Further exploration of the transesterification reactions of the nanocomposite blends was examined through Raman Spectroscopy (see **Figure 6.16**). Here we compare a 50PET/50PC unfilled blend to the corresponding 'compatibilized' nanocomposite, and although a slight shift in the peak intensity occurs in the nanocomposite – an indication that some transesterification has occurred – we again conclude the amount of transesterification that occurs during melt-blending is low. It is important to note that if a significant amount of transesterification was to occur, the 50/50 blend composition has been found to experience the greatest copolymer conversion ratios. [**18**]

Figure **6.16**
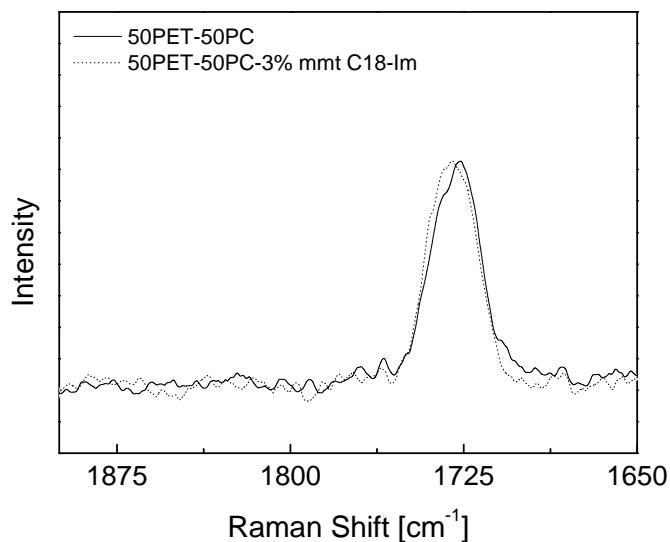
Figure **6.16**: Raman spectroscopy monitoring the PET band for transesterification in the unfilled 50PET/50PC and 'compatibilized' nanocomposite blend.

Thus, from this standpoint it is again believed transesterification does not take place in any greater amount than the respective unfilled blends within the detectable limits of the instrumentation. Further verification that excess transesterification in the presence of the mmt fillers does not occur in any detectable extent can be obtained through MDSC studies where the T_g of the PET and PC phases were examined (see **Figure 6.17**).

Figure 6.17
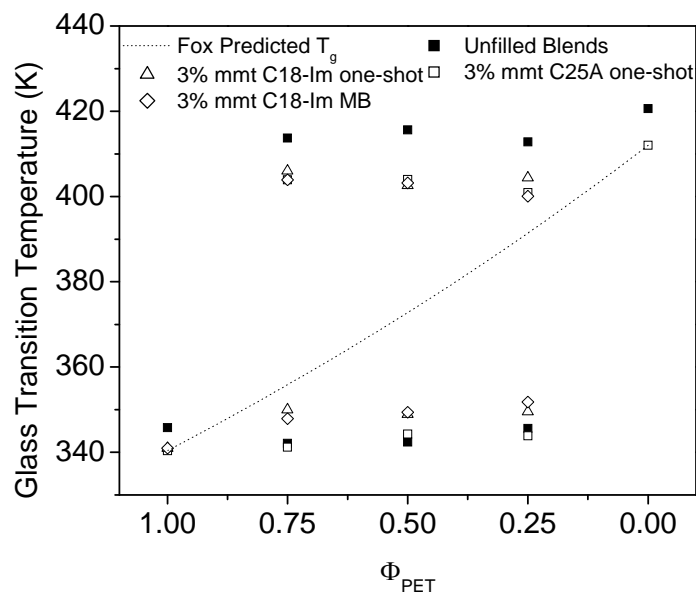
Figure 6.17: Transesterification analysis through monitoring the glass transition temperature (T_g) in modulated DSC scans for the unfilled blends (open symbols) and the corresponding nanocomposite blends (closed symbols).

Complete transesterification in a PET/PC blend where a copolymer or a miscible blend is generated, the glass transition temperature (T_g) has been found to be predicted by the empirical Fox equation [**29**] (see **Equation 6.10**) where the copolymer/blend T_g is calculated from the weighted average of the glass transition temperature of the two polymers (T_g^{PET} and T_g^{PC}) where W_{PET} and W_{PC} are the corresponding weight fractions.[**17**]

Equation 6.10

$$\frac{1}{T_g} = \frac{W_{PET}}{T_g^{PET}} + \frac{W_{PC}}{T_g^{PC}}$$

(**Equation 6.10**)

Two distinct T_g's are present regardless of surfactant chemistry or PET/PC phase morphology, further indicating the lack of detectable transesterification. There is no measurable difference in the glass transition temperatures as they generally fall within the range of instrumental error.

Thus, the combined ATR-FTIR, Raman Spectroscopy, and DSC results strongly indicate that the PET/PC phase compatibilization observed for the imm-mmt based nanocomposites is not a function of transesterification. Therefore, the conclusion can be drawn that if the thermodynamics of surfactant selection are properly chosen, the dispersive phase of the o-mmt can absolutely be controlled – which bears interesting insight into not only PET-PC nanocomposite blends, but also other polymer blend systems.

6.5   Conclusions

The nanocomposite blend morphology of PET/PC/mmt blends was studied and controlled by modifying the thermodynamics of dispersion through tailoring the mmt surfactant chemistry. Two distinct morphologies were produced: (1) a 'non-compatibilized' system in which mmt was dispersed primarily/solely in the PET phase with phase separated PC phases that do not bear any mmt filler, (2) a phase 'compatibilized' PET/PC system in which no distinct phase boundary recognition is possible and the mmt is well-distributed throughout. Regardless of the morphology the tensile moduli improves around 20 % compared to the corresponding unfilled systems. A

significant improvement in the elongation-at-break in PET-rich 'compatibilized' nanocomposites is also observed.

The combined ATR-FTIR, Raman Spectroscopy, and DSC studies verify that measurable transesterification does not seem to occur in any of the nanocomposites after simple melt-blending, at least not to any extent higher than the unfilled blends. These intriguing results bear promise for the PET/PC/mmt hybrid materials for applications in which tailored properties, such as the ductility in this case, are needed.

6.6   Appendix

6.6.1   Instron Induced mmt Alignment

The stress/strain behavior of the compatibilized 75PET/25PC/mmt nanocomposites was remarkable as an increase in the ductility was observed over the unfilled blend (see **Figure 6.18**). In comparison, we find the non-compatibilized nanocomposite blend has a much greater degree of brittleness as it fails to reach 100 % elongation.

Figure **6.18**
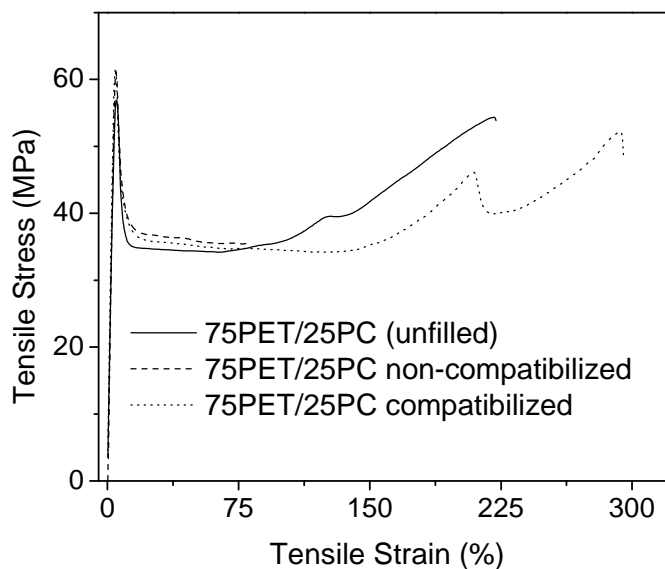
Figure **6.18**: Typical Stress/Strain curve from Instron tensile testing.

Furthermore, we observe a unique necking pattern in the high-elongation compatibilized nanocomposites (see **Figure 6.19**). The compatibilized nanocomposite develops a hollow core as the polymer undergoes 'cold flow'; all other samples (non-compatibilized nanocomposite blends, unfilled blends, the bulk polymers and their nanocomposites) all undergo normal necking. A more detailed visual representation was created for visualization purposes (see **Figure 6.20**).

Figure **6.19**
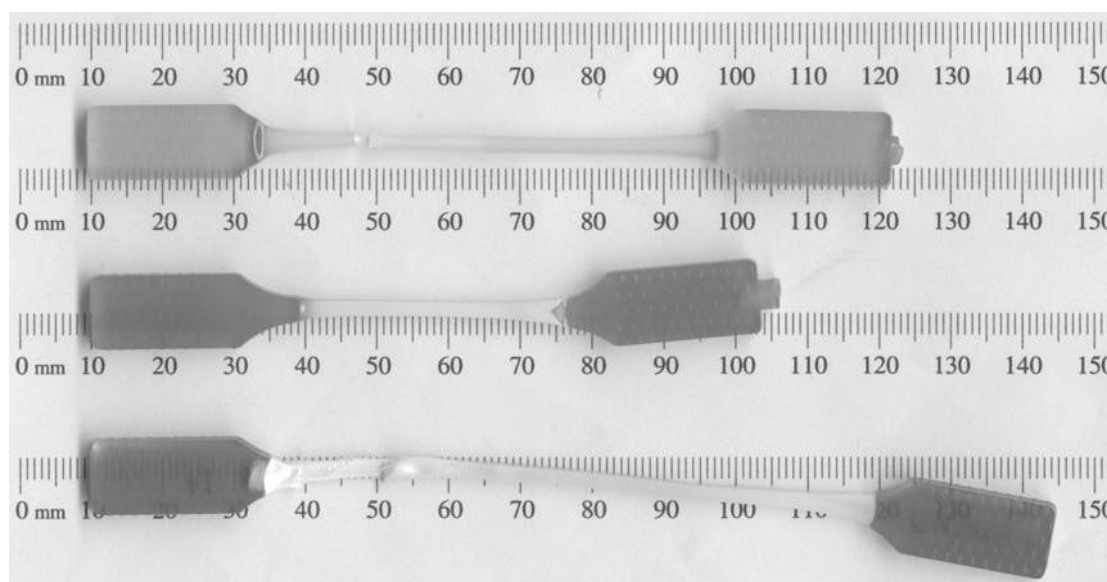
Figure **6.19**: Strained samples from an Instron tensile test: Top sample is the unfilled 75PET/25PC blend, center sample is the 75PET/25PC/non-compatibilized nanocomposite blend, and the bottom sample is the 75PET/25PC/compatibilized nanocomposite blend.

TEM analysis was completed on two regions of the strained high-elongation 75PET/25PC/compatibilized nanocomposite blend to determine the mmt platelet orientation with little drawing (section A-A) and after amounts of strain were exposed to the region (section B-B).

Figure **6.20**
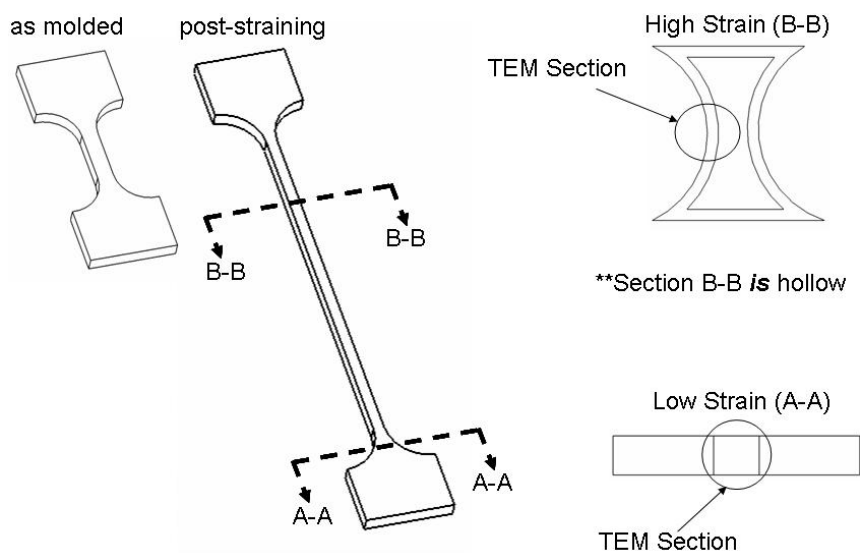
Figure **6.20**: Microtoming locations for the high-strain 75PET/25PC/compatibilized nanocomposite blend: Region A-A is the low strain region and Region B-B is the high strain region.

The disparity in the TEM analysis of the low-strain region (see **Figure 6.22**) and the high-strain region (see **Figure 6.21**) is remarkable. The high strain region has used viscous forces to not only preferentially align the mmt tactoids in the direction of draw, but also further broke apart the tactoid size into stacks of a few individual platelets, and in some cases individual layers (high magnification image in **Figure 6.21**). The low-strain sample exhibits little, if any preferential alignment, and has tactoids with upwards of 10 sheets per stack.

Figure **6.21**
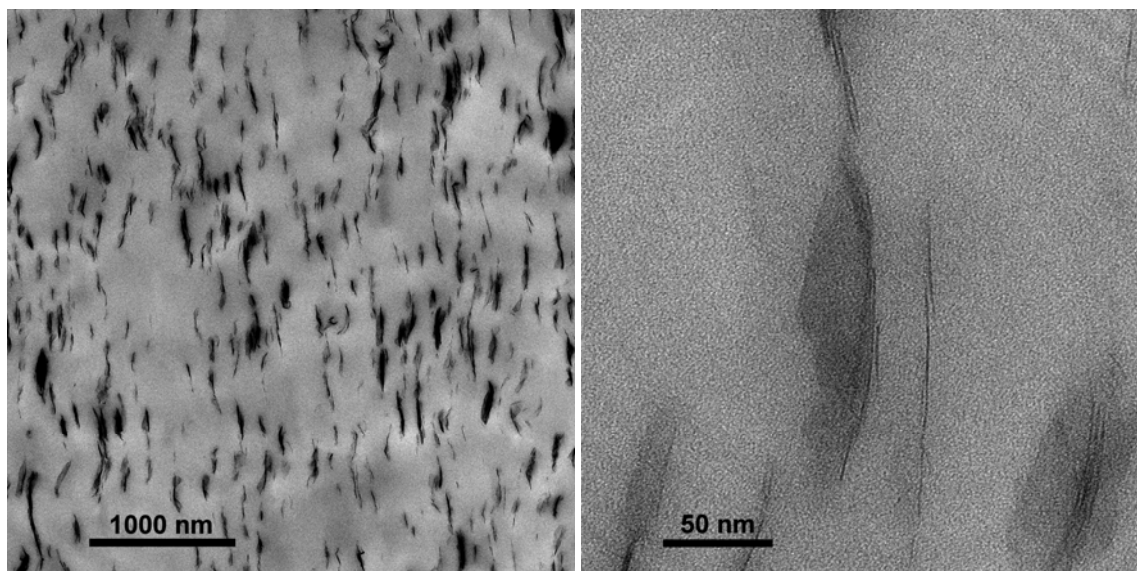
Figure **6.21**: TEM images of the high-strain region of the tensile tested IM dogbone.

Figure 6.22
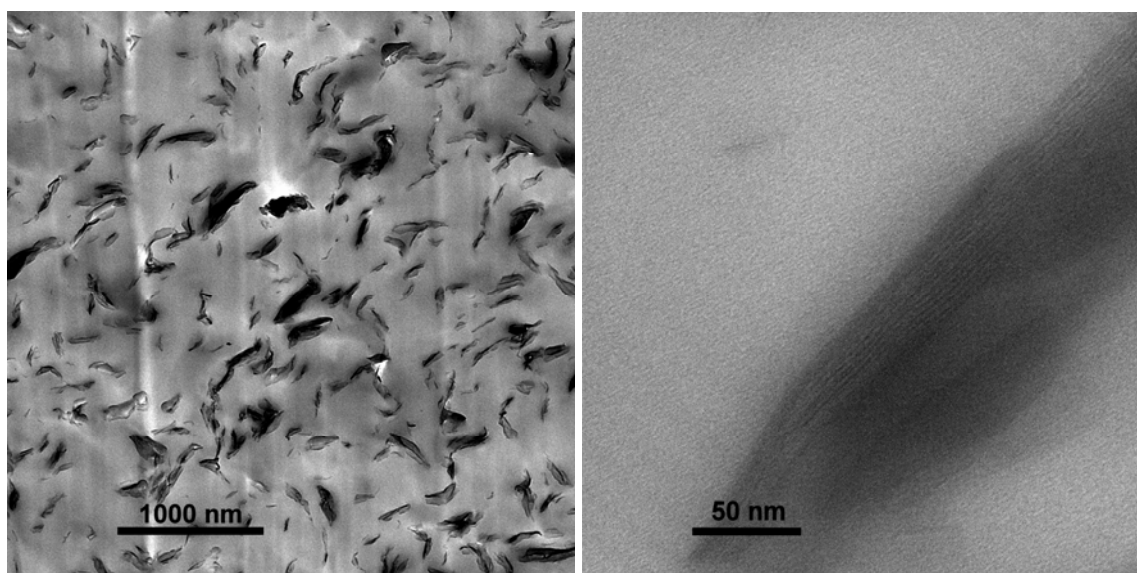
Figure **6.22**: TEM images of the low-strain region of the tensile tested IM dogbone.

6.6.2 Injection Molding Parameters

Figure **6.23**

Figure **6.23**: Injection molding processing data sheet for PET/PC/mmt nanocomposite blends.

References

1. Kong, Y. and Hay, N., *Journal of Polymer Science: Part B: Polymer Physics* 2004; 42:2129-2136.

2. Suzuki, T., Tanaka, H., and Nishi, T., *Polymer* 1989; 30:1287-1297.

3. Reinsch, V.E. and Rebenfeld, L., *Journal of Applied Polymer Science* 1996; 59:1913-1927.

4. Alexandre, M. and Dubois, P., *Materials Science and Engineering* 2000; R28: 1-63.

5. Ray, S.S. and Okamoto, M., *Progress in Polymer Science* 2003; 28:1539-1641.

6. Giannelis, E.P., Krishnamoorti, R., and Manias, E., *Advances in Polymer Science.* 1998; 138:107–148.

7. Xu, W., Liang, G., Zhai, H., Tang, S., Hang, G., and Pan, W-P., *European Polymer Journal* 2003; 39:1467-1474.

8. Xie, W., Gao, Z., Pan, W-P., Hunter, D., Singh, A., and Vaia, R., *Chemistry of Materials* 2001**;** 13:2979–2990.

9. Sanchez-Solis, A., Romero-Ibarra, I., Estrada, M.R., Calderas, F., and Manero, O., *Polymer Engineering and Science* 2004; 44:1094-1102.

10. Ou, C.F., Ho, M.T., and Lin, J.R., *Journal of Polymer Research* 2003; 10:127-132.

11. Yoon, P.J., Hunter, D.L., and Paul, D.R., *Polymer* 2003; 44:5323–5339.

12. Yoon, P.J., Hunter, D.L., and Paul, D.R., *Polymer* 2003; 44:5341–5354.

13. Wang, Z.M., Chung, T.C., Gilman, J.W., and Manias, E., *Journal of Polymer Science: Part B: Polymer Physics* 2003; 41:3173–3187.

14. Awad, W.H., Gilman, J.W., Nyden, M., Harris, R.H., Sutto, T.E., Callahan, J., Trulove, P.C., DeLong, H.C., and Fox, D.M., *Thermochimica Acta* 2004; 409:3-11.

15. Denchev, Z., Sarkissova, M., Radusch, H-J., Luepke, T., and Fakirov, S., *Macromolecular Chemistry and Physics* 1998; 199:215–221.

16. Godard, P., Dekoninck, J.M., Devlesaver, V., and Devaux, J., *Journal of Polymer Science: Part A: Polymer Chemistry* 1986; 24:3315–3324.

17. Marchese, P., Celli, A., and Fiorini, M., *Macromolecular Chemistry and Physics* 2002; 203:695-704.

18. Zheng, W-g., Wan, Z-h., and Qi, Z-n., *Polymer International* 1994; 34:301-306.

19. Porter, R.S., and Wang, L-H., *Polymer* 1992; 33:2019–2030.

20. Vaia, R.A. and Giannelis, E.P., *Macromolecules*, 1997; 30:7990–7999.

21. Vaia, R.A. and Giannelis, E.P., *Macromolecules*, 1997; 30:8000–8009.

22. Van Oss, C.J., Chaudhury, M.K., and Good, R.J., *Chemical Reviews* 1988; 88:927–941.

23. Wu, W., Giese, R.F., and Van Oss, C.J., *Langmuir* 1995; 11:379-382.

24. Ponter, A. B., Jones, W.R., and Jansen, R.H., *Polymer Engineering and Science* 1994; 34:1233–1238.

25. Wu, S., **Polymer Interface and Adhesion,** M. Dekker, New York, NY, 1982.

26. van Oss, C. J., **Interfacial Forces in Aqueous Media**, CRC Press, New York, NY, 2006.

27. Barton, A.F.M., **Handbook of Solubility Parameters and Other Cohesion Parameters,** CRC Press, Boca Raton, 1991.

28. Huang, Z.H. and Wang, L.H., *Makromolekulare Chemie-Rapid Communications* 1986; 7:255-259.

29. Fox, T.G., *Bulletin of the American Physical Society* 1956; 1:123.

Crystallization and Melting Behaviors of Poly(ethylene terephthalate) / Polycarbonate / Montmorillonite Nanocomposite Blends

7.1   Summary

Novel nanocomposite blends of Poly(ethylene terephthalate) and Polycarbonate with a layered silicate filler (montmorillonite) filler were developed. Remarkable enhancements in the ductility of the nanocomposite blends were detailed in systems in which the thermally stable alkyl-imidazole surfactant compatibilized the resultant nanocomposites. Despite the lack of phase separation in the compatibilized nanocomposites, such systems retain a remarkable degree of crystalizability. Even the non-compatibilized nanocomposites, with the presence of well defined amorphous PC inclusions, led to high relative crystallinity in the nanocomposite blends. The ductility enhancement observed in certain morphologies of these novel systems was striking, especially in the absence of significant amounts of transesterification reactions, and is again believed to be associated with the reduction in crystal size which is likewise correlated to an increase in the number of inter-crystalline linkages, and thus an improvement in nanocomposite ductility.

7.2   Introduction

Polymer nanocomposites often achieve enhancements in the mechanical properties with concurrent improvements in thermal stability, barrier properties, crystalizability, and/or the flammability characteristics.[1][2][3][4] The general crystallization behaviors of nanocomposites were discussed in **Chapter 2** of this thesis and the specific effects on PET/mmt nanocomposites were detailed in **Chapter 3**. Briefly revisiting the effects of a nano-scale filler on polymer crystallinity, we find behaviors can be classified in two general categories: (1) behaviors specific to a given polymer or class of polymers, and (2) general behaviors observed across all crystallizable polymer/nano-scale filler reinforced systems.[5] The first subgroup contains examples such as nylon-6/mmt nanocomposites that are known to develop a γ-crystal phase next to the mmt filler as a function of the strong hydrogen bonding of each amide group with the silicate surface.[6][7] The latter category includes those behaviors rooted in the nucleation and crystallization kinetics. Polymer nanocomposites in general observe strong nucleation density increases with mmt addition, reductions in the linear growth rate and spherulite size when comparing the nanocomposite to the bulk polymer, and observe no change in the equilibrium melting temperature.[5]

PET nanocomposites have been shown to exhibit heterogeneous nucleation, reduced undercoolings, increased nucleation densities, slower linear crystal growth rates, and an increase in the degree of crystallinity upon nanocomposite formation.[8][9][10] PET/PC blends also have unique crystallization behaviors with the amorphous PC domains acting as crystal nucleation and growth termination points. Alterations in the

structure of PET that result from transesterification reactions will hinder the crystallization of the blend.[**11**]

Morphological control of PET/PC/mmt nanocomposite blends through surfactant chemistry modification lead to two distinct dispersion scenarios: 1) a phase immiscible system in which selective dispersion of the mmt filler occurs in the PET phase alone ('non-compatibilized') and 2) a system in which the filler acts as a compatibilizing agent resulting in uniform montmorillonite distribution that lacks PET/PC phase boundary recognition ('compatibilized').[**12**] Equivalent improvements in the modulus were observed autonomous of morphology, yet startling enhancements in the ductility occurred in the PET rich phase compatibilized nanocomposites.

When considering all of these factors together a high degree of complexity is imparted such that concrete statements regarding the crystallization behaviors of PET/PC/montmorillonite nanocomposite blends may be difficult to develop. This work aims to elucidate the crystallization behaviors of such novel nanocomposite blends. The effects of filler addition, phase morphology, and the presence of the amorphous PC domains on the crystallization behaviors will be examined. These studies mainly focused on the crystallization behaviors of an unfilled 50PET/50PC blend compared to its respective 'non-compatibilized' and 'compatibilized' nanocomposites, and as a baseline for comparison the corresponding unfilled PET and its PET/mmt nanocomposites.

7.3   Experimental

7.3.1   Sample Preparation

Nanocomposite blends with a well-characterized morphology were prepared via melt-blending in the previous study.[12] Two distinct phase morphologies were developed for further study, the 'non-compatibilized' and the 'compatibilized' nanocomposite blends. The samples examined in this work were melt-blended by one-step extrusion (PET + PC + mmt were simultaneously added and extruded) followed by injection molding to form micro-tensile and flexural bars. An overview of the samples examined in this study along with the resultant phase morphology may be found in **Table 7.1**.

Table **7.1**

Table **7.1**: Crystallization and melting behaviors of PET upon cooling from a quiescent melt.

Acronym	mmt	mmt loading (wt. %)	Dispersive Phase
PET	-	-	-
PET/C25A mmt	C25A	3	PET
PET/imm-mmt	imm-mmt	3	PET
50PET/50PC	-	-	-
50PET/50PC/non-compatibilized	C25A	3	PET
50PET/50PC/compatibilized	imm-mmt	3	-

The acronym 'C25A' refers to the commercially available (Southern Clay Products) Cloisite 25A montmorillonite that has a cation exchange capacity (CEC) of 0.95 meq/g and is modified with dimethyl hydrogenated tallow 2-ethylhexyl quaternary

ammonium surfactant. The acronym 'imm-mmt' stands for a Na$^+$ montmorillonite (PGW – obtained from Nanocor) that has a CEC of 1.4 meq/g and was exchanged with a thermally stable alkyl-imidazole surfactant that was synthesized and exchanged using protocols outlined in **Chapter 3**.

7.3.2   Crystallization Behaviors

The crystallization and melting behaviors were examined using differential scanning calorimetry (DSC). The DSC was performed on a TA Instruments Q100 DSC calibrated with sapphire and indium standards under helium purge with a secondary nitrogen purge. The scanning rate was 10 °C/min in all cases unless otherwise noted. The degree of crystallinity was calculated using **Equation 7.1** where ΔH_m is the enthalpy of fusion and ΔH_m° is the enthalpy of fusion of the perfect crystalline PET (125.5 J/g).[**13**]

Equation **7.1**

$$\chi_c = \frac{\Delta H_m}{\Delta H_m^o} \times 100 \qquad\qquad (\text{Equation } \mathbf{7.1})$$

The crystallization process was taken to near completion via cold crystallization of the injection molded samples at 140 °C for 1.5 hours. All DSC studies examining the enthalpy of crystallization and melting were repeated three times with the average value reported.

Optical microscopy under cross polarizers (PLOM) was employed to examine the spherulite shape and size of bulk PET and its nanocomposites on an Olympus BX-41 microscope (Hitech Instruments) equipped with a SPOT Insight QE camera. The

microscope was also fit with a Linkam LTS 350 hot stage, controlled using LinkSys software and cooled via liquid nitrogen, such that isothermal crystallization at elevated temperatures could be monitored. The samples were held isothermally at 280 °C, above the melt temperature, for three minutes to allow for complete melting of the crystalline material to occur. Subsequent crystallization took place isothermally at 237 °C and 227 °C (depending upon the sample) upon cooling (at a rate of 25 °C/minute) from the quiescent melt. Isothermal crystallization was allowed to proceed for 30 minutes during which a series of sequential images were taken, with one minute in between each image, to monitor the crystallization process. It is also important to note that no glass cover slips were used in this work as it has been found to alter polymer crystal growth behaviors.[14]

7.4   Results and Discussion

The baselines for comparison of the crystalizability of the compatibilized and non-compatibilized nanocomposite blends are the non-isothermal crystallization behaviors of the as-molded and annealed specimens (see **Figure 7.1**). The nanocomposite blends had low degrees of crystallinity after melt-blending, very similar to the previously studied bulk PET and its nanocomposites and the unfilled PET/PC blends, during the melt-blending process. We find the initial DSC scan after injection molding (**Figure 7.1a**) has a substantial cold crystallization peak (T_{cc}) at 115 °C in the unfilled and non-compatibilized blends and at 140 °C for the bulk PET and the compatibilized blends. Annealing at 140 °C for 1.5 hours drove the crystallization process to near

completion as no cold crystallization peak is observed in the annealed specimens (**Figure 7.1b**).

Considering for a moment the morphology of the compatibilized nanocomposites (recall the TEM imaging from **Chapter 6**), it could be assumed that based on the lack of large crystallizable PET domains, the crystalizability of such nanocomposites would be severely inhibited. From an experimental standpoint, we confirm here a depression in the overall crystalizability of the compatibilized blends, which becomes more exaggerated as the PC fraction rises (**Figure 7.1c**). A slight depression in the melting temperature of the compatibilized blends was observed and we note the absence of dual melting behaviors in both the as-molded and annealed samples.

Shifting the focus to the unfilled and non-compatibilized blends, we observe that as the PC fraction rises a corresponding increase in the overall degree of crystallinity is evident. When comparing the as-molded crystalline fraction of all samples, we find the degree of crystallinity (about 16 % to 19 %) is generally independent of the sample morphology or blend concentration, an important factor when considering the mechanical properties of the all systems covered in these works were examined on as-molded specimens. Thus, the relative degree of crystallinity for the PET in all of the melt-blended samples was indeed similar.

Figure **7.1**
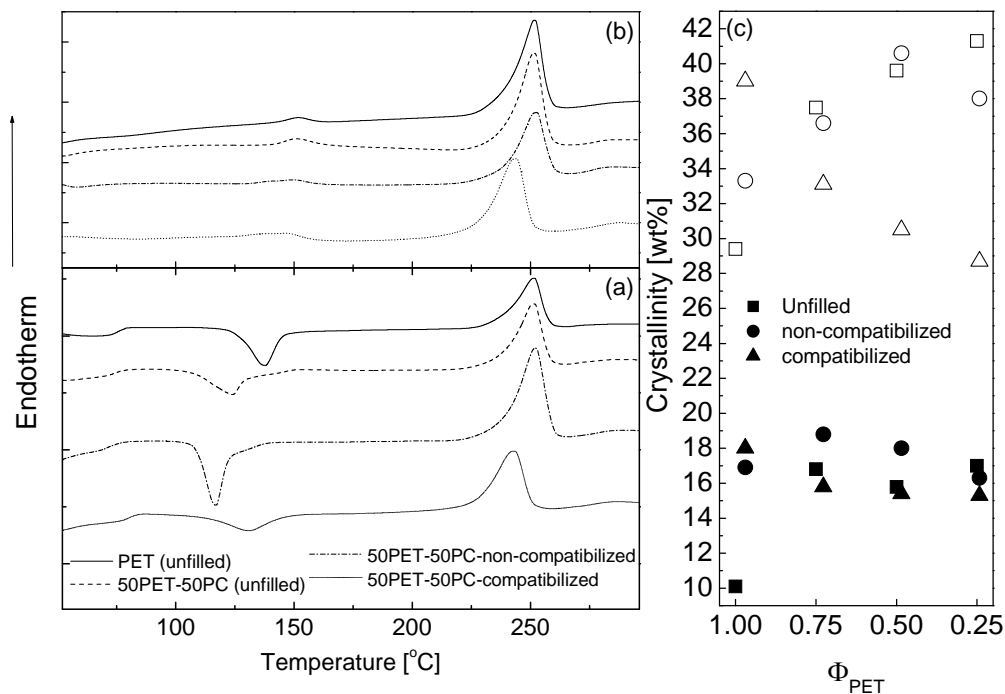
Figure **7.1**: DSC scans of (a) as-prepared, (b) annealed, and (c) comparison of the as-molded (closed) versus the annealed (open) degree of crystallization.

The crystallization/melting behaviors were further probed from a non-isothermal standpoint by cooling the samples from a quiescent melt (see **Figure 7.2**). From a morphological standpoint, the non-compatibilized nanocomposite blends behave much like the unfilled blends – and are unaffected by the amorphous PC domains. The physical restrictions alone of the compatibilized nanocomposite blends – severely impact the crystallization behaviors such that the PC does hinder the crystallization process.

Figure **7.2**
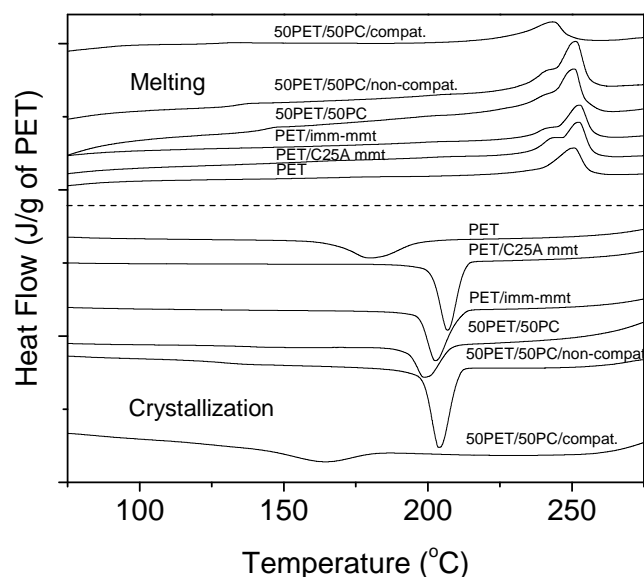
Figure **7.2**: Crystallization and melting behaviors of PET, PET/PC blends, PET/mmt nanocomposites, and PET/PC/mmt nanocomposite blends when cooling from the melt.

Table **7.1**

Table **7.1**: Non-isothermal crystallization and melting behaviors of the PET depending on morphology and blend type upon cooling from a quiescent melt.

Sample	$t^{1/2}$ (s)	T_c (ºC)	T_c onset (ºC)	T_m (ºC)	ΔT (T_m-T_c)
PET	104	180	198	251	71
PET/C25A mmt	34	207	213	253	46
PET/imm-mmt	49	203	211	253	50
50PET/50PC	54	199	208	251	52
50PET/50PC/non-compat.	40	204	211	251	48
50PET/50PC/compat.	110	164	182	243	80

PLOM investigation of the isothermal crystallization of PET and its nanocomposites was completed in **Chapter 3**. In review, nucleation of bulk PET occurs with an induction time of less than one minute and initial impingement occurring after four minutes with the PET spherulite size being 24 ± 2 micrometers. The addition of the

alkyl-ammonium modified C25A mmt led to irregular growth at the outset with eventual correction such that what appeared to be normal spherulitic growth occurred with the final spherulite 16 ± 2 micrometers. The introduction of the thermally stable imm-mmt led to spherulites which were smaller yet. These PET/mmt nanocomposites experience a sharp rise in nucleation density upon layered silicate addition and underwent heterogeneous nucleation.

Previous studies in this thesis catalogued the requisite 10 °C decline in the isothermal crystallization temperature for the 50PET/50PC blend. The crystallization behaviors of the unfilled PET/PC blends (*cf.* **Chapter 5**) indicated that prior to nucleation and growth, phase coalescence of the PET domains was observed prior to crystallization. The average spherulite size of the 50PET/50PC blend was 9 ± 1 micrometers (see **Figure 7.4**). When considering the 50PET/50PC non-compatibilized nanocomposite blend, the strong nucleating effect of the mmt is again apparent as isothermal crystallization readily occurs at 237 °C as confirmed by PLOM. The layered silicate in the non-compatibilized nanocomposite blends spurs heterogeneous nucleation with similar spherulite growth behaviors as those observed in the PET/mmt nanocomposites (*cf.* **Chapter 3**).

However, the spherulite size is again reduced compared to the bulk PET and even the unfilled PET/PC blends because of the nucleation density increase and subsequent impingement before substantial growth can take place.

Figure **7.3**
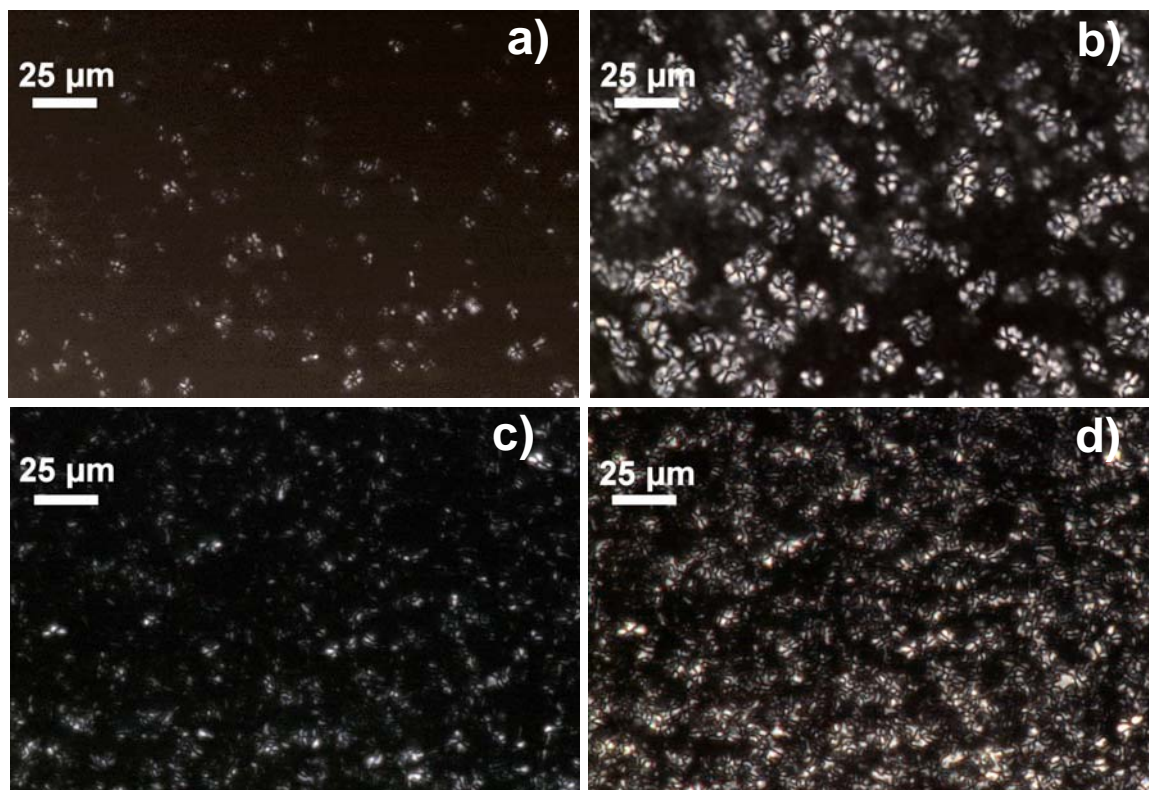
Figure **7.3**: PLOM of isothermal crystallization of the 50PET/50PC blend at: a) 20 minutes and b) 30 min. at 227 °C, and the 50PET/50PC/non-compatibilized blend at: c) 13 min. and d) 30 min. at 237 °C.

The compatibilized nanocomposite blends are difficult to resolve under isothermal crystallization conditions as creating a sample in which a single layer of polymer was present proved difficult. As was the case for the unfilled blends, the crystallization temperature is also reduced to 227 °C, again indicating the strong nucleating effect of the layered silicate is overcome by the morphological restrictions imposed by the compatibilization of the PET and PC phases. Likewise, it should be noted again, the compatibilization is not a true compatibilization in the sense that crystallization is only hindered – not eliminated.

7.5 **Conclusions**

Examination of the crystallization and melting behaviors of PET, PET/mmt nanocomposites, PET/PC unfilled blends, and compatibilized and non-compatibilized nanocomposite blends was completed. Morphology based differences in the undercooling and the crystallization/melting temperatures were observed. The crystalizability is more restricted in the compatibilized nanocomposite systems as a function of the reduction in large PET domains. The compatibilized morphology also reduces the overall degree of PET crystallinity, yet the non-compatibilized morphology follows the behaviors exhibited by the PET/mmt nanocomposites and the unfilled PET/PC blends. Perhaps the most important discovery is related to the overall degree of crystallinity in the as-molded samples. We find that there is no appreciable difference in the relative degree of crystallinity in the as-molded injection molded test specimens regardless of phase morphology, blend concentration, whether the system was filled or unfilled, or the phase of mmt dispersion.

References

1. Alexandre, M. and Dubois, P., *Materials Science and Engineering* 2000; R28:1–63.

2. Ray, S.S. and Okamoto, M., *Progress in Polymer Science* 2003; 28:1539–1641.

3. Giannelis, E.P., Krishnamoorti, R., and Manias, E., *Advances in Polymer Science.* 1998; 138:107–148.

4. Xu, W., Liang, G., Zhai, H., Tang, S., Hang, G., and Pan, W-P., *European Polymer Journal* 2003; 39:1467–1474.

5. Manias, E., Polizos, G., Nakajima, H., and Heidecker, M.J., **Flammability of Polymer Nanocomposites.** Editors: Wilkie and Morgan, Wiley & Sons, NJ, 2007.

6. Lincoln, D.M., Vaia, R.A., Wang, Z-G., Hsiao, B.S., and Krishnamoorti, R., *Polymer* 2001; 42:9975–9985.

7. Lincoln, D.M., Vaia, R.A., Wang, Z-G., and Hsiao, B.S., *Polymer* 2001; 42:1621–1631.

8. Wang, Y., Shen, C., Li, H., Li, Q., and Chen, J., *Journal of Applied Polymer Science* 2004; 91:308–314.

9. Ou, C.F., Ho, M.T., and Lin, J.R., *Journal of Polymer Research* 2003; 10:127–132.

10. Wan, T., Chen, L., Chua, Y.C., and Lu, X. *Journal of Applied Polymer Science* 2004; 94:1381–1388.

11. Marchese, P., Celli, A., and Fiorini, M., *Macromolecular Chemistry and Physics* 2002; 203:695–704.

12. Heidecker, M.J. and Manias, E. *Communication under Preparation*

13. Wunderlich, B., **Macromolecular Physics, Vol. 1, Crystal Structure, Morphology, Defects,** Academic Press, New York, NY, 1973.

14. Schultz, J.M., **Polymer Crystallization**, Oxford University Press, New York, NY 2001.

Chapter 8

Concluding Remarks and Potential Future Study Directions

Polymer nanocomposites based on high performance polymers reinforced by nanoscale 2-dimensional fillers were studied in this thesis. The incorporation high aspect ratio layered silicates, such as organically modified montmorillonites, were found to enhance a wide variety of material properties upon favorable dispersion in the host polymer matrix. The development of thermally stable surfactants also played an important role in the enhancement of material properties.

The flammability characteristics of polymer nanocomposites were found to be enhanced via the well-known mechanism of char formation. The ability of the char to act as a mass transport barrier to restrict the high energy combustibles from reaching the flame source and also as a thermal insulator to protect the underlying virgin polymer was well documented in the poly(methyl methacrylate), poly(ethylene terephthalate), and polystyrene nanocomposites that were examined.

The hallmark of polymer nanocomposites is the synergistic enhancement of many material properties without severe penalties in other properties, as is typically the case with performance tradeoffs in conventional polymer composites. We observed significant enhancements in poly(ethylene terephthalate) nanocomposite material properties as compared to the bulk with respect to thermal stability, the relative modulus, and altered crystallization behaviors – all at low filler loadings – without observing a severe penalty in the composite ductility, especially when high thermal stability surfactant modifications

were applied to the layered silicate. Future studies from this end should focus on the further development of other high thermal stability surfactants, such as quinolinium based treatments, which can render the filler even more hydrophobic and thus reduce the water-induced degradation of PET during melt processing. Likewise, intrinsic viscosity measurements would help to better quantify the overall thermal degradation of PET observed during melt-blending.

Polycarbonate, another high melt-processing temperature engineering polymer, nanocomposites reinforced by montmorillonite were also studied, with the emphasis on optimizing the layered silicate surfactant treatment. The success of each individual nanocomposite was examined such that the best combination of mechanical and thermal properties was achieved, while keeping the molecular weight degradation under control. Preferential filler-platelet alignment was determined to have negligible influences on the overall reinforcing effect in highly aligned nanocomposites, a rather striking finding. Future studies should focus on a wider-range of filler alignments, such that a true gauge of the reinforcing effect when preferential alignment of filler and of polymer occurs can be examined in detail.

Novel nanocomposites of immiscible blends of poly(ethylene terephthalate) and polycarbonate offered the best, probably, results of this thesis, and present the highest promise for future studies. Control of the composite phase morphology, by preferential dispersion of fillers in one phase or through fillers promoting compatibilization between the two polymers, and offers truly unique potential for tailoring material properties depending on the dispersive phase of a given nanocomposite blend. For example, an impressive improvement in ductility *and* modulus was observed in PET-rich

compatibilized nanocomposite blends. Future studies should be focused upon quantifying the degree of transesterification reactions, and tracing the origin of this behavior (*cf.* gauge the relative importance of the filler induced changes in crystal morphology, against transesterification, nanocomposite reinforcement due to physisorbed polymer, and/or other mechanisms). Likewise, similar nanocomposite approaches to other amorphous/crystalline immiscible blends, when incorporating layered silicate fillers preferentially or in a compatibilizing manner, may also offer an attractive avenue towards 'smart' nanocomposite design that could be utilized to alter the material properties and the nature of these blends, based on the "phase" of filler dispersion. Surfactant optimization may also be undertaken to probe the potential maximum enhancement in material properties in such systems.

VITA

Matthew John Heidecker was born on June 1st, 1980 in Erie, Pennsylvania to William and Louise Heidecker. He was the eldest of three children – and is the product of a family whose competitiveness is rivaled by few. His educational path was always unique. He chose the alma mater of his mother for his high school education, Mercyhurst Prep, which of course precluded his siblings from following suit (it was a good thing there are *three* Catholic high school's in Erie). From there, his college education was pursued at Penn-State Erie in Plastic Engineering Technology, where he received a Bachelor of Science degree with Honors and Distinction in May of 2002. That fall, he enrolled in the Materials Science and Engineering program at Penn State University under the direction of Evangelos Manias to pursue a PhD. in polymer science. Throughout his doctorate degree, his research interests were focused on polymer nanocomposites, resultant mechanical behaviors, flammability characteristics of nanocomposites, crystallization, and polymer/layered silicate degradation behaviors. Upon defending his dissertation, he accepted a position at Emerson Climate Technologies with the title of Lead Engineer, Polymers and currently resides in Troy, OH. His alternative interests (to science) are traveling, running, politics, cooking, and reading.

Select Publications (more to come!)

- Manias, E., Polizos, G., Nakajima, H., and Heidecker, M.J., **<u>Flammability of Polymer Nanocomposites.</u>** Editors: Wilkie and Morgan, Wiley & Sons, NJ, 2007.

- Costache, M.C., Wang, D., Heidecker, M.J., Manias, E., and Wilkie, C.A., *Polymers for Advanced Technologies* 2006; 17:272–280.

- Costache, M.C., Heidecker, M.J., Manias, E., and Wilkie, C.A., *Polymers for Advanced Technologies* 2006; 17: 764–771.